Research on the Effect of Cathode Catalyst Structure on Performance and Durability in Polymer Electrolyte Fuel Cells

A Doctoral Thesis

Presented to

Integrated Graduate School of

Medicine, Engineering, and Agricultural Sciences

University of Yamanashi

March 2022

Aki Kobayashi

Contents

Chapter 1 General Introduction

1-1. Background

In recent years, energy consumption, including fossil fuels, has continued to increase due to global population growth and livelihood improvement. Due to the large consumption of fossil fuels, the concentration of CO_2 in the atmosphere, which is considered to be a greenhouse gas, continues to increase, and especially after the industrial revolution in the 1980s, the concentration of CO_2 began to increase. Furthermore, changes in global mean surface temperature are said to be roughly linearly related to total cumulative CO_2 emissions.[1] The world population in 2021 will be 7,875 million. According to the United Nations World Population Prospects 2019, the number will reach 8.5 billion in 2030, 9.7 billion in 2050, and 10.9 billion in 2100.[2] According to the Intergovernmental Panel on Climate Change (ICPP), the impact of global warming caused by greenhouse gases (GHG) such as CO_2 will increase the number of people affected by water shortages, especially in developing countries, to hundreds of millions, increasing the risk of floods, heat waves, and infectious diseases.[3] The Leaders' Summit on Climate was held in 2021 and each country set new GHG emission reduction targets (Table 1-1).[4] Among them, Japan declared in 2030 that it would aim to reduce greenhouse gas emissions by 46% compared to 2013.[5] To reduce CO_2 emissions worldwide, it is necessary to develop new renewable energy alternatives to fossil fuels. As renewable energies, solar power, wind power, geothermal power, hydropower, biomass, hydrogen, etc. do not emit CO_2 during power generation, and there is no need to worry about resource depletion, so they are attracting attention. Under such circumstances, hydrogen is superior in the following points. (1) Since water can be decomposed into hydrogen by an electrochemical reaction, surplus electricity can be converted into hydrogen and stored

for a long period of time. (2) It can be used for a wide range of purposes, from personal use to large-scale power generation. (3) Since it can be extracted from various resources (water, natural gas, fossil fuel, by-product gas, methane gas, etc.), it is not easily affected by raw material prices, climate changes, and regional differences. (4) It becomes a distributed energy source and can secure a stable power supply even in an emergency. CO_2 is emitted when hydrogen is produced, but by combining it with CCS (Carbon dioxide Capture and Storage), it is possible to suppress the generation of CO_2.[6] In addition, Japan relied on oil for 75% of its primary energy, and nearly 80% of it depended on imports from overseas. In particular, it has a big problem from the viewpoint of "securing

Table 1-1. GHG reduction targets in major countries / regions and the percentage of CO_2 emissions in the world (2018).

Country / Region	GHG reduction target		Percentage of CO_2 emissions in the world (2018)
	Medium-term target (Year to compared)	Carbon neutral achievement target year	
USA	-50 to -52% in 2030 (2005)	2050	14.7%
JAPAN	-46% in 2030 (2013)	2050	3.2%
EU	-55% in 2030 (1990)	2050	9.4%
UK	-78% in 2035 (1990)	2050	
Canada	-40 to -45% in 2030 (2005)	2050	1.7%
China	Gradually reduce coal Consumption from 2026 to 2030	2060	28.4%
India	Emissions per GDP in 2030: -33 to -35% (2005)	-	6.9%
Russia	-30% in 2030 (1990)	-	4.7%
Korea	-17% in 2030 (2017)	2050	1.8%
Brazil	-43% in 2030 (2005)	2050	1.2%

energy safety", such as being easily affected by the international situation because it is highly dependent on a specific country or area.[7] If resources in Japan can be used as a raw material for hydrogen and used as an alternative energy to fossil fuels, diversification of energy and improvement of energy self-sufficiency can be expected. A fuel cell is a power generation device that can electrochemically react hydrogen and oxygen and directly extract them as electrical energy. A fuel cell vehicle (FCV) is equipped with hydrogen filled in a high-pressure cylinder and supplies hydrogen directly to the fuel cell. As for FCV, Toyota Motor Co., Ltd. started general sales of “MIRAI” in December 2014, and Honda Motor Co., Ltd. started sales of “Clarity Fuel Cell” in March 2016. The fuel cell bus (SORA) has also been on sale since March 2018.[8] The stationary fuel cell (ENE-FARM) has been on sale in Japan since 2009, ahead of the rest of the world. ENE-FARM is a cogeneration system that stores and uses the heat generated with electricity from fuel cells and can achieve high total energy efficiency (97%). The types of fuel used are city gas, LPG, etc., and hydrogen obtained by reforming these is used to generate electricity. A high target of 5.3 million units will be spread in 2030, and 400,000 units will be spread by 2021.

1-2. Principle and characteristic of fuel cells

The principle of the fuel cell was discovered by Humphry Davy of the United Kingdom in 1801, and the prototype of the fuel cell that is familiar to the current fuel cell was created by William Grove of the United Kingdom in 1839.[9] Platinum was used for the electrodes and dilute sulfuric acid was used for the electrolyte to cause electrolysis of water. Then, hydrogen gas and oxygen gas were stored in the test tube, and 4 sets of these were connected in series. The power generated by this device could be used to electrolyze

water that has entered another device. He showed that the electrochemical dissociation of water was almost reversible. A fuel cell supplies hydrogen to the negative electrode (anode), oxygen to the positive electrode (cathode), and extracts electrons directly from the chemical reaction that occurs on the catalyst. The principle of power generation is shown below.

Anode (Hydrogen oxidation reaction)	$H_2 \rightarrow 2H^+ + 2e^-$	(1-1)
Cathode (Oxygen reduction reaction)	$1/2\ O_2 + 2H^+ + 2e^- \rightarrow H_2O$	(1-2)
Total	$H_2 + 1/2\ O_2 \rightarrow H_2O$	(1-3)

The Gibbs free energy change ΔG^0 of all reactions in Equation 1-3 is -237.2 kJ mol^{-1}. The theoretical maximum voltage (electromotive force), E^0 of a fuel cell can be calculated using Equation 1-4.

$$E^0 = -\Delta G^0 / 2F \quad (1\text{-}4)$$

Where F is the Faraday constant (96485 C mol^{-1}). From Equation 1-4, E^0 is calculated to be about 1.229 V. The theoretical energy conversion efficiency (ε^0) is calculated from the reaction enthalpy change amount ΔH^0 and the electrical energy ΔG^0, and can be calculated using Equation 1-5.

$$\varepsilon^0 = -\Delta G^0 / \Delta H^0 \quad (1\text{-}5)$$

Here, ΔH^0 is 285.8 kJ mol^{-1}, and the theoretical efficiency is 83% (HHV: Higher Heating Value). The state of the generated water is assumed to be liquid and calculated by HHV. In a fuel cell, unlike other power generation methods, in the process of converting chemical energy into electric energy, there is no alternative conversion such as thermal conversion or mechanical conversion, and the chemical energy is directly converted into electric energy and thermal energy. Therefore, such a high theoretical power generation efficiency can be obtained. It is not possible to extract electric energy with this theoretical electromotive force and theoretical efficiency at the time of power generation, and a voltage drop occurs according to the load applied to the fuel cell. The product of the operating current and voltage is the electrical energy that can be taken out to the external circuit, and the power of the polarization is converted into heat. There are various types of fuel cells depending on the form of the electrolyte and the fuel. Table 1-2 shows a comparison of four types of fuel cells that have been actively researched and developed in recent years. Phosphoric acid fuel cell (PAFC) is being actively researched and developed among various types of fuel cells. However, the phosphoric acid contained in the electrolyte causes corrosion. Therefore, it is common to use platinum, which is a stable metal, for the catalyst, and cost reduction is one of the major issues. Molten carbonate fuel cell (MCFC) has high power generation efficiency and operate at high temperatures,

Table 1-2. Types and characteristics of fuel cells.

	Polymer electrolyte fuel cell (PEFC)	Phosphoric acid fuel cell (PAFC)	Molten carbonate fuel cell (MCFC)	Solid oxide fuel cell (SOFC)
Electrolyte	Polymer ion exchange membrane	Liquid phosphoric acid	Molten carbonate salt	Solid oxide
Fuel	H_2	H_2	H_2, CO	H_2, CO
Operating temperature	60-100°C	170-200°C	600-700°C	700-1000°C
Efficiency (HHV)	30-40	35-45	50-65	50-70

so the reaction at the electrodes is easy to proceed, and an expensive catalyst such as platinum is not required. In addition, it has the advantages of high energy efficiency because it can effectively use the high-temperature exhaust gas emitted, and that various fuels such as hydrocarbon fuels and CO can be used. However, since high temperature molten carbonate is highly corrosive, there are still many problems in improving reliability such as deterioration of materials. Since the solid oxide fuel cell (SOFC) operates at a high temperature like the MCFC, it is not necessary to use an expensive metal such as platinum as a catalyst, and high energy efficiency can be expected. However, due to high temperature operation, the reliability required for materials is strict, and there are problems such as enormous number of parts, quality control of each member, and long startup time. The Polymer electrolyte fuel cell (PEFC) uses a proton-conducting polymer membrane as the electrolyte and operates at a very low temperature of around room temperature to around 100 °C, so the startup time is short. Furthermore, it is possible to make the electrolyte thinner, and it is possible to reduce the size and weight. Moreover, since PEFC does not contain a liquid material, it is extremely stable against vibration. For these reasons, PEFC is being researched and developed by many companies, universities, and research institutes as a power source for automobiles and households. On the other hand, as with PEFC, expensive platinum (Pt) is used for the catalyst, and cost reduction is a major issue. In addition, deterioration in the electrodes, mainly the catalyst, tends to progress due to repeated startup and shutdown and output changes, and improvement of durability and reliability is also a major issue.

1-3. Structure and theory of PEFCs

The basic building block of a fuel cell is called a single cell. Figure 1-1 shows a schematic diagram of a single cell of PEFC. PEFC is composed of a polymer electrolyte membrane in which protons pass, a catalyst layer in which a power generation reaction occurs, a Gas Diffusion Layer that evenly diffuses the supplied gas to the electrodes, and a bipolar plate that supplies and discharges gas and extracts electrons to the outside. The membrane electrode assembly (MEA) has a structure in which a catalyst coated membrane (CCM) coated with a catalyst layer on both sides of a polymer electrolyte membrane is sandwiched between two gas diffusion layers (GDL) and the outside is gripped by a bipolar plate. Since the power that can be obtained with a single cell is small, the fuel cell system is equipped with a stack in which single cells are stacked. When single cells are stacked, the amount of heat generated increases and the cell temperature rises, so the stack includes accessories such as a cooling plate and heat exchanger to control the cell temperature, and output terminals. Each reaction for power generation proceeds in

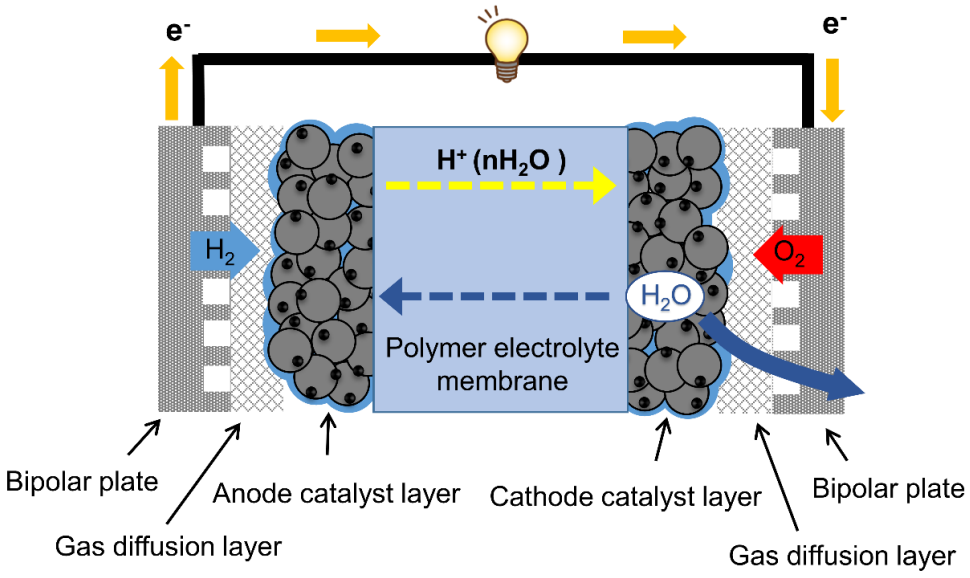

Figure 1-1. Schematic diagram of the PEFC.

the catalyst layer, the hydrogen oxidation reaction (HOR) shown in Equation 1-1 proceeds in the anode, and the oxygen reduction reaction (ORR) shown in Equation 1-2 proceeds in the cathode. The power generation characteristics of PEFC are represented by the current−potential polarization ($I-V$) curve as shown in Figure 1-2. As mentioned above, the theoretical electromotive force of a fuel cell is about 1.229 V, but it does not reach the theoretical electromotive force due to voltage drop factors caused by various internal resistances. When the electrochemical reaction proceeds out of equilibrium state, the electrode potential deviates from the equilibrium potential. The phenomenon in which the electrode potential changes is called polarization (η), and the potential that deviates at that time is called overvoltage. Overvoltages are roughly classified into three types.

1. Reaction overvoltage

The overvoltage required to change the activation energy is called reaction overvoltage, and the magnitude of this overvoltage is mainly determined by the activity of the catalyst used. Since the HOR at the anode shown in Equation 1-1 proceeds very quickly when Pt

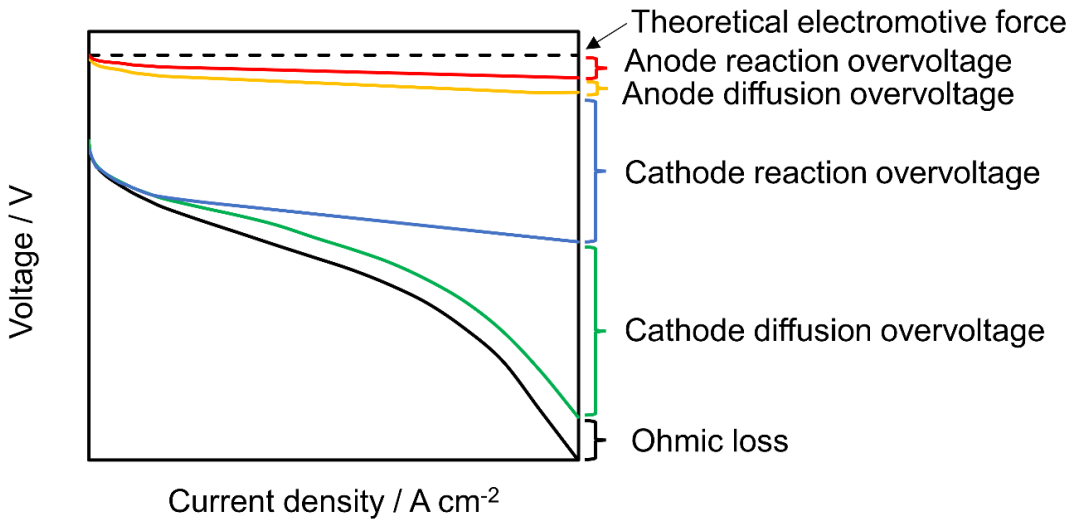

Figure 1-2. The current-potential relationship and cell voltage loss factor of PEFC.

is used as the catalyst, the reaction overvoltage is almost negligible.[10,11] On the other hand, the ORR at the cathode shown in Equation 1-2 is slow and shows a large reaction overvoltage even when platinum is used as the catalyst. This is one of the major factors that cause the voltage drop in PEFC.

2. Diffusion overvoltage

If the supply of the reactant to the reaction interface is delayed in the progress of the electrochemical reaction, the concentration of the reactant at the reaction interface decreases. Since the reaction rate in an electrochemical reaction depends on the concentration of the reactants, a decrease in the concentration of the reactants contributes to the decrease in the reaction rate. Therefore, it is necessary to reduce the activation energy in order to maintain the reaction rate even if the reaction product concentration decreases, and as a result, the electrode potential changes. The overvoltage at this time is called diffusion overvoltage. The diffusion overvoltage is affected by the diffusivity and permeability of the reaction gases (hydrogen and oxygen) in the GDL and the catalyst layer, and the drainage property of the water produced by the electrochemical reaction. The phenomenon that the diffusion overvoltage rises occurs because the water generated at the cathode accumulates in the GDL and the cathode catalyst layer and inhibits the diffusion of gas (flooding). This flooding phenomenon occurs more prominently as the current density increases because the amount of generated water increases as the current density increases.

3. Ohmic loss

The voltage drop caused by ohmic resistance is called ohmic loss and is caused by the conductive resistance of ions and electrons inside the cell. Ohm loss is mainly caused by each material (GDL, bipolar plate, electron conductor such as current collector plate,

polymer electrolyte membrane) that composes the fuel cell.

The resistance generated by reaction overvoltage and diffusion overvoltage does not have a constant value and does not obey Ohm's law.

The cell voltage (E_{cell}) can be described by Equation 1-6.

$$E_{cell} = E^0 - (\eta_{act,\ anode} + \eta_{diff,\ anode} + \eta_{act,\ cathode} + \eta_{diff,\ cathode} + \eta_{ohm}) \quad (1\text{-}6)$$

$\eta_{act,}$, η_{diff} and η_{ohm} indicate reaction overvoltage, diffusion overvoltage, and ohm loss, respectively. In PEFCs, Pt is generally used as an electrode catalyst for both the anode and the cathode. A catalyst (Pt/C) in which Pt particles are supported on a carbon black (CB) support such as Vulcan or Ketjen black is often used. CB supports are produced by pyrolysis of hydrocarbons such as natural gas and petroleum-treated aromatic residues. The most common manufacturing process is a furnace black process in which the raw material is incompletely burned in an air atmosphere of about 1000 ℃, where the CB support forms chain aggregates. In addition, by activating to generate micropores on the order of nm inside the carbon material and increase the internal surface area, it is possible to produce a CB support having a specific surface area in the range of 8 to 1500 m^2 / g. Figure 1-3 shows a TEM (Transmission Electron Microscopy) image of a typical electrode catalyst. In this image, the black dots with a diameter of several nm are the Pt particles, and the base on which the Pt particles are supported is the CB support with a diameter of 20 to 50 nm. It can be seen that the Pt particles are highly dispersed on the CB support. The catalyst layer is composed of a catalyst consisting of CB supports and Pt particles and an ionomer. Ionomer is a proton conductor with the same composition as

the polymer electrolyte membrane, and is dispersed inside the catalyst layer together with Pt/C. ORR kinetics are sluggish than HOR. The ORR reaction proceeds at the three-phase interface, which is the interface where O_2, electrons (e^-), and protons (H^+) are present.

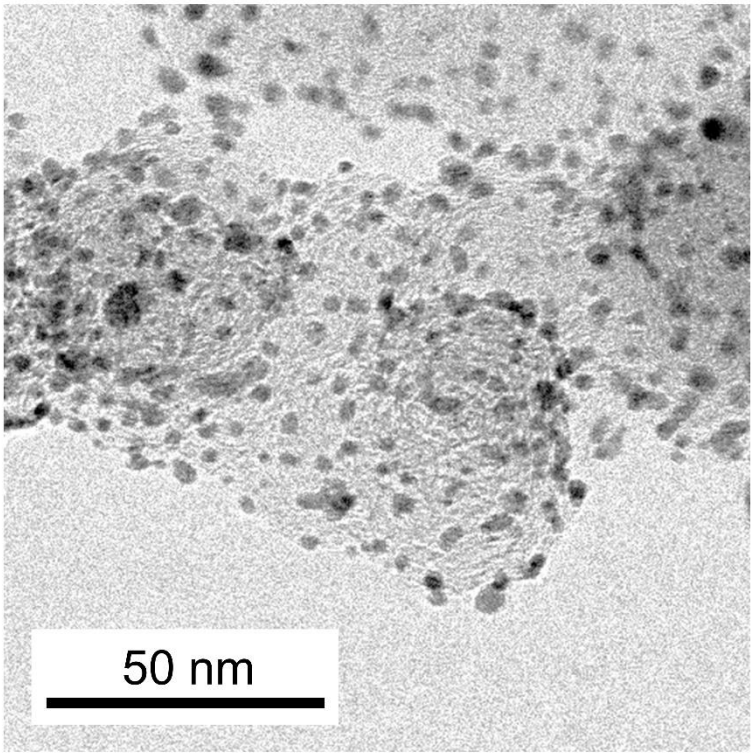

Figure 1-3. TEM image of Pt/C electrode catalyst layer.

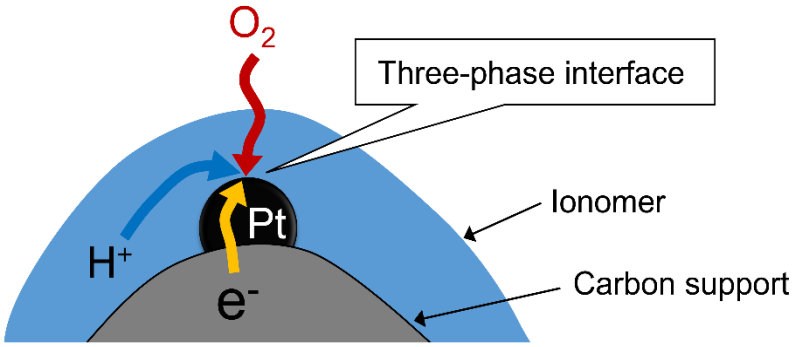

Figure 1-4. Schematic diagram of the three-phase interface of the cathode catalyst layer.

Figure 1-4 shows a schematic diagram of the three-phase interface of the catalyst layer. Proton and electron exchanges occur in cathode catalysts. In order to proceed this reaction in the electrode catalyst layer, a proton conduction path, an electron conduction path and a reaction gas transport path are required at the reaction point. The ionomer or water, the CB supports, and the pores in the catalyst layer are responsible for each mechanism, and the reaction takes place on the Pt particles. In order for these reactions to proceed efficiently, it is important that the surface area of the Pt particles is large and that there are sufficient electron, proton, and oxygen transfer paths.

1-4. Issues and development trends of PEFCs

Figure 1-5 shows the breakdown of the fuel cell stack cost per annual production.[12] The ratio of catalyst is the highest among all components, and the ratio increases as the annual production increases. Platinum (Pt) accounts for most of the cost of the catalyst. Therefore, when fuel cells become widespread in earnest, it is essential to reduce the amount of platinum used in order to reduce the cost of stacks. Therefore, when fuel cells become widespread in earnest, it is essential to reduce the amount of platinum used in order to reduce the cost of stacks. As mentioned in section 1-3, ORR requires more Pt because the reaction is more difficult than HOR. In addition, the cathode catalyst layer requires a large amount of Pt loading because various operation patterns including startup / shutdown and load operation deteriorate the cathode catalyst and the polymer electrolyte membrane. Therefore, many studies have been carried out focusing on improving ORR activity and durability in the cathode catalyst layer.[13–15] The electrochemical reaction in PEFC occurs at "the place where the three-phase interface is formed on the surface of Pt particles" as shown in Figure 1-4. The amount of this place is generally expressed by the surface area

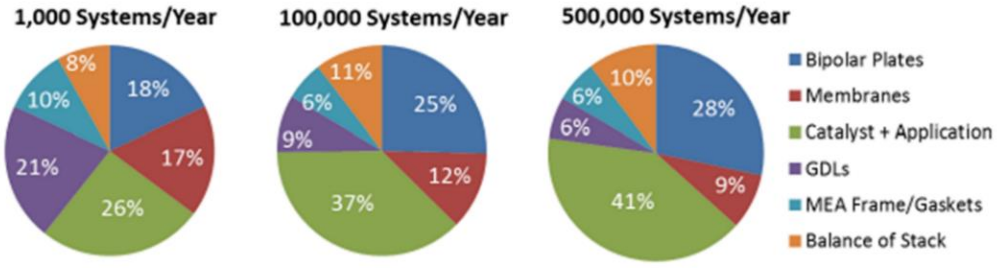

Figure 1-5. Breakdown of the 2017 projected fuel cell stack cost at 1,000, 100,000, and 500,000 systems per year.

per unit weight of Pt and is called ECSA (Electro Chemical Surface Area, $m^2 g^{-1}$). This is an important parameter that indicates the characteristics of the fuel cell electrode, and the larger this value, the higher the PEFC performance tends to be. It is also important for the catalyst to maintain high ECSA and mass activity in order to maintain high cell performance over a long time period.[16,17] Since ECSA indicates the surface area forming the three-phase interface in the non-power generation state, the ionomer is responsible for the proton conduction path. In other words, it can be said that ECSA is the surface area of Pt particles covered by ionomer. In order to reduce the amount of Pt used in PEFCs, it is important to increase the reaction area (ECSA) that can contribute to the electrochemical reaction. Therefore, many catalysts using low-surface-area carbon (LSC) as a CB support have been studied based on the concept of utilizing Pt without waste by covering all Pt with ionomer. Since LSC is a solid carbon support with low activation and few pores, it has a structure in which Pt particles are supported on the surface of CB support.[18,19] In recent years, catalysts using high-surface-area carbon (HSC), which has many pores of 10 nm or less, have been attracting attention. Since HSC has a large specific surface area, Pt is dispersed in small particles (1 to 5 nm), and a large amount of Pt particle is supported in the pores.[20] Since Pt becomes smaller particles, the surface area

per unit weight of Pt becomes large, but there are many Pt particle that are not covered with ionomer because it is difficult for ionomer to enter into the pores.[21] However, studies are underway based on the concept of forming a proton conduction path on Pt particle in the pores with the water generated during power generation so that it can contribute to the electrochemical reaction.[22] The fuel cell stack installed in the MIRAI sold by Toyota Motor Co., Ltd. also used a solid carbon support in the first generation sold in 2014. Porous carbon supports (MCND) are used in the second generation sold in 2020, and catalysts using supports with many pores are attracting more and more attention.[23]

In order to improve the catalyst, it is important to understand the relationship between characteristics of catalyst structure, chemical properties, electrochemical properties and the performance or durability. Many studies have been done on the effects of catalyst structure on performance and durability.[24 −28] The major structural difference between LSC and HSC is the pores of 10 nm or less. Many studies have indicated that most of the Pt particle supported in the pores is not covered with ionomer,[29 ,30] but the relationship between the pore structure and the ionomer covering state remains unclear. In catalysts using HSC, most Pt particles are present in the pores, so it is important to clarify the relationship between the ionomer state near the pores and cell performance. However, it is very difficult to directly clarify the structure near the pores. This is because, as shown in Figure 1-3, the position and shape of the pores cannot be observed with a microscope. Therefore, there is a need for a method that can indirectly understand the structure of pores.

Many studies have been done on the durability of PEFCs. There are multiple factors that reduce the cell performance of Pt-based catalysts. There is an increase in Pt particle size due to electrochemical Ostwald ripening or particle migration and coalescence,[31 −34

elution of Pt into the polymer electrolyte membrane,[35–38] and detachment of Pt particles from CB support due to corrosion.[39,40] In actual fuel cell operation, these factors combine to reduce cell performance. Many durability tests carry out potential cycles that simulate startup and shutdown and load operation under the H_2/N_2 atmosphere.[41,42] This is to simply evaluate the effect of the potential on the deterioration of the catalyst and clarify the deterioration mechanism. On the other hand, it has not been possible to evaluate the situation including the influence of the flow of generated water and gas in actual load operation. In order to design a highly durable catalyst in an actual machine, the actual durability should be evaluated under the conditions including the influence of the flow of generated water and gas in the actual load operation. On the other hand, this test has not been able to evaluate the durability in a situation that includes the influence of the flow of generated water and gas in actual load operation. In order to develop a highly durable catalyst in an actual system, the durability should be evaluated under the conditions including the influence of generated water and gas flow in actual load operation.

1-5. Objective and structure of this research

As mentioned above, expectations are rising for the spread of fuel cells from the perspective of solving energy problems and social problems. In particular, catalysts play an important role in promoting the conversion of chemical energy to electrical energy, which strongly affects cell performance and durability. Furthermore, since expensive platinum is used, the cost ratio of the catalyst in the stack is high, it is very important to improve the catalyst with high platinum utilization and high durability. For that purpose, it is important to understand the relationship between the structure of the catalyst and the cell performance and durability. The main purpose of this study was to analyze the

structure of the catalyst, evaluate the cell performance and durability of MEA, and show the design guideline of the catalyst that leads to the improvement of cell performance and durability.

First, in Chapter 2, I focused on the structure of the CB support. Catalysts were prepared using four different CB supports, and the structure of each CB support and catalyst was analyzed from scanning transmission electron microscopy (STEM) observation and N_2-adsorption measurements, and at the same time, cell performance and electrochemical measurements were performed. Furthermore, by carrying out the load cycling in the H_2/Air atmosphere, the durability in the situation simulating the actual load operation was verified. As post-test analysis, electrochemical measurement, catalyst observation by STEM, observation of polymer electrolyte membrane cross section by the focused ion beam device (FIB), and EPMA were performed to investigate the effect of catalyst structure on durability. This provided design guidelines for CB support of catalyst that achieve high cell performance and durability.

Next, in Chapter 3, I focused on the structure of the Pt particles in order to establish a more optimal catalyst structure. Using the difference in the Pt loading percentage of the CB support, which had the highest cell performance in Chapter 3, the effect of the morphological change of Pt particles on the cell performance due to the change in the Pt loading percentage was investigated. Here, in addition to the analysis contents of Chapter 3, the limiting current was measured. As for the durability test, in addition to the actual load operation in the H_2/Air atmosphere as in chapter 2, the operation simulating the startup and shutdown was carried out. As a post-test analysis, in addition to the analysis contents of Chapter 3, cross-section observation of the catalyst layer was carried out. From these results, important design guidelines for the development of catalysts that

achieve high cell performance and durability are presented.

Finally, Chapter 4 summarizes the results of Chapter 2 and Chapter 3. These results provided information on the effects of CB support and catalyst structure on cell performance and durability under H_2/Air conditions. In addition, I proposed the future prospects of supports, precious metal particles, and ionomer, which are the constituent materials of the catalyst layer.

1-6. References

1 Friedlingstein, P et.al. Global carbon budget 2020. *Earth Syst. Sci. Data* 2020, 12, 3269–3340.

2 United Nations, “World Population Prospects 2019”, https://population.un.org/wpp/Graphs/Probabilistic/POP/TOT/900

3 The Intergovernmental Panel on Climate Change, “Climate Change 2007: Synthesis Report”, https://www.ipcc.ch/site/assets/uploads/2018/02/ar4_syr_spm.pdf

4 Japan External Trade Organization (JETRO), “Region/Analysis Report”, https://www.jetro.go.jp/biz/areareports/special/2021/0401/9ac24934b1ca2265.html

5 Ministry of Foreign Affairs of Japan, “Japan's emission reduction targets”, https://www.mofa.go.jp/mofaj/ic/ch/page1w_000121.html

6 Ministry of Economy, Trade and Industry, “Basic Hydrogen Strategy December 26, 2017”, https://www.meti.go.jp/english/press/2017/pdf/1226_003b.pdf

7 Agency for Natural Resources and Energy, “What happens when oil stops?”,

https://www.enecho.meti.go.jp/about/special/tokushu/anzenhosho/kasekinenryo.html

8 TOYOTA MOTOR CORPORATION, “News release, March 28th, 2018”, https://global.toyota/jp/newsroom/corporate/21862392.html

9 Grove, WR. On voltaic series and the combination of gases by platinum. *The London, Edinburgh, and Dublin Philosophical Magazine and Journal of Science* 1839, 14, 86–87.

10 Durst, J.; Siebel, A.; Simon, C.; Hasché, F.; Herranz, J.; Gasteiger, H.A. New insights into the electrochemical hydrogen oxidation and evolution reaction mechanism. *Energy Environ. Sci.* 2014, 7, 2255–2260.

11 Debe, M. K. Electrocatalyst approaches and challenges for automotive fuel cells. *Nature* 2012, 486, 43–51.

12 DOE Hydrogen and Fuel Cells Program Record, “Fuel Cell System Cost – 2017”, https://www.hydrogen.energy.gov/pdfs/17007_fuel_cell_system_cost_2017.pdf

13 Shigihara, Y.; Ooi, A.; Tada, E.; Nishikata, A. Dissolution and Consequent Morphological Evolution of Electrodeposited Pt−Cu Nanoparticles under Potential Cycling in 0.5 M H_2SO_4 Solution. *J. Electrochem. Soc.* 2019, 166, C3170−C3178.

14 Gatalo, M.; Jovanovič, P.; Petek, U.; Šala, M.; Šelih, V, S.; Zepeda, F, R.; Bele, M.; Hodnik, N.; Gaberšček, M. Comparison of Pt−Cu/C with Benchmark Pt−Co/C: Metal Dissolution and Their Surface Interactions. *ACS Appl. Energy Mater.* 2019, 2, 3131−3141.

15 Beermann, V.; Holtz, M, E.; Padgett, E.; Araujo, J, F.; Muller, D, A.; Strasser, P. Real-time imaging of activation and degradation of carbon supported octahedral

Pt–Ni alloy fuel cell catalysts at the nanoscale using in situ electrochemical liquid cell STEM. *Energy Environ. Sci.* 2019, 12, 2476–2485.

16 Harzer, G, S.; Schwammlein, J, N.; Damjanovic, A, M.; Ghosh, S.; Gasteiger, H, A. Cathode Loading Impact on Voltage Cycling Induced PEMFC Degradation: A Voltage Loss Analysis. *J. Electrochem. Soc.* 2018, 165, F3118-F3131.

17 Kneer, A.; Jankovic, J.; Susac, D.; Putz, A.; Wagner, N.; Sabharwal, M.; Secanell, M. Correlation of Changes in Electrochemical and Structural Parameters due to Voltage Cycling Induced Degradation in PEM Fuel Cells. *J. Electrochem. Soc.* 2018, 165, F3241-F3250.

18 Uchida, M.; Fukuoka, Y.; Sugawara, Y.; Eda, N.; Ohta, A. Effects of microstructure of carbon support in the catalyst layer on the performance of polymer-electrolyte fuel cells. *J. Electrochem. Soc.* 1996, 143, 2245−2252.

19 Suzuki, T. Fuel Cell Stack Technology of Toyota. *ECS Trans.* 2016, 75, 423–434.

20 Jinnai, H.; Spontak, R, J.; Nishi, T. Transmission Electron Microtomography and Polymer Nanostructures. *Macromolecules* 2010, 43, 1675–1688.

21 Iden, H.; Sato, K.; Ohma, A.; Shinohara, K. Relationship among Microstructure, Ionomer Property and Proton Transport in Pseudo Catalyst Layers. *J. Electrochem. Soc.* 2011, 158, B987−B994.

22 Yarlagadda, V.; Carpenter, M. K.; Moylan, T. E.; Kukreja, R. S.; Koestner, R.; Gu, W.; Thompson, L.; Kongkanand, A. Boosting Fuel Cell Performance with Accessible Carbon Mesopore. *ACS Energy Lett.* 2018, 3, 618−621.

23 Toyota Technical Review “Development of the Fuel Cell System for the Second-Generation MIRAI”. 2021/2, 236.

24 Mohanta, P, K.; Ripa, M, S.; Regnet, F.; Jörissen, L. Effects of Supports BET Surface Areas on Membrane Electrode Assembly Performance at High Current Loads. *Catalysts* 2021, 11, 195.

25 Koga, M.; Matsumoto, H.; Kunishima, M.; Tokita, M.; Masunaga, H.; Ohta, N.; Takeuchi, A.; Mizukado, J.; Sugimori, H.; Shinohara, K.; Uemura, S.; Yoshida, T.; Hirai, S. Microstructure Investigation of Polymer Electrolyte Fuel Cell Catalyst Layers Containing Perfluorosulfonated Ionomer. *Membranes* 2021, 11, 466.

26 Songa, S.; Liang, Y.; Li, Z.; Wanga, Y.; Fu, R.; Wu, D.; Tsiakaras, P. Effect of pore morphology of mesoporous carbons on the electrocatalytic activity of Pt nanoparticles for fuel cell reactions. *Appl. Catal., B* 2010, 98, 132–137.

27 Park, Y.-C.; Tokiwa, H.; Kakinuma, K.; Watanabe, M.; Uchida, M. Effects of carbon supports on Pt distribution, ionomer coverage and cathode performance for polymer electrolyte fuel cells. *J. Power Sources* 2016, 315, 179−191.

28 Tuaev, X.; Rudia, S.; Strasser, P. The impact of the morphology of the carbon support on the activity and stability of nanoparticle fuel cell catalysts. *Catal. Sci. Technol.* 2016, 6, 8276–8288.

29 Lee, M.; Uchida, M.; Yano, H.; Tryk, D. A.; Uchida, H.; Watanabe, M. New evaluation method for the effectiveness of platinum/carbon electrocatalysts under operating conditions. *Electrochim. Acta* 2010, 55, 8504−8512.

30 Uchida, M.; Park, Y.-C.; Kakinuma, K.; Yano, H.; Tryk, D. A.; Kamino, T.; Uchida, H.; Watanabe, M. Effect of the state of distribution of supported Pt nanoparticles on effective Pt utilization in polymer electrolyte fuel cells. *Phys. Chem. Chem. Phys.* 2013, 15, 11236−11247.

31 Sharma, R; Gyergyek, S.; Li, Q.; Andersen, S, M. Evolution of the degradation mechanisms with the number of stress cycles during an accelerated stress test of carbon supported platinum nanoparticles. *J. Electroanal. Chem.* 2019, 838, 82–88.

32 Sharma, R.; Andersen, S, M. Quantification on Degradation Mechanisms of Polymer Electrolyte Membrane Fuel Cell Catalyst Layers during an Accelerated Stress Test. *ACS Catal.* 2018, 8, 3424−3434.

33 Myers, D, J.; Wang, X.; Smith, M, C.; More K, L. Potentiostatic and Potential Cycling Dissolution of Polycrystalline Platinum and Platinum Nano-Particle Fuel Cell Catalysts. *J. Electrochem. Soc.* 2018, 165, F3178-F3190.

34 Xin, H, L.; Mundy, J, A.; Liu, Z.; Cabezas, R.; Hovden, R.; Kourkoutis, L, F.; Zhang, J.; Subramanian, N, P.; Makharia, R.; Wagner, F, T.; Muller, D, A. Atomic-Resolution Spectroscopic Imaging of Ensembles of Nanocatalyst Particles Across the Life of a Fuel Cell. | *Nano Lett.* 2012, 12, 490−497.

35 Baroody, H, A.; Stolar, D, B.; Eikerling, M, H. Modelling-based data treatment and analytics of catalyst degradation in polymer electrolyte fuel cells. *Electrochim. Acta* 2018, 283, 1006−1016.

36 Bi, W.; Gray, G, E.; Fuller, T, F. PEM Fuel Cell Pt／C Dissolution and Deposition in Nafion Electrolyte. *Electrochem. Solid-State Lett.* 2007, 10, B101−B104.

37 Zhang, J.; Litteer, B, A.; Gu, W.; Liu, H.; Gasteiger, H, A. Effect of Hydrogen and Oxygen Partial Pressure on Pt Precipitation within the Membrane of PEMFCs. *J. Electrochem. Soc.* 2007, 154, B1006-B1011.

38 Ohma, A.; Yamamoto, S.; Shinohara, K. Analysis of Membrane Degradation Behavior During OCV Hold Test. *ECS Trans.* 2007, 11, 1181−1192.

39 Mayrhofer, K, J, J.; Meier, J, C.; Ashton, S, J.; Wiberg, G, K, H.; Kraus, F.; Hanzlik, M.; Arenz, M. Fuel cell catalyst degradation on the nanoscale. *Electrochem. Commun.* 2008, 10, 1144–1147.

40 More, K, L.; Borup, R.; Reeves, K, S. Identifying Contributing Degradation Phenomena in PEM Fuel Cell Membrane Electride Assemblies Via Electron Microscopy. *ECS Trans.* 2006, 3, 717–733.

41 New Energy and Industrial Technology Development Organization, “a single cell evaluation and analysis protocol”, https://www.nedo.go.jp/content/100537904.pdf

42 Fuel Cell Commercialization Conference of Japan, “Proposals of the development targets, research and development challenges and evaluation methods concerning PEFCs”, http://fccj.jp/pdf/23_01_kt.pdf

Chapter 2 Effect of Carbon Black Support Structure on Performance and Durability in PEFC Cathode Catalyst

2-1. Introduction

Many studies have been carried out focusing on catalysts and electrolyte (ionomer) in the catalyst layer. The electrolyte, for example, a perfluorosulfonic acid (PFSA) ionomer, is added to transport protons to the Pt. In order to improve the performance of fuel cells, it is important to improve the sites where the gas, protons, and electrons react, which is called the three-phase interface.[1] ECSA is, by definition, the electrochemically active interfacial area between the Pt and the ionomer and is one of the factors that control the cell performance, particularly at low current densities. On the other hand, the ECSA is less consistent with cell performance in the high current density range.[2] Cell performance cannot be evaluated based on the ECSA value alone. Sulfonate groups in the PFSA ionomer also poison the oxygen reduction reaction (ORR) kinetic activity on Pt, especially in the high voltage region where water is not generated or under low humidification conditions.[3–7] Carbon blacks (CBs) that have internal pores in the primary particles have been used in order to increase the surface area where Pt particles can be dispersed.[8–11] CB supports vary in their morphology and chemical properties, which play critical roles in determining the performance and stability of the catalyst.[12] Catalyst layers (CLs) prepared using CB include pores in one or more size ranges, with peaked size distributions. The smaller pores, typically in the range below approximately 100 nm, are defined as primary pores, formed in the spaces between the primary CB support particles. The primary CB support particles are usually in an aggregated form (grape-like clusters), as formed during the production process, with typical sizes of 10−100 nm. These

aggregates form larger structures, called agglomerates, and larger pores, defined as secondary pores, are formed between the agglomerates.[2,9,13–15] In the International Union of Pure and Applied Chemistry (IUPAC) Recommendations, pores are classified as macropores when the pore diameter is 50 nm or more, mesopores when the pore diameter is 2 to 50 nm, and micropores when the pore diameter is 2 nm or less. In order to focus on the internal pores of CB supports, I have defined the internal pores with diameters smaller than 10 nm in the primary particles of CB as nanopores. So far, studies have been conducted on the position of Pt particles using multiple CBs. In 1996, Uchida et al. of Matsushita Battery Industrial Company (currently known as Panasonic Co., Ltd.) published the first known work on the relationship between the primary pores of catalysts and the corresponding PEFC cell performance.[15] That work laid a foundation for today's research in this area. In that paper, in which Acetylene Black (AB), Ketjenblack (KB), and Vulcan (Vu) were used, still the subjects of present-day research, the conclusion was that AB, which has a small specific surface area, showed the best cell performance, in terms of mass activity, due to the small amount of unused platinum in the nanopores. On the other hand, recent study has also focused on techniques that utilize Pt particles in the pores of supports with large specific surface areas. Yarlagadda et al.[16] used KB, Vu, and HSC with accessible mesopores, showing that HSC had higher cell performance in the high current density (HCD) region. Ramaswamy et al. used six different CB supports to examine the relationship between micro-, meso-, and macroporosity and cell performance at HCD.[17] Harzer et al. manufactured catalysts in which Pt particle was mainly supported on the exterior or interior of the support (KB).[18] They investigated the effect of the location of the Pt particles in the interior or on the exterior of the support CB on the ORR activity and cell performance at HCD. Padgett et al. conducted a potential cycling

durability test using KB, Vu, and AB to investigate the effect of differences in the structure of the CB support on durability.[10] In addition, El Hannach et al. modeled and validated the effect of ionomer content and Pt particle loading on the nanoporous structure of the catalyst using KB.[19] They treated the changes in pore size distribution and isotherms associated with changes in the amount of ionomer using both simulations and experiments. These studies have shown that when the electrode is made, the ionomer cannot contact the Pt particles loaded inside the pores, and it is difficult to contact the ionomer with all of the Pt particles. Recent approaches are focusing on CB support structures and ionomer coverings that allow oxygen to access the Pt.[3,4,18,20] Yarlagadda et al. concluded that the ideal catalyst structure is one with internal porosity that can hold Pt particles and not contact directly with the ionomer to prevent being poisoned.[16] Ramaswamy et al. investigated pore volume and cell performance in the high current density region.[17] Improvements in the ionomer are also being made.[21–25] It is important to design an appropriate CL for improving cell performance;[6,7,26,27] however, previous study has not revealed detailed guidelines for maximizing the utilization of supported Pt. One of the factors is that HSC has many pores and its structure is complicated. Therefore, there are many unclear points such as the state of Pt particles supported in the pores, the state of ionomer covering, and the behavior of generated water during operation. Therefore, I investigated the relationships between the amount of ionomer, changes in the pore volume of the catalyst, and the cell performance. From these, I clarify how the ionomer covers the pores and derive design guidelines for the optimal CL using multiple CB supports, which lead to the increased, effective utilization of the accessible Pt particles on the surface of the nanopores in the primary particles of the CB supports. Durability tests using carbon supports have also been investigated.[28–32] Padgett et al. discussed the impact of

the carbon nanostructure on durability.[10] These studies have revealed catalyst degradation by potential cycling under H_2/N_2 (anode/cathode) gas conditions. Takei et al. investigated catalyst deterioration under various conditions assuming actual FCV operation with current cycling.[31] This durability evaluation was carried out using graphitized carbon black (GCB) with few pores; herein, I investigated the effect of the catalyst with various pore structures.

2-2. Experimental

2-2-1. Catalyst materials and fabrication of MEAs

All of the anode CLs were prepared with a CB-supported PtCo catalyst (Tanaka Kikinzoku Kogyo K.K.) with a total metal loading of 54% by weight. All of the cathode CLs were prepared from Pt particles dispersed on four different CB supports (FCX200, Cabot Corporation; ECP200L, ECP; and ECP600JD, Lion Specialty Chemicals Co., Ltd.) with a total metal loading of 40% by weight. I have simplified the nomenclature of the CB supports, referring to FCX200 as V1, ECP200L as K4, ECP as K8, and ECO600JD as K13. Anode and cathode CL inks were prepared by dispersing the catalysts in water, ethanol, and long-side-chain PFSA ionomer solution (FORBLUE i series, AGC Inc., IEC = 1.14 meq g^{-1}). The properties of the CB supports used in this study are summarized in Table 2-1. Inks were prepared using the four different catalysts. Ethanol, distilled water, and ionomer were added to the catalyst, mixed, dispersed, and allowed to stand for 15 to 18 h. Then, dispersion and defoaming treatments were performed. To prepare the catalyst-coated membranes (CCMs), the catalyst inks were directly sprayed onto the ion exchange membrane (GORE-SELECT® Membrane, W. L. Gore & Associates, Inc.) using a pulse-swirl-spray (PSS, Nordson Co. Ltd.) apparatus, and the hot plate was set at 65 °C. The

Table 2-1. Properties of the CB supports and Pt catalysts.

CB supports	Unit	V1	K4	K8	K13
Product name		FCX200	ECP200L	ECP	ECP600JD
CB species		Vulcan	Ketjenblack	Ketjenblack	Ketjenblack
Specific surface area	$m^2\ g_{\text{-carbon}}^{-1}$	141	382	778	1335
nanopore volume*	$cm^3\ g_{\text{-carbon}}^{-1}$	0.09	0.23	0.48	1.05
Catalysts	Unit	Pt/V1	Pt/K4	Pt/K8	Pt/K13
Specific surface area	$m^2\ g_{\text{-catalyst}}^{-1}$	77	192	406	741
	($m^2\ g_{\text{-carbon}}^{-1}$)	(128)	(320)	(677)	(1235)
nanopore volume*	$cm^3\ g_{\text{-catalyst}}^{-1}$	0.04	0.12	0.25	0.53
	($cm^3\ g_{\text{-carbon}}^{-1}$)	(0.07)	(0.20)	(0.42)	(0.88)

* nanopore volume indicates the total volume of pores up to 10 nm in diameter.

cathode ink was applied on one side of the membrane, and the anode ink was applied on the opposite side. The electrode was 6 cm on each side, with an area of 36 cm^2. The Pt loadings were 0.19 mg cm^{-2} for the cathode catalyst layers and 0.12 mg cm^{-2} for the anode catalyst layers. The CCMs were annealed by hot-pressing at 140 °C and 1.1 MPa for 5 min, and then, they were assembled with two gas diffusion layers (GDLs, H1509, NOK Corp.), one on each electrode.

2-2-2. Physical characterization of CB supports and catalysts and CCMs

Analysis of the surface area and pore size distribution of the CB supports and CCM was carried out using a surface area and pore size analyzer (Autosorb-iQ_3, automated gas sorption analyzer, Anton Paar GmbH). To examine the cathode catalyst after addition of the ionomer applied to the membrane, the CCM was coated with the cathode ink on both sides so that the excess weight (i.e., other than that of the membrane) was about 0.1 g. The purpose of applying the coating on both sides of the membrane was to secure an amount of sample that could be measured accurately and to reduce the exposed area of

the polymer electrolyte membrane so as to minimize the amount of N_2 adsorbed on the membrane. Degas conditions were 200 °C for 8 h on the CB supports and catalysts and 80 °C for 24 h on the CCM in an onboard degassing port. The N_2-adsorption measurements were conducted in the P/P_0 range 0.025−0.995. The specific surface area and pore size distribution were calculated by the Brunauer-Emmett-Teller (BET) method and quenched solid density functional theory (QSDFT) method, respectively. The QSDFT method was more suitable for characterization of the nanopores below 10 nm than the Barrett-Joyner-Halenda (BJH) method. In addition, the influence of roughness and nonuniformity of the surface of the CB is taken into consideration, and the reliable nanopore diameter of the CB can be calculated.[33,34] In this study, N_2 at 77 K on carbon (cylindrical porosity, QSDFT equilibrium model) was selected as the analysis model for the QSDFT method.[34–37]

2-2-3. Distribution of Pt particles

The morphology of the Pt particles was analyzed by scanning transmission electron microscopy (STEM, HD-2700, Hitachi High-Technologies Co.). From the transmission electron (TE) image, it is possible to observe all of the Pt particles that are located on the CB support surfaces (exterior) and CB support pores (interior). The Pt particles appear as black dots. From the secondary electron (SE) image, it is possible to observe Pt particles located only on the exterior as white dots.[7] The STEM instrument has a 3D holder, which enables the sample to be rotated by 180°, so that the Pt particles on the reverse side of the CB support particles can be observed, ensuring that all of the Pt particles located on the exterior are accounted for. Thus, I was able to separate the Pt particles on the exterior and interior of the CB support particles. The Pt surface area (per unit weight of Pt) was

calculated from the particle size of the Pt particles, and the interior/exterior ratio was measured by STEM.[2,9] Each Pt surface area was calculated by statistically processing 1000 or more Pt particles using 7−10 STEM images.

2-2-4. Electrochemical measurements

Electrochemical characterization measurements of the cathode CLs were carried out in a single cell evaluation device controlled using the measurement system (Fuel cell single cell evaluation system, Panasonic Production Technology Co., Ltd.). Cyclic voltammetry (CV) was performed at 80 °C and 80% relative humidity (RH) using a potentiostat (HZ-3000, Hokuto Denko Co.). The cathode was flushed with N_2, and the anode was flushed with H_2 at a flow rate of 100 mL min^{-1}. Prior to the potential sweep, the potential was maintained for 30 s at an open circuit. Then, the potential was swept back and forth from 0.05 to 1.0 V at 20 mV s^{-1}. The potential sweep was performed three times and the third time was used for the calculation of ECSA. The ECSA values were determined from the hydrogen adsorption charge referred to ΔQ_H = 0.21 mC cm^{-2}, which is the amount of electric charge generated when hydrogen is adsorbed at unity coverage on a polycrystalline Pt surface. The current−potential polarization ($I-V$) curves of the membrane electrode assemblies (MEAs) were carried out in a single-cell evaluation device by supplying hydrogen and air to the anode and cathode, respectively, at 80 °C and 80% RH under ambient pressure. The flow rates of all gases were controlled using mass flow controllers; the utilizations of the reactant gases were 40% O_2 (U_o = 40) and 80% H_2 (U_f = 80). The $I-V$ curves were measured under quasistatic operating conditions with a measurement time of 5 min at each point. Overvoltage isolation was divided into reaction overvoltage and diffusion overvoltage. The reaction overvoltage was determined as the

difference from the theoretical open-circuit voltage (OCV) by obtaining the intercept and slope in the low current density region, where there is almost no diffusion resistance. For the diffusion overvoltage, the voltage when there is no diffusion resistance is obtained using the intercept and slope obtained from the low current density region and is defined as the difference from the IR free voltage.

2-2-5. Load cycling operation

Figure 2-1 shows the protocol of the durability test and procedure of the degradation degree evaluation. In the durability test, the operation was performed by cycling between

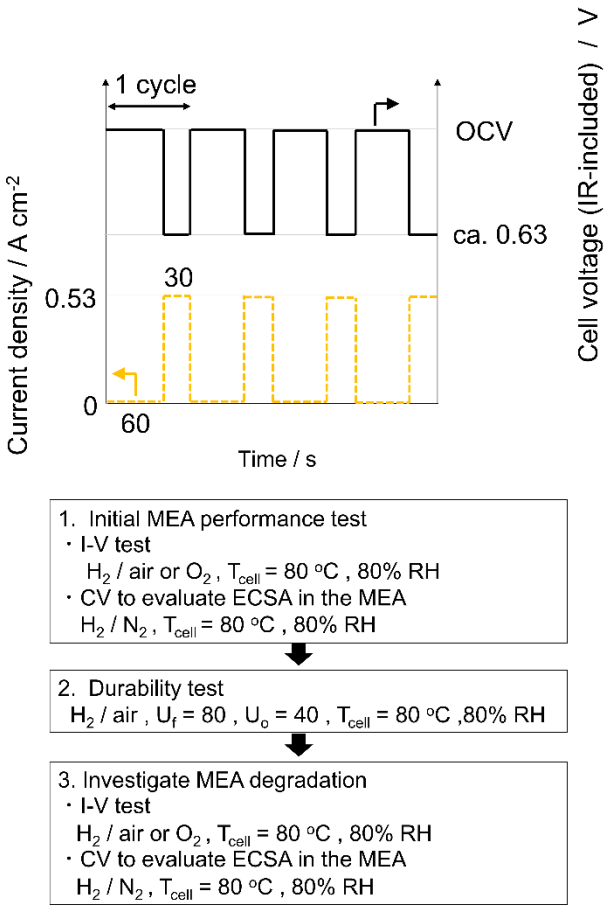

Figure 2-1. Protocol for the durability test and experimental procedure for investigating the effects of catalyst degradation.

OCV and 0.53 A cm^{-2}, and it was held for 60 s at OCV and 30 s at 0.53 A cm^{-2}. The operation of the OCV and load was set as one cycle, and 10,000 cycles were performed. The cell temperature was 80 °C; air was supplied to the cathode, and H_2 was supplied to the anode at 80% RH. The cell was operated at $U_o = 40$ and $U_f = 80$. Before and after the durability test, the $I-V$ curve and CV were measured to investigate the degree of deterioration.

2-2-6. Observation of catalyst morphology after the durability test

After the durability test, a cross-sectional sample of the MEA was prepared using the focused ion beam device (FIB, Hitachi High-Tech Co.). This enables the depth direction analysis of the MEA. Using the prepared sample, a TE image was obtained for Pt particles and a Z-contrast (ZC) image was obtained for the membrane using STEM. Concentration changes of Pt in the cathode catalyst layer and polymer electrolyte membrane of the MEAs were analyzed using a field emission-electron probe microanalyzer (FE-EPMA, JEOL Ltd. JXA-8530F) with a Pt line scan.

2-3. Results and discussion

2-3-1. Microstructure analysis of CB supports and Pt particle distribution of the catalysts before and after the Pt loading

I investigated four different cathode catalysts in this study. I used V1, K4, K8, and K13 as CB supports. V1 refers to Vulcan (100 $m^2\ g^{-1}$), and K4, K8, and K13 refer to Ketjenblack with 400, 800, and 1300 $m^2\ g^{-1}$ nominal specific surface areas, respectively. Table 2-1 shows the accurate specific surface areas and pore volumes in the nanopore region of the CB supports and catalysts. Figure 2-2 shows the pore size distribution in the

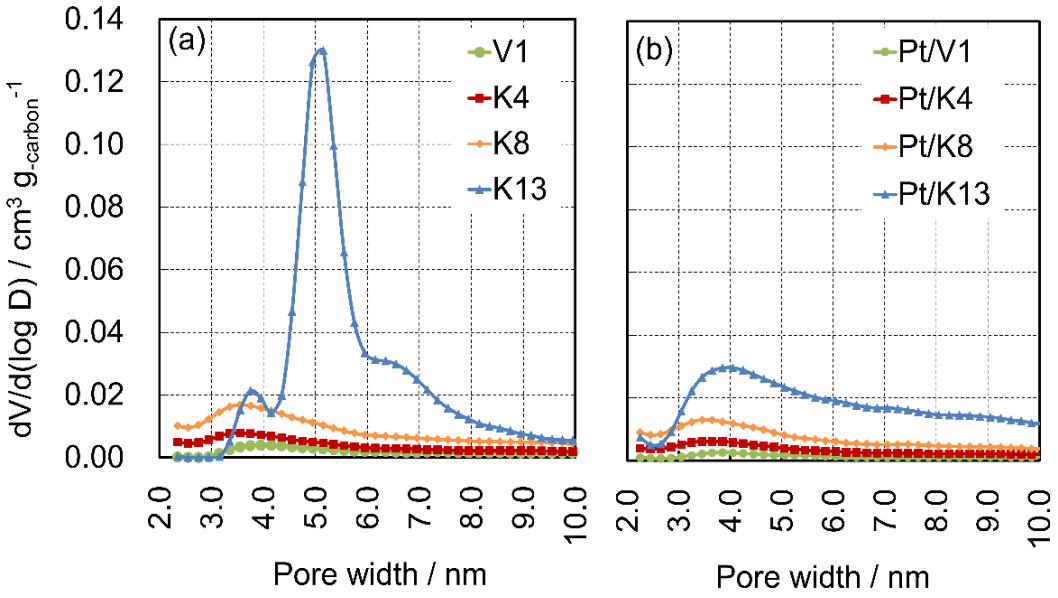

Figure 2-2. Pore size distribution per unit mass of carbon of (a) CB supports and (b) catalysts.

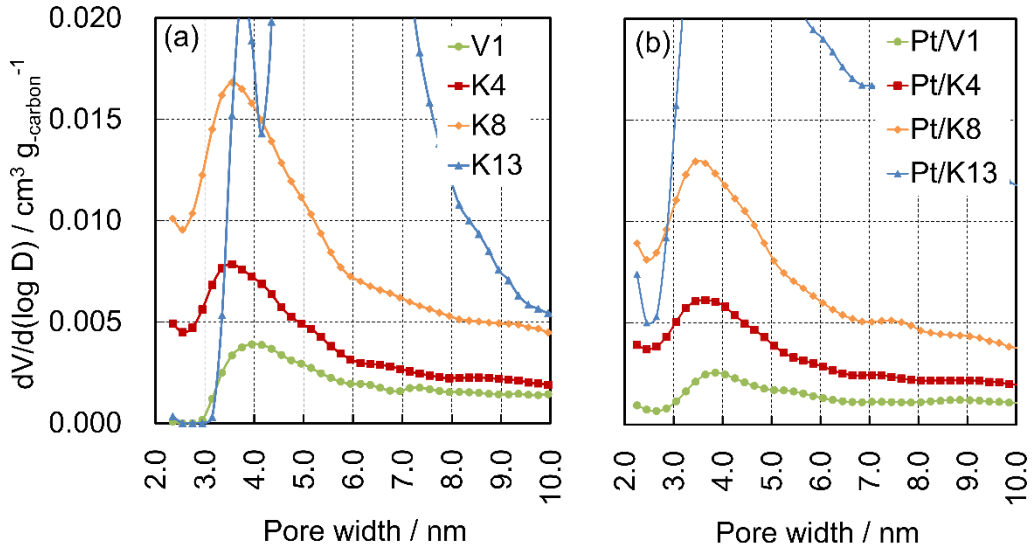

Figure 2-3. (a) Pore size distribution of CB supports with enlarged scale of the y-axis. (b) Pore size distribution of catalysts with enlarged scale of the y-axis.

2 to 10 nm range per unit mass of carbon for these CB supports and catalysts. A large difference appeared in the pore volume distribution; the order of pore volume for both

CB supports and catalysts was Pt/V1 < Pt/K4 < Pt/K8 < Pt/K13. These values increased with increasing specific surface area of the CB support. In the pore distributions for these CB supports (V1, K4, and K8), a small peak appeared at a pore size of about 3.6 nm, and

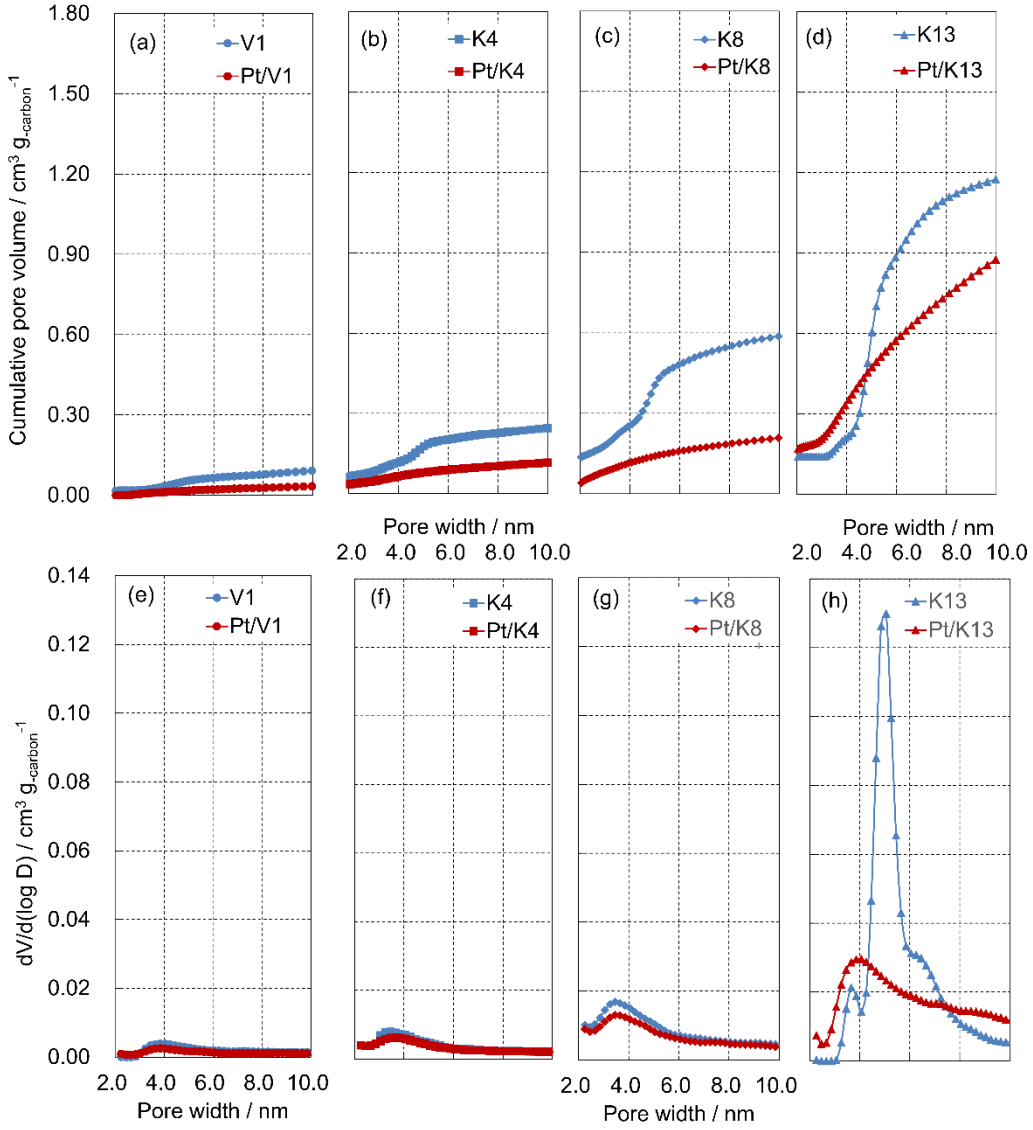

Figure 2-4. Change of the nanopore cumulative volume of the CB supports after Pt loading calculated by the QSDFT analysis of (a) V1 and Pt/V1, (b) K4 and Pt/K4, (c) K8 and PtK8 and (d) K13 and Pt/K13. Change of the pore size distribution of the CB supports after Pt loading calculated by the QSDFT analysis of (e) V1 and Pt/V1, (f) K4 and Pt/K4, (g) K8 and PtK8 and (h) K13 and Pt/K13.

the pore distribution of the catalyst produced by loading Pt using these CB supports was hardly changed. Figure 2-3 shows the pore size distributions with the vertical axis expanded so that the peaks for V1, K4, and K8 can be distinguished easily. In the case of K13, a small peak appeared at a pore size of about 3.8 nm and a large peak at about 5.0 nm, and the peak for Pt/K13 using this CB support broadened and was centered at about 3.8 nm. Both before and after Pt loading, the peaks for this CB support were larger than those of other catalysts. Large peaks were not observed in the pore size region of 10 nm or more. After loading Pt, the volume of pores having a pore diameter of 3−6 nm selectively decreased. These results indicate that the Pt/K13 catalyst, supported on K13, still had a much larger pore volume than those of the other catalysts and also that the Pt particles became lodged in the 3−6 nm diameter pores of the CB support. With the exception of Pt/K13, the cumulative volumes of the catalysts decreased to about one-third of the volume of the CB support due to the Pt loading. On the other hand, for Pt/K13, the cumulative pore volume decreased by only about 20% (shown in Figure 2-4) despite the high ratio of Pt particles in the interior. Compared to other catalysts, Pt/K13 was prepared from a CB support with many large-diameter pores and relatively small Pt particles, and thus, many Pt particles might be loaded in the pores without blocking the pore entrances. The morphologies of the catalysts were analyzed by STEM. The TE and SE images at 0 and 180°, together with the percentages of exterior and interior Pt particles, are shown in Figure 2-5. The Pt particle distributions on the exterior and interior surfaces of the CB support were determined from these images. The Pt particles that are visible in the TE image but not in the SE image are the interior Pt particles. In the TE images of Pt/K13 (Figure 2-5r,s), small Pt particles were observed to be dispersed, and in the SE images (Figure 2-5p,q), the particle number decreased, and the interparticle distances were

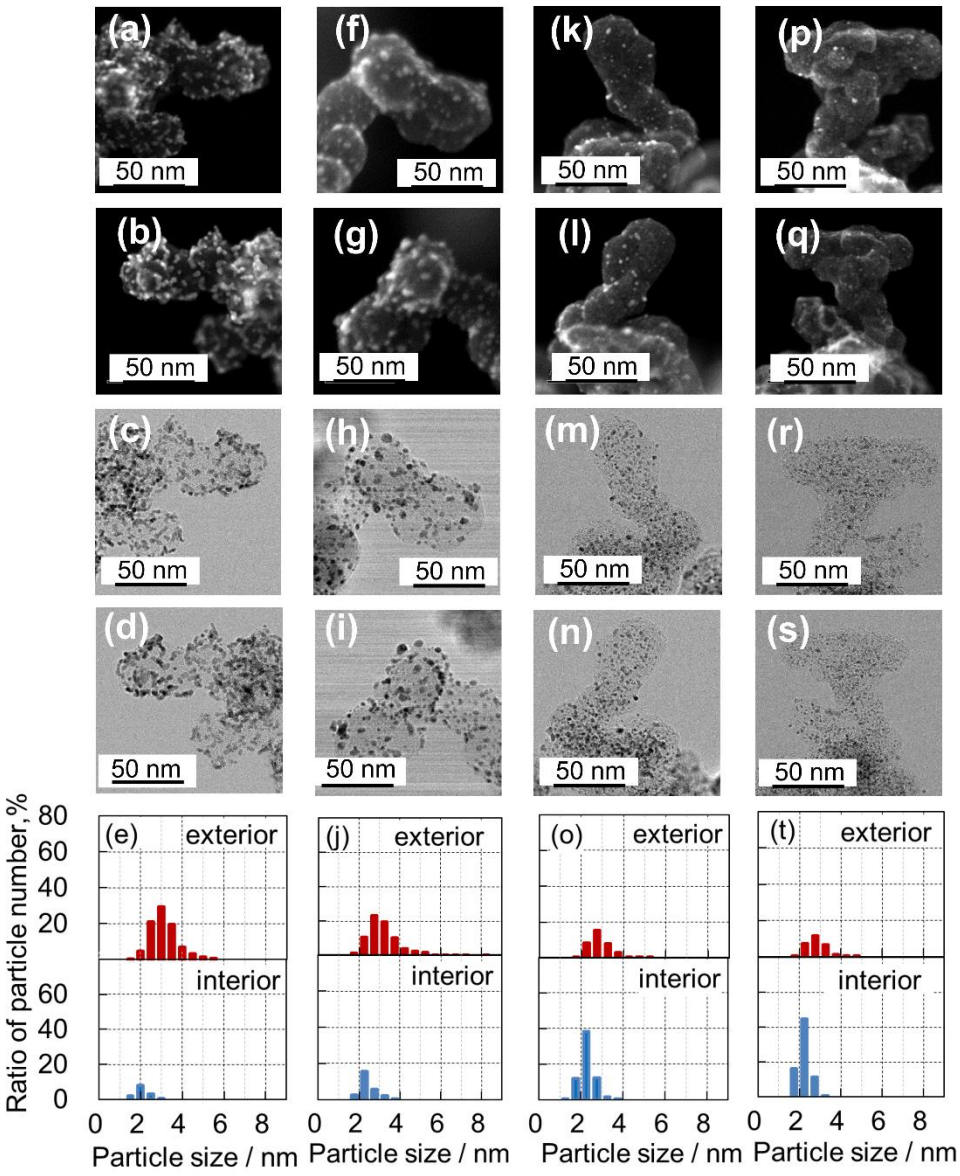

Figure 2-5. STEM images and size distribution of Pt particles interior and exterior the catalysts. (a,b) 0 and 180° SE image of Pt/V1, (c,d) 0 and 180° TE image of Pt/V1, (e) Pt distribution of Pt/V1, (f,g) 0 and 180° SE image of Pt/K4, (h,i) 0 and 180° TE image of Pt/K4, (j) Pt distribution of Pt/K4, (k,l) 0 and 180° SE image of Pt/K8, (m,n) 0 and 180° TE image of Pt/K8, (o) Pt distribution of Pt/K8, (p,q) 0 and 180° SE image of Pt/K13, (r,s) 0 and 180° TE image of Pt/K13, and (t) Pt distribution of Pt/K13.

observed to be wide. These results indicate that many of the Pt particles in Pt/K13 are supported on the surface of the inner nanopores of the K13 (73% inside, 23% outside).

Table 2-2. Sizes of Pt particles located on the exterior and interior of the CB support particles.

Catalysts		Particle size / nm	Frequency, %	Pt surface area / $m^2 g^{-1}$ **
Pt/V1	Interior	2.4 ± 0.3	13	6 ± 0.1
	Exterior	3.4 ± 0.6	87	78 ± 2.5
Pt/K4	Interior	2.4 ± 0.3	25	14 ±0.2
	Exterior	3.2 ± 0.8	75	77 ±4.5
Pt/K8	Interior	2.3 ± 0.3	64	60 ±1.1
	Exterior	2.8 ± 0.5	36	50 ±1.5
Pt/K13	Interior	2.2 ± 0.3	73	72 ±1.2
	Exterior	2.8 ± 0.4	27	43 ±1.0

** It is a calculated value obtained by statistical processing from the STEM image.

On the other hand, for Pt/V1, many of the Pt particles observed in the TE images (Figure 2-5a,b) are also observed in the SE images (Figure 2-5c,d). In the case of Pt/V1, many Pt particles were supported on the exterior surface (interior 13% exterior 83%). In the case of both Pt/K8 and Pt/K4, intermediate tendencies between Pt/K13 and Pt/V1 were observed. The Pt particle location percentages of interior and exterior for Pt/K8 were 64% and 36%, respectively, and those for Pt/K4 were 25% and 75%. Table 2-2 summarizes the interior and exterior results of these Pt particle sizes, the Pt particle frequency percentage, and the Pt surface area for those catalysts. These results also indicate that the use of a more porous CB support leads to an increased frequency of Pt particles in the interior nanopores. The Pt particles on the surfaces of the interior nanopores were smaller than those on the exterior surfaces for all catalysts. While the Pt particle sizes in the interior nanopores were nearly the same (2.2−2.4 nm) for all catalysts, those on the exterior differed. On the exterior surface of the CB primary particles, Pt/V1, with the smallest surface area, exhibited the largest Pt particle size (3.4 nm), and Pt/K13, with the largest surface area, exhibited the smallest particle size (2.8 nm). From these results, I can

conclude that a catalyst using a CB support with a larger specific surface area is dispersed with smaller Pt particles, and the exterior Pt particles coalesce via the aggregation of small Pt particles during the Pt loading process. A catalyst using a CB support with a smaller specific surface area is more likely to undergo aggregation, resulting in a larger Pt particle size. The dispersion state of the Pt particles depends largely on the specific surface area of the CB support, and the larger specific surface area can be effectively utilized and leads to a dispersion of smaller Pt particles.

2-3-2. Nanopore volume of catalyst after the addition of ionomer

I focused on the relationship between accessible Pt and nanopores in order to research the effect of Pt particles inside the pores of the primary particles of the CB support on cell performance and durability. To focus on the internal pores of the CB supports, I will discuss the internal pores with diameters smaller than 10 nm as nanopores in the primary CB particles. At the present time, a method for directly observing the ionomer covering state on a CB support with low crystallinity is under study and has not yet been established. However, El Hannach et al. interpreted that, in a catalyst using K8, the surfaces of pores (primary pores, ~5 nm), of the same size as the nanopores I have focused on, are blocked by the ionomer, and the ionomer in the pores impedes the gas access into the pores.[19] In response to these interpretations of previous studies, similar to the studies of accessible Pt by Padgett et al.[10] and Yarlagadda et al.,[16] I found that, in the case of K13, nanopores exist with a non-negligible pore volume inside the primary CB particles. I sought to propose the status of ionomer intrusion and the blocking of nanopore entrances based on the verification of the experimental data. Therefore, I proposed the state of ionomer covering in nanopores and the effect of ionomer covering, based on the behavior of

changes in nanopore volumes obtained from isotherms and the effect on cell performance, depending on the amount of ionomer. Many studies have used N_2-adsorption measurements to investigate changes in the pore structure of CB supports.[2,18,19,38] In the N_2-adsorption measurements, the pressure is varied, and the resulting adsorption/desorption amount is measured versus time. Since the N_2-adsorption measurement is performed at 77 K, the state of the water-free ionomer is measured. The isotherm was obtained by plotting the results with the relative pressure (P/P_0) on the horizontal axis and the amount of N_2 adsorbed on the surface of the substance on the vertical axis. Figure 2-6a shows the isotherms of I/C = 0.9 for Pt/K8 and Pt/K13. Hysteresis is observed in the isotherm where the adsorption and desorption volumes do not match. These isotherms are defined as H3 or H4 types in the IUPAC classification.[39] H3- or H4-type hysteresis loops are typical for micro-mesoporous materials and indicate that the catalyst has narrow slit-like pores or ink bottle-type pores.[2,19,39–42] I consider the K8 and K13 isotherms to be a unique combination of H3 and H4 types. Many studies have been conducted on the structure of materials and isotherms, and it is useful to continue further studies. The decrease in hysteresis means that either the pores of the CB support are more cylindrical, or the pore volume is reduced, resulting in a more spherical shape. The hysteresis volume and the ionomer weight at each ionomer and CB weight ratio (I/C) are presented in Figure 2-6b. Here, the hysteresis volume is defined as the difference between the volume of the isotherm on the desorption side and the adsorption side when $P/P_0 = 0.5$. The reason why I adopted the value of $P/P_0 = 0.5$ was based on the study by El Hannach et al. They have shown in their study that the isotherm ($0.35 < P/P_0 < 0.7$) corresponds to the filling of the primary pores by capillary condensation. These pores have smaller diameters (~5 nm) than the secondary pores and therefore are filled

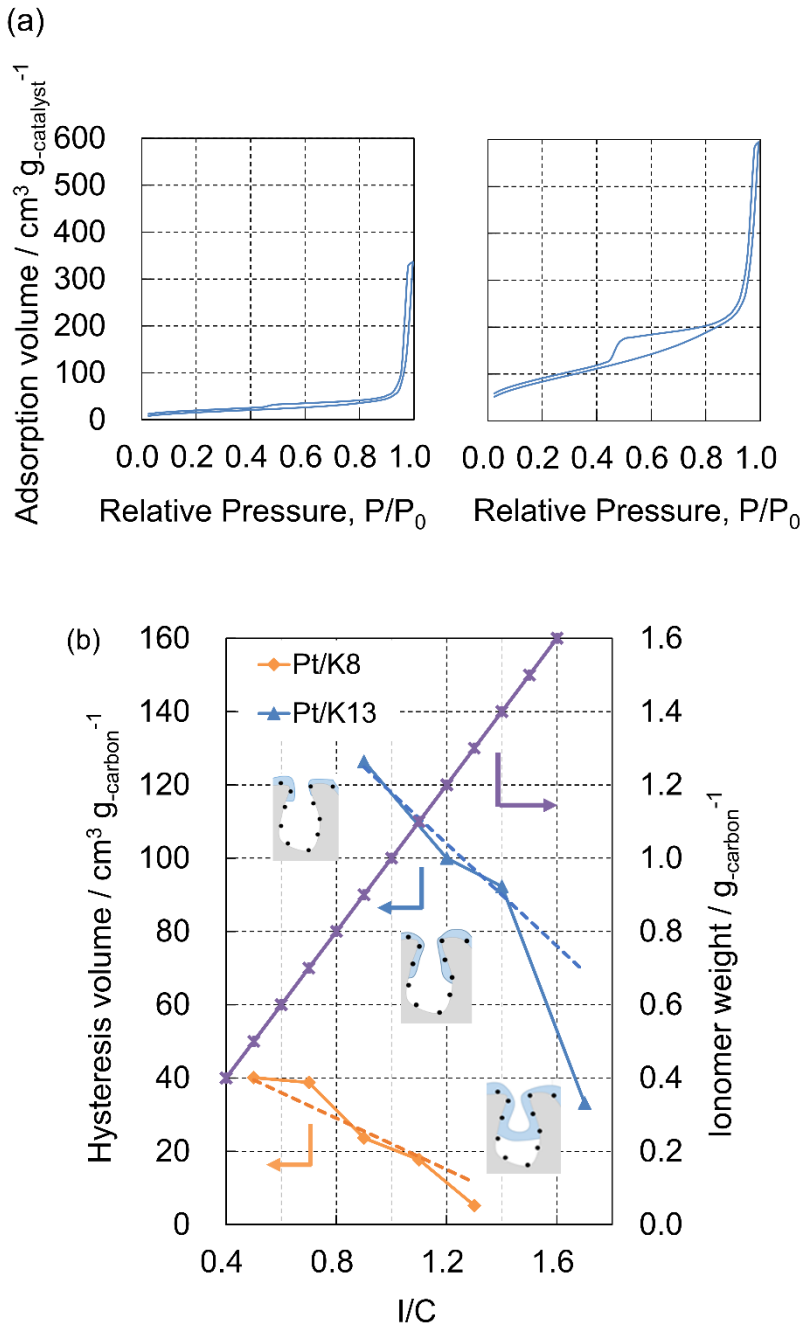

Figure 2-6. (a) Isotherms of Pt/K8 (left) and Pt/K13 (right) with I/C = 0.9. (b) Hysteresis volume at P/P_0 = 0.5 of the catalysts after the ionomer addition and the ionomer weight at each I/C.

first.[19] Since this P/P_0 range is consistent with the nanopores I am focusing on, I simply set the median P/P_0 = 0.5 of the abovementioned range as the volume corresponding to

nanopores. In a comparison of the hysteresis volumes between the Pt/K8 and Pt/K13 catalysts with varying ionomer content, that of the Pt/K13 catalyst, with larger specific surface area, showed the larger hysteresis volume. For each catalyst, the hysteresis tended similarly to decrease as the I/C increased. The weight of ionomer increased in proportion to I/C; on the other hand, the change in hysteresis volumes had inflection points. Sudden drops of the hysteresis volume occurred at I/C 1.3 (Pt/K8) and I/C 1.7 (Pt/K13). The decrease for Pt/K13 was clearer than that of Pt/K8. Although I/C = 0 was not measured in this experiment, the effects of K8 on isotherms only with CB support, after Pt loading, and with ionomer were discussed by El Hannach et al.[19] In addition, K13 was studied by Delaporte et al., who used K13 and PVDF (polyvinylidene difluoride) binder to measure isotherms without adding an ionomeric binder.[39] The fact that the hysteresis decreased as I/C increased suggests that the ink bottle-type pores of the catalyst were filled with the ionomer. It is considered that the hysteresis volume should decrease linearly as the ionomer fills the pores, if the ionomer penetrates along the pore walls. However, a phenomenon in which the hysteresis volume sharply decreases means that the pore volume suddenly decreases and suggests that the entrances of the pores have been blocked. These results can be explained as follows: the ionomer penetrated gradually into the pores, and the pores filled linearly up to I/C 1.1 for Pt/K8 and I/C 1.4 for Pt/K13. Then, up to I/C 1.3 for Pt/K8 and I/C 1.7 for Pt/K13, the ionomer might have blocked the pore entrances. I have inserted schematic diagrams, which suggest the distributions of both ionomer and Pt particles in the interior nanopores of Pt/K13 with varying ionomer content, as shown in Figure 2-6b. These results also indicate that the effect of ionomer content on the active area of the Pt particle is complicated for the HSC support, which has a large interior pore volume of the primary CB particles. More specifically, it is expected that the

ionomer exists in various states, for example, covering with a uniform thickness on the surface of the CB support particles, covering with a nonuniform thickness, and blocking the entrances of the pores. The effects of the Pt particles in the interior CB nanopores, which are either covered or not covered by the ionomer, on the fuel cell performance are considered to depend upon this coverage and will vary with the conditions, that is, current density and supplied gas humidity. By collating the abovementioned results with the cell performance, it is considered that the design guidelines for the catalyst and the ionomer for maximizing the cell performance can be clarified.

2-3-3. ECSA and cell performance of catalysts

Figure 2-7a shows the dependence of the ECSA for each catalyst with relation to the ionomer content at 80 °C and 80% RH. The ECSA values for Pt/K8 and Pt/K13 exhibited relatively high values and volcano-shaped dependence on the ionomer content. Those for Pt/K4 exhibited mid-range values and were nearly constant for I/C larger than 0.4. Those for Pt/V1 exhibited the lowest values, with significant scatter. The maximum values for Pt/K8 and Pt/K13 were nearly the same but were observed at different ionomer contents (I/C 0.9 for Pt/K8 and at I/C 1.1 for Pt/K13). From these results, I consider that, in the case of the cathodes using Pt/K8 and Pt/K13, the ECSA values increased with increasing ionomer ratio up to I/C 0.9 in Pt/K8 and I/C 1.1 in Pt/K13, due to the ionomer impregnation in the CB nanopores, and then decreased because the ionomer blocked the entrances of the nanopores. Previous research has shown that 73% of the total Pt was utilized in the MEA and 62% of the Pt particles were present on the exterior of the CB surface, with 38% in the interior, at an optimum I/C value of 0.7. The Nafion ionomer (DE521, DuPont) was impregnated into the nanopores of a similar Ketjenblack support

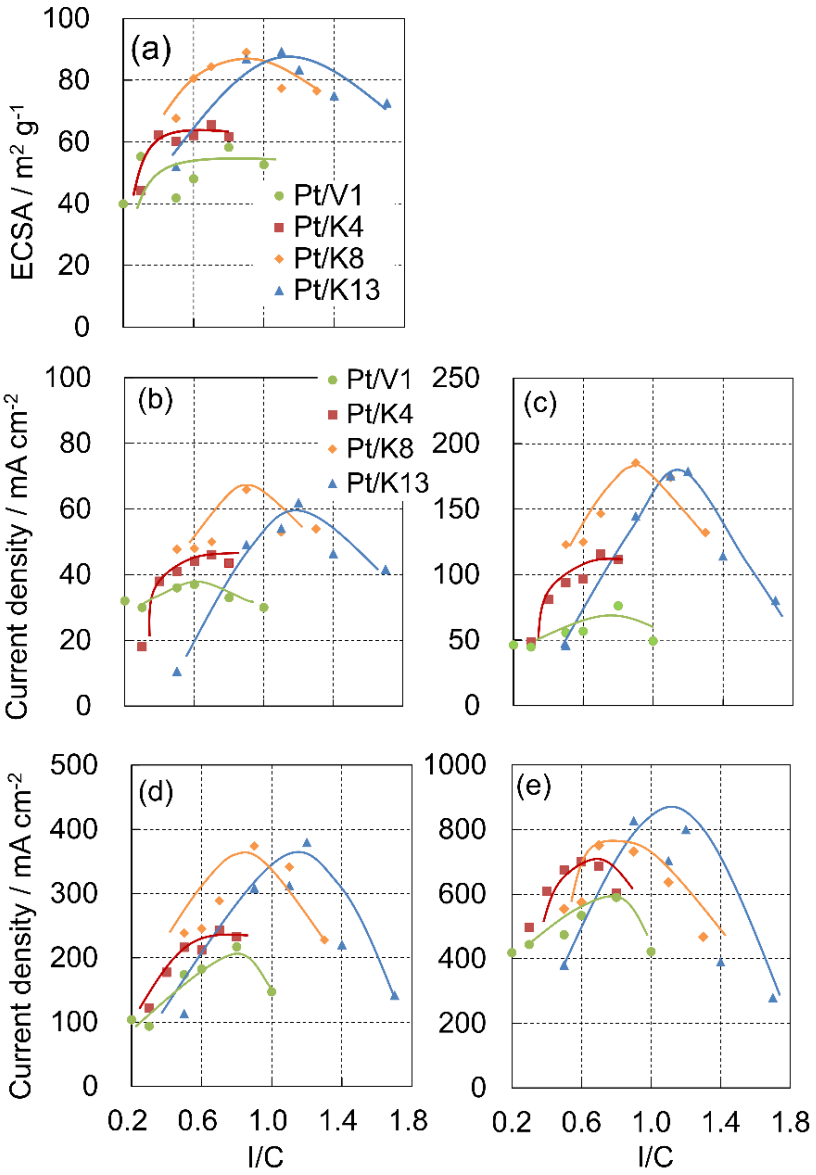

Figure 2-7. Dependence of both (a) ECSA and the current density at various cell voltages: (b) 0.85, (c) 0.80, (d) 0.75, and (e) 0.60 V for each catalyst with relation to the ionomer content at 80 °C and 80% RH.

(Pt 50 wt %) and covered the Pt particles present in the interior, yielding approximately 10% as the utilization value.[9] The ECSA value was different from the Pt surface area calculated from the STEM image most likely because the ionomer was not able to cover the Pt particles in the pore interiors. In another study, the optimum I/C for Aquivion

ionomer (D70-20BS) and Ketjenblack support (Pt 30 wt %), which has 62% interior Pt surface area, was 0.7.[2] The change in the optimum values to I/C 0.9 in Pt/K8 using AGC ionomer and Ketjenblack (Pt 40 wt %) is considered to increase because of the difference of both ionomer and the percentage of interior Pt surface area (60%). Since Pt/K13 had a low exterior Pt percentage, the ECSA was thought to be smaller than that of Pt/K8, but, as shown in Figure 2-2, it exhibited a similar value. The reason is considered to be that there were many nanopores with large diameters in the Pt/K13 catalyst, and the ionomer covered even deeper in the nanopores than those in Pt/K8 with increasing ionomer ratio. Moreover, Pt/K13 had a larger specific surface area, and the ionomer intruded deeply into the nanopores so that the amount of ionomer required to reach the maximum ECSA value was large. The reason for ECSA values decreasing for I/C values greater than the optimum is unclear but might due to a decrease in the number of proton pathways in the ionomer existing in the nanopores under the unsaturated humidity conditions (80% RH). These volcano-like relationships also occurred for the cell performance. On the other hand, Pt/K4 showed a constant value; thus, it is considered that the nanopores were filled with ionomer for I/C values of 0.4 or higher. In the case of Pt/V1, the CB support had few interior nanopores. The scattering of the ECSA values is considered to be due to a nonuniform distribution of the ionomer coverage, and the values were low due to the large particle size and low Pt surface area (see Table 2-2). The I/C values at which the N_2-adsorption measurement decreased were less than those with the highest ECSA. The reason is considered to be that, for the N_2-adsorption measurement, the ionomer did not contain water, and, in the case of the ECSA evaluation, since the RH was 80% and water was also generated electrochemically due to the fact that the ECSA was evaluated after activation, the ionomer contained water and thus swelled. The ionomer water uptake after

activation was about 20%.[21] The ionomer swelling led to decreases in the optimum I/C values, for example, I/C from 1.1 to 0.9 in Pt/K8 and I/C from 1.4 to 1.1 in Pt/K13. These results indicate that the nanopores, after activation, were blocked at lower I/C values than those for the N_2-adsorption measurement. Figure 2-7b–e shows the current density at various potentials for each catalyst with relation to the ionomer content at 80 °C and 80% RH. The measurement cell used in this study is one that is designed for a stationary fuel cell (Ene-Farm), with extremely low pressure loss. In a comparison of the pressure losses on cells with the same 29.2 cm^2 electrode area, the value for the Ene-Farm type cell was 0.05 kPa at 0.2 A cm^{-2} and that for the standard JARI (Japan Automobile Research Institute) cell was 1.40 kPa at 0.2 A cm^{-2}. Since the flow velocity and oxygen partial pressure were low due to the multiflow channel structure, there were several types of overvoltage, particularly concentration and transport, and the cell performances were lower than those for FCV applications. Nevertheless, I believe that the present results are useful and applicable for FCV-type cells. Indeed, there are no major differences in the selection of catalysts and ionomers or the method of preparing the catalyst layers. The current densities for Pt/K8 and Pt/K13 also exhibited a volcano-shaped dependence on the ionomer content and relatively high values in comparison with Pt/K4 for all cathode potential regions. In the high potential regions (0.85 V, 0.80 V), the cell performance for Pt/K8 was higher than that of Pt/K13 but that of Pt/K13 improved as the potential decreased below 0.75 V and was higher than that of Pt/K8. The ECSA values at optimal I/C for Pt/K8 (I/C 0.9) and Pt/K13 (I/C 1.1) were nearly the same, but the cell performances with relation to the cathode potential differed. However, the optimum I/C at each cathode potential hardly changed. These results indicate that the Pt utilization with relation to the current density was nearly the same, suggesting that the generated water

did not increase the active reaction area, and the Pt particles inside the blocked interior nanopore did not become activated. The performance improvement for Pt/K13 at potentials less than 0.75 V, compared with Pt/K8, suggests that the increase in the generated water led to increased effectiveness[43] of Pt particles outside the blocked interior nanopores. In the lower cathode potential region (Figure 2-7e), the performance of Pt/K13 was clearly improved. The reason is considered to be that a large amount of generated water swelled the ionomer and increased the proton conductivity of the ionomer, improving the proton pathways for the Pt/K13 cathode. The thinly covered ionomer and generated water would also lead to the prevention of poisoning of the Pt surface by the ionomer.[16–18] The presence of many large nanopores in Pt/K13 is also considered to contribute to the improvement of the oxygen transport. According to Yarlagadda et al., sufficient pore volume in the 4 to 7 nm diameter range mitigates the local oxygen resistance.[16] On the other hand, the low cell performance of Pt/K4 is considered to stem from the large Pt particle size and low ECSA; in addition, because 75% of Pt particles were present in the exterior, many were poisoned by the relatively thick ionomer.[5,16,17] From these results, I conclude that Pt/K8 is suitable for stationary fuel cells that operate in the low current density region (high voltage region), and Pt/K13 is also suitable for the requirement of higher output in the intermediate current density region under near-atmospheric pressure (low voltage region).

2-3-4. Electrochemical evaluations before and after load cycling operation

Figure 2-8 shows the $I-V$ curves for various catalysts before and after the durability test. The beginning of test (BOT) indicates the initial evaluation after activation, and the end of test (EOT) indicates the evaluation after 10,000 cycles. The I/C values of the cathode

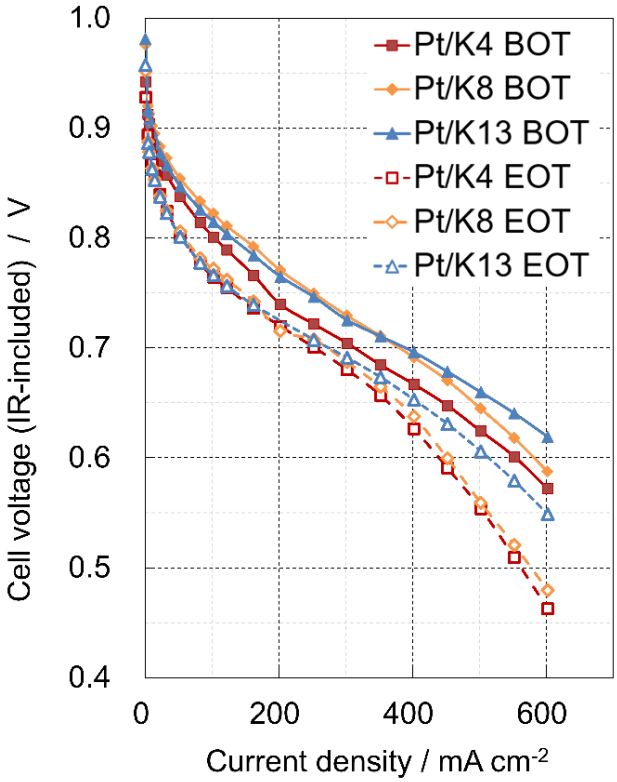

Figure 2-8. Polarization curves before (BOT) and after (EOT) the 10,000-cycle durability test.

CLs that were used for the durability evaluations were the optimal values, that is, I/C 0.7 for Pt/K4, I/C 0.9 for Pt/K8, and I/C 0.9 for Pt/K13, respectively. The cell using the Pt/K13 cathode catalyst exhibited high BOT performance and maintained high cell performance after the durability test. In particular, the cell voltages for the Pt/K4 and Pt/K8 cathode catalysts in the high current density region of 0.3 A cm^{-2} or more dropped sharply, but that for Pt/K13 maintained a relatively high cell performance. The BOT performance of the cell using the Pt/K8 catalyst was higher than that for Pt/K4, but the EOT performances of both cells (Pt/K4 and Pt/K8) were almost the same. The deterioration of Pt/K8 was larger than that of Pt/K4. As shown in Table 2-2 and Figure 2-5, Pt/K13 had smaller Pt particles and higher dispersion than those of others. In addition,

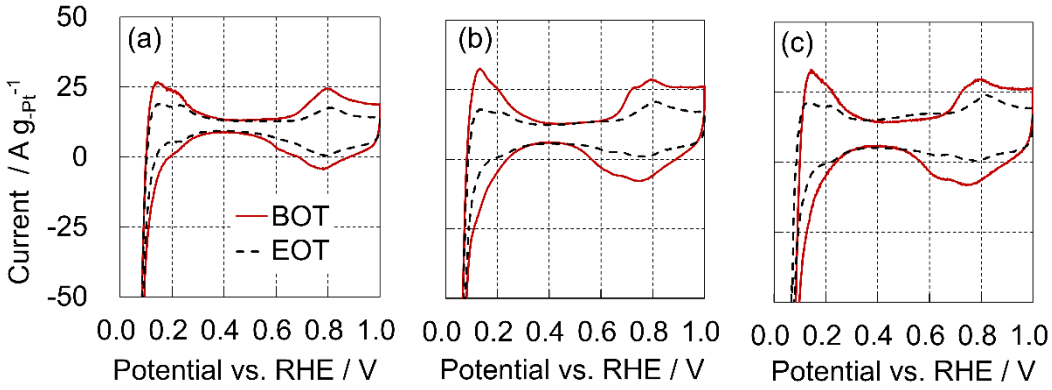

Figure 2-9. Change in cyclic voltammograms for (a) Pt/K4, (b) Pt/K8, and (c) Pt/K13 before and after the durability test.

Table2-3. Changes in ECSA and overvoltage percentages before and after the durability test.

Catalysts		Pt/K4	Pt/K8	Pt/K13
ECSA / m^2 g^{-1}	BOT	65	82	87
	EOT	35	43	49
Reaction overvoltage		+13%	+20%	+16%
Diffusion overvoltage		+42%	+28%	+10%

the CB support of Pt/K13 (K13) had a large specific surface area, so that the distances between the Pt particles would be longer than those of others. The average distances between Pt particles calculated from the average Pt particle sizes listed in Table 2-2 are 8 nm for Pt/V1, 13 nm for Pt/K4, 16 nm for Pt/K8, and 20 nm for Pt/K13. For the longer average interparticle distances, the Pt particle aggregation would be more effectively suppressed. The longer distance between the Pt particles of Pt/K13 is considered to be one of the factors contributing to the higher EOT performance. Figure 2-9 shows the comparison of CVs between BOT and EOT for the cathodes using the various catalysts. The electric double layer capacities of all cathodes hardly changed before versus after the durability test. These results indicate that the CB support was hardly oxidized (corrosion)

and suggest that Pt particle detachment due to carbon corrosion was not a major factor in the deterioration of cell performance. Table 2-3 shows the values of ECSA and the percentages of change in overvoltage before and after the durability test, for the various cathode catalysts. All ECSA values had decreased significantly at EOT, by 49%, 48%, and 44% for Pt/V4, Pt/K8, and Pt/K13, respectively; the percentage decrease for Pt/K13 was the smallest, and it maintained the highest ECSA value at EOT. I evaluated individually the overvoltage changes in both reaction and diffusion for each cathode. These differences of reaction overvoltage changes were relatively small, but those of the diffusion overvoltage changes were larger, increasing 42% for Pt/K4, 28% for Pt/K8, and 10% for Pt/K13. These results suggest that the change in Pt particle distribution affected the overvoltage increases.

2-3-5. Morphologies of catalysts before and after the durability test

Figure 2-10a−f shows the TE images of various catalysts after the durability test. Figure 2-10g−l shows the Pt particle-size distributions in CLs on the GDL side or membrane side before and after the durability test. Figure 2-10m−o shows the Pt particle distributions using ZC images in the membrane after the durability test. Figure 2-10a,d shows images of catalysts on the GDL side and membrane side of Pt/K4, respectively. Similarly, Figure 2-10b,e shows images for Pt/K8 and Figure 2-10c,f for Pt/K13. After the durability test, all of the Pt particle sizes became obviously larger (Figure 2-5). The Pt particle size and Pt surface area before and after the durability test are presented in Table 2-4. There are two mechanisms for coarsening of Pt particles in fuel cell catalysts, Ostwald ripening, and agglomeration or aggregation. In Ostwald ripening, Pt dissolves electrochemically and reprecipitates on the surfaces of adjacent Pt particles.[44] Agglomeration involves the

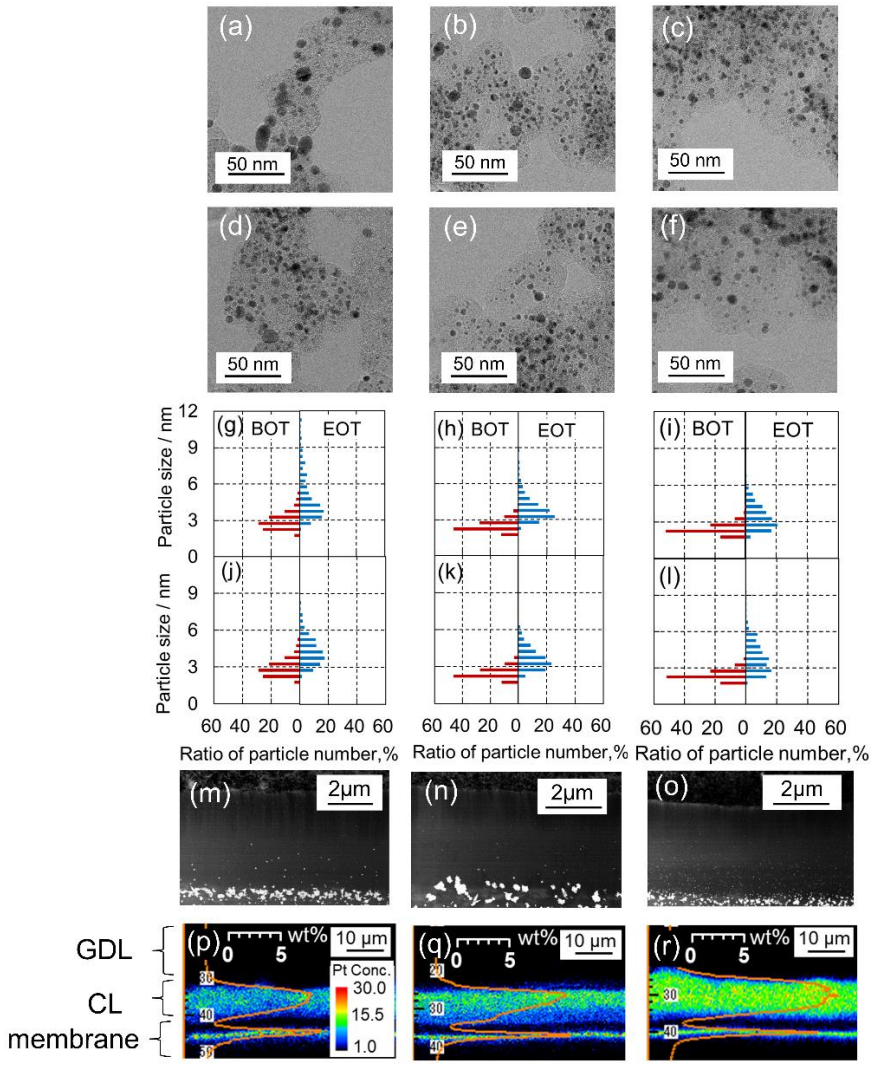

Figure 2-10. Observation catalysts and membrane morphology and change in Pt particle before and after the durability test. The TE image of the CL on the GDL side after the durability test of (a) Pt/ K4, (b) Pt/K8, and (c) Pt/K13. The TE image of the CL on the membrane side after the durability test of (d) Pt/K4, (e) Pt/K8, and (f) Pt/K13. Pt particle size distribution of the catalyst on the GDL side before and after the durability test of (g) Pt/K4, (h) Pt/K8, and (i) Pt/K13. Pt particle size distribution of the catalyst on the membrane side before and after the durability test of (j) Pt/K4, (k) Pt/K8, and (l) Pt/K13. The ZC image of the membrane after the durability test of (m) Pt/K4, (n) Pt/K8, and (o) Pt/K13. Concentration changes in Pt in the cathode catalyst layer and electrolyte membrane of (p) Pt/K4, (q) Pt/K8, and (r) Pt/K13 by EPMA and Pt line scan.

movement and joining of Pt particles on the support surface, perhaps initially without

Table 2-4. Size of Pt particles before and after the durability Test

	Particle size / nm			Pt surface area / $m^2\ g^{-1}$		
Catalysts	Pt/K4	Pt/K8	Pt/K13	Pt/K4	Pt/K8	Pt/K13
BOT	3.0 ± 0.7	2.5 ± 0.4	2.4 ± 0.3	91	111	115
EOT	4.9 ± 1.8	4.1 ± 1.2	3.6 ± 1.1	57	68	76

bonding strongly. However, if these Pt particles are exposed to high potential, high temperature, or cycles of potential or heat, they can become strongly bonded via the rearrangement of Pt atoms.[45] Ostwald ripening and aggregation form Pt particles with different shapes. Padgett et al. found that Ostwald ripening leads to particles becoming spherical, whereas aggregation leads to elongated particles.[10] The Pt particles on the GDL side of Pt/K8 and Pt/K13 (Figure 2-10b,c) were mostly circular. Pt particles with both elongated and round shapes were observed for Pt/K4 (Figure 2-5a). On the membrane side, circular Pt particles were mainly observed for all catalysts (Figure 2-5d−e). These results suggest that the coarsening of Pt/K8 and Pt/K13 was mainly caused by Ostwald ripening, while that for the GDL side of Pt/K4 was caused by both aggregation and Ostwald ripening; on the membrane side, the Pt particles were coarsened due to Ostwald ripening for all catalysts. From these results, I conclude that the movement of Pt particles would be limited, and coarsening due to aggregation did not occur easily because Pt/K8 and Pt/K13 had longer Pt particle distances than that for Pt/K4, also including Pt particles in nanopores. Moreover, the longer distances between Pt particles would decrease the possibility of reprecipitation on the surface of adjacent Pt particles, and thus, the Ostwald ripening would decrease. Since Pt/K13 had longer distances between Pt particles, with suppression of Ostwald ripening, many smaller Pt particles were present, even after the durability test. On the other hand, for Pt/K4, with a shorter Pt interparticle distance than

Pt/K8 and Pt/K13 and due to the large percentage of exterior Pt particles (75%), aggregation resulted. Figure 2-10g,j shows the Pt particle size distributions on the GDL side and membrane side of Pt/K4, respectively. Similarly, Figure 2-10h,k shows the distributions for Pt/K8 and Figure 2-10i,l shows the distributions for Pt/K13. In the Pt particle distributions for Pt/K13, the percentages of small Pt particles were higher than those for Pt/K4 and Pt/K8 on both sides. These results also support the hypothesis that Ostwald ripening and aggregation were suppressed due to the long interparticle distances and presence of nanopores for Pt/K13. The EPMA results of all catalysts (Figure 2-10p−r) show that the Pt contents in these CLs at EOT increased in the order Pt/K4 < Pt/K8 < Pt/K13, and the Pt contents on the membrane side of both Pt/K4 and Pt/K8 were remarkably decreased in comparison with the GDL side. The Pt particles near the membrane can easily dissolve, and the dissolved ions can flow into the membrane and be precipitated by crossover hydrogen, forming a Pt band.[46,47] The closer to the membrane, the less Pt remains in the catalyst layer.[31,48] My results are consistent with the previous research. The amount of Pt present on the membrane side of Pt/K13 was larger than those for the others (Figure 2-10r) and is considered to be one of the factors that could help to maintain the relatively high performance partly because the proton transport resistance was small. Moreover, the more uniform the distribution of Pt in the catalyst layer, the more uniformly the reaction takes place in the catalyst layer. The centralization of the reaction sites, which would adversely impact the oxygen transport pathways, was reduced, leading to the smaller change in diffusion overvoltage for Pt/K13 (Table 2-3). Moreover, the suppression of reaction site centralization on the GDL side of the CL helped to minimize increases in the length of the proton transport pathways. In this study, the effects of the oxygen transport pathways and proton transport pathways could not be separated.

I will be seeking to clarify this in ongoing research. The Pt distributions of the membrane in Figure 2-10m−o show that Pt/K13 had small Pt particles, Pt/K8 had larger particles than Pt/K13 and Pt/K4, and the Pt particles of Pt/K8 CL had undergone more extensive dissolution and reprecipitation than the others. These results indicate that the larger extent of Pt dissolution and reprecipitation in the membrane of Pt/K8 than that for Pt/K13 was an important factor leading to its larger decrease in cell performance. Padgett et al. reported the amount of Pt that migrates into the membrane is generally insensitive to the morphology of the CB support.[10] However, as explained in the Introduction, those results were obtained from a durability test based on voltage cycling under a H_2/N_2 gas atmosphere. Takei et al. found that the amount of Pt that migrates to the membrane differed depending on the catalyst under actual load cycling operation (H_2/air), and they reported that increased amounts of water in the CL increased the amount of Pt depositing on the membrane.[31] These results indicate that a difference in the hydrophilicity of the CL caused the difference in the amount of Pt dissolving into the membrane. I conclude that an appropriate CB support and Pt particle size are important in mitigating dissolution and reprecipitation in the membrane under actual fuel cell operating conditions. On the other hand, since Pt particles having a large particle size are energetically stable, they can be retained without being dissolved.[9] Since Pt/K4 had comparatively larger Pt particles, which were more stable and underwent less dissolution, this catalyst experienced a lesser degree of precipitation in the membrane. In the Pt/K4 catalyst layer, the shapes of the Pt particles differed clearly between the two sides, GDL and membrane, which also suggests that the mechanism of coarsening of the Pt particles differed between the two sides. These results indicate that the dissolution of Pt was added to the mechanisms for the Pt particle coarsening on the membrane side as a factor that decreases the cell performance during

an actual fuel cell operating durability evaluation that includes power generation because the water flux from cathode to anode enhances the movement of Pt ions.[31] From those evaluations of both BOT and EOT, Pt/K13 had higher initial performance and durability than the others and was considered to be the most suitable catalyst in the intermediate current density region under atmospheric pressure. I found that, when the ionomer content was optimized, the high surface area CB support was advantageous for the maintenance of small Pt particle size. I can prevent the blocking of the nanopores and improve the transport of oxygen and protons to Pt in the nanopores and increase the interparticle distance, leading to both increased electrochemical surface area and suppression of Ostwald ripening and coarsening.

2-4. Conclusions

I recognize that there is no general consensus regarding the penetration of ionomer into nanopores. At present, no one has found clear evidence of ionomer intrusion into the nanopores. Previous papers have recommended that Pt particle be selectively supported outside the nanopores for higher current density.[2] However, I aware that Pt/K8 also uses about 10% of Pt in the internal pores.[9] El Hannach et al. reported that the ionomer was distributed in the 5 nm pores of K8; their conclusion was that there was no ionomer intrusion into the micropores, and the ionomer was distributed on the surface of agglomerates. However, since they did not define the size of the internal pores of the CB support in detail in the way I have done in the present work, they were not able to consider conclusively whether the ionomer intruded into the nanopores.[19] On the other hand, Padgett et al. and Yarlagadda et al. proposed the active utilization of Pt in nanopores.[10,11,16] In my study, I suggest that, in the region of intermediate current density, catalysts with

large nanopore capacities such as Pt/K13 can actively utilize Pt in the pores. I also propose that it is beneficial from the point of view of avoiding poisoning because the number of Pt particles that are not in direct contact with ionomer increases.[3–7] I investigated the effect of the CB support on the Pt particle distribution, ionomer distribution, cell performance, and durability (under actual load cycling operation) with various specific surface areas using STEM observation, N_2-adsorption measurement, and electro-chemical characterization. The specific surface area increased in the following order: Pt/V1 < Pt/K4 < Pt/K8 < Pt/K13. The degree of ionomer impregnation in the nanopores of the catalyst was able to be evaluated by the hysteresis volume of the isotherms obtained by N_2-adsorption measurement. Excess ionomer caused a sharp decrease in the hysteresis volume, suggesting the blocking of the nanopore entrances. The ECSA and cell performance were able to be maximized by ensuring that the ionomer did not block the nanopore entrances after activation. I found that, even if the optimal ECSA values were nearly the same for Pt/K8 and Pt/K13, Pt/K13 had better cell performance in the low potential region (intermediate current density region) than Pt/K8 because Pt/K13 had improved proton transport and good oxygen transport. Pt/K13 underwent little deterioration in the actual load operation durability test and showed high cell performance at EOT. I found from the durability evaluation of actual load operation, which involves the flux of both gas and water, that increasing the distance between Pt particles on the catalyst suppresses Ostwald ripening and coarsening of Pt particles, as well as suppressing the reprecipitation of Pt in the membrane. Preventing the ionomer from blocking the nanopores of the catalyst and increasing the Pt interparticle distance is important in order to improve both cell performance and durability and constitutes a

promising means of increasing the effective utilization of the accessible Pt particles on the surfaces of the nanopores in the primary CB particles.

2-5. References

1 Lopez-Haro, M.; Guétaz, L.; Printemps, T.; Morin, A.; Escribano, S.; Jouneau, P.-H.; Bayle-Guillemaud, P.; Chandezon, F.; Gebel, G. Three-dimensional analysis of Nafion layers in fuel cell electrodes. *Nat. Commun.* 2014, 5, 5229.

2 Park, Y.-C.; Tokiwa, H.; Kakinuma, K.; Watanabe, M.; Uchida, M. Effects of carbon supports on Pt distribution, ionomer coverage and cathode performance for polymer electrolyte fuel cells. *J. Power Sources* 2016, 315, 179−191.

3 Shinozaki, K.; Morimoto, Y.; Pivovar, B. S.; Kocha, S. S. Suppression of Oxygen Reduction Reaction Activity on Pt-Based Electrocatalysts from Ionomer Incorporation. *J. Power Sources* 2016, 325, 745−751.

4 Kodama, K.; Shinohara, A.; Hasegawa, N.; Shinozaki, K.; Jinnouchi, R.; Suzuki, T.; Hatanaka, T.; Morimoto, Y. Catalyst Poisoning Property of Sulfonimide Acid Ionomer on Pt (111) Surface. *J. Electrochem. Soc.* 2014, 161, F649−F652.

5 Kodama, K.; Motobayashi, K.; Shinohara, A.; Hasegawa, N.; Kudo, K.; Jinnouchi, R.; Osawa, M.; Morimoto, Y. Effect of the Side-Chain Structure of Perfluoro-Sulfonic Acid Ionomers on the Oxygen Reduction Reaction on the Surface of Pt. *ACS Catal.* 2018, 8, 694− 700.

6 Kongkanand, A.; Yarlagadda, V.; Garrick, T. R.; Moylan, T. E.; Gu, W. (Plenary) Electrochemical Diagnostics and Modeling in Developing the PEMFC Cathode. *ECS Trans.* 2016, 75, 25−34.

7 Kocha, S. S.; Zack, J. W.; Alia, S. M.; Neyerlin, K. C.; Pivovar, B. S. Influence of Ink Composition on the Electrochemical Properties of Pt/C Electrocatalysts. *ECS Trans.* 2013, 50, 1475−1485.

8 Ito, T.; Matsuwaki, U.; Otsuka, Y.; Hatta, M.; Hayakawa, K.; Matsutani, K.; Tada, T.; Jinnai, H. Three-Dimensional Spatial Distributions of Pt Catalyst Nanoparticles on Carbon Substrates in Polymer Electrolyte Fuel Cells. *Electrochemistry* 2011, 79, 374−376.

9 Uchida, M.; Park, Y.-C.; Kakinuma, K.; Yano, H.; Tryk, D. A.; Kamino, T.; Uchida, H.; Watanabe, M. Effect of the state of distribution of supported Pt nanoparticles on effective Pt utilization in polymer electrolyte fuel cells. *Phys. Chem. Chem. Phys.* 2013, 15, 11236−11247.

10 Padgett, E.; Yarlagadda, V.; Holtz, M. E.; Ko, M.; Levin, B. D. A.; Kukreja, R. S.; Ziegelbauer, J. M.; Andrews, R. N.; Ilavsky, J.; Kongkanand, A.; Muller, D. A. Mitigation of PEM Fuel Cell Catalyst Degradation with Porous Carbon Supports. *J. Electrochem. Soc.* 2019, 166, F198−F207.

11 Padgett, E.; Andrejevic, N.; Liu, Z.; Kongkanand, A.; Gu, W.; Moriyama, K.; Jiang, Y.; Kumaraguru, S.; Moylan, T. E.; Kukreja, R.; Muller, D. A. Connecting Fuel Cell Catalyst Nanostructure and Accessibility Using Quantitative Cryo-STEM Tomography. *J. Electrochem. Soc*. 2018, 165, F173−F180.

12 Antolini, E. Carbon supports for low-temperature fuel cell catalysts. *Appl. Catal., B* 2009, 88, 1−24.

13 Watanabe, M.; Tomikawa, M.; Motoo, S. Experimental analysis of the reaction layer structure in gas diffusion electrode. *J. Electroanal. Chem.* 1985, 195, 81−93.

14 Watanabe, M.; Makita, K.; Usami, H.; Motoo, S. New preparation method of a high performance gas diffusion electrode working at 100 % utilization of catalyst clusters and analysis of the reaction layer. *J. Electroanal. Chem.* Interfacial Electrochem. 1986, 197, 195−208.

15 Uchida, M.; Fukuoka, Y.; Sugawara, Y.; Eda, N.; Ohta, A. Effects of microstructure of carbon support in the catalyst layer on the performance of polymer-electrolyte fuel cells. *J. Electrochem. Soc.* 1996, 143, 2245−2252.

16 Yarlagadda, V.; Carpenter, M. K.; Moylan, T. E.; Kukreja, R. S.; Koestner, R.; Gu, W.; Thompson, L.; Kongkanand, A. Boosting Fuel Cell Performance with Accessible Carbon Mesopore. *ACS Energy Lett.* 2018, 3, 618−621.

17 Ramaswamy, N.; Gu, W.; Ziegelbauer, J. M.; Kumaraguru, S. Carbon Support Microstructure Impact on High Current Density Transport Resistances in PEMFC Cathode. *J. Electrochem. Soc.* 2020, 167, 064515.

18 Harzer, G. S.; Orfanidi, A.; El-Sayed, H.; Madkikar, P.; Gasteiger, H. A. Tailoring Catalyst Morphology towards High Performance for Low Pt Loaded PEMFC Cathodes. *J. Electrochem. Soc.* 2018, 165, F770−F779.

19 El Hannach, M.; Soboleva, T.; Malek, K.; Franco, A. A.; Prat, M.; Pauchet, J.; Holdcroft, S. Characterization of pore network structure in catalyst layers of polymer electrolyte fuel cells. *J. Power Sources* 2014, 247, 322−326.

20 Garrick, T. R.; Moylan, T. E.; Yarlagadda, V.; Kongkanand, A. Characterizing Electrolyte and Platinum Interface in PEM Fuel Cells Using CO Displacement. *J. Electrochem. Soc.* 2017, 164, F60−F64.

21 Shimizu, R.; Park, Y. C.; Kakinuma, K.; Iiyama, A.; Uchida, M. Effects of Both Oxygen Permeability and Ion Exchange Capacity for Cathode Ionomers on the

Performance and Durability of Polymer Electrolyte Fuel Cell. *J. Electrochem. Soc.* 2018, 165, F3063−F3071.

22 Kongkanand, A.; Mathias, M. F. The Priority and Challenge of High-Power Performance of Low-Platinum Proton-Exchange Membrane Fuel Cells. *J. Phys. Chem. Lett.* 2016, 7, 1127−1137.

23 Garsany, Y.; Atkinson, R. W.; Sassin, M. B.; Hjelm, R. M. E. Improving PEMFC Performance Using Short-Side-Chain Low Equivalent-Weight PFSA Ionomer in the Cathode Catalyst Layer. *J. Electrochem. Soc.* 2018, 165, F381−F391.

24 Jinnouchi, R.; Kudo, K.; Kodama, K.; Kitano, N.; Suzuki, T.; Minami, S.; Shinozaki, K.; Hasegawa, N.; Shinohara, A. The role of oxygen-permeable ionomer for polymer electrolyte fuel cells. *Nat. Commun.* 2021, 12, 4956.

25 Y, Xiaocong.; Zhang, F.; Zhang, H.; Tang, H.; Pan, M.; Fang, P. Improving Oxygen Reduction Performance by Using Protic Poly (Ionic Liquid) as Proton Conductors. *ACS Appl. Mater. Interfaces* 2019, 11, 6111−6117.

26 Pan, L.; Ott, S.; Dionigi, F.; Strasser, P. Current challenges related to the deployment of shape-controlled Pt alloy oxygen reduction reaction nanocatalysts into low Pt-loaded cathode layers of proton exchange membrane fuel cells. *Curr. Opin. Electrochem.* 2019, 18, 61−71.

27 Uchida, M. PEFC catalyst layers: Effect of support microstructure on both distributions of Pt and ionomer and cell performance and durability. Curr. Opin. Electrochem. 2020, 21, 209− 218.

28 Hiraoka, F.; Matsuzawa, K.; Mitsushima, S. Degradation of Pt/C under various potential cycling patterns. *Electrocatalysis* 2013, 4, 10−16.

29 Kawahara, S.; Mitsushima, S.; Ota, K.; Kamiya, N. Deterioration of Pt catalyst under potential cycling. *ECS Trans.* 2006, 3, 625−631.

30 Wang, X.; Kumar, R.; Myers, D. J. Effect of Voltage on Platinum Dissolution: Relevance to Polymer Electrolyte Fuel Cells. *Electrochem. Solid-State Lett.* 2006, 9, A225−A227.

31 Takei, C.; Kakinuma, K.; Kawashima, K.; Tashiro, K.; Watanabe, M.; Uchida, M. Load cycle durability of a graphitized carbon black-supported platinum catalyst in polymer electrolyte fuel cell cathodes. *J. Power Sources* 2016, 324, 729−737.

32 Uchimura, M.; Sugawara, S.; Suzuki, Y.; Zhang, J.; Kocha, S. S. Electrocatalyst Durability under Simulated Automotive Drive Cycles. *ECS Trans.* 2008, 16, 225−234.

33 Gor, G. Y.; Thommes, M.; Cychosz, K. A.; Neimark, A. V. Quenched solid density functional theory method for characterization of mesoporous carbons by nitrogen adsorption. *Carbon* 2012, 50, 1583−1590.

34 Neimark, A. V.; Lin, Y.; Ravikovitch, P. I.; Thommes, M. Quenched solid density functional theory and pore size analysis of micro-mesoporous carbons. *Carbon* 2009, 47, 1617−1628.

35 Puziy, A. M.; Poddubnaya, O. I.; Gawdzik, B.; Sobiesiak, M. Comparison of heterogeneous pore models QSDFT and 2D-NLDFT and computer programs AsiQwin and SAIEUS for calculation of pore size distribution. *Adsorption* 2016, 22, 459−464.

36 Thommes, M.; Cychosz, K. A. Physical adsorption characterization of nanoporous materials: progress and challenges. *Adsorption* 2014, 20, 233−250.

37 Landers, J.; Gor, G. Y.; Neimark, A. V. Density functional theory methods for characterization of porous materials. *Colloids Surf., A* 2013, 437, 3−32.

38 Soboleva, T.; Zhao, X.; Malek, K.; Xie, Z.; Navessin, T.; Holdcroft, S. On the Micro-, Meso-, and Macroporous Structures of Polymer Electrolyte Membrane Fuel Cell Catalyst Layers. *ACS Appl. Mater. Interfaces* 2010, 2, 375−384.

39 Delaporte, N.; Belanger, R. L.; Lajoie, G.; Trudeau, M.; Zaghib, K. Multi-carbonyl molecules immobilized on high surface area carbon by diazonium chemistry for energy storage applications. *Electrochim. Acta* 2019, 308, 99−114.

40 Sotomayor, F. J.; Cychosz, K. A.; Cychosz, K. A.; Thommes, M. Characterization of Micro/Mesoporous Materials by Physisorption: Concepts and Case Studies. *Acc. Mater. Surf. Res.* 2018, 3, 34−50.

41 Thommes, M.; Kaneko, K.; Neimark, A. V.; Olivier, J. P.; Rodriguez-Reinoso, F.; Rouquerol, J.; Sing, K. S. W. Physisorption of gases, with special reference to the evaluation of surface area and pore size distribution (IUPAC Technical Report). *Pure Appl. Chem.* 2015, 87, 1051−1069.

42 Gambou-Bosca, A.; Ḅ elanger, D. Chemical Mapping and Electrochemical Performance of Manganese Dioxide/Activated Carbon Based Composite Electrode for Asymmetric Electrochemical Capacitor. *J. Electrochem. Soc.* 2015, 162, F5115.

43 Lee, M.; Uchida, M.; Yano, H.; Tryk, D. A.; Uchida, H.; Watanabe, M. New evaluation method for the effectiveness of platinum/carbon electrocatalysts under operating conditions. *Electrochim. Acta* 2010, 55, 8504−8512.

44 Ferreira, P. J.; la O', G. J.; Shao-Horn, Y.; Morgan, D.; Makharia, R.; Kocha, S.; Gasteiger, H. A. Instability of Pt/C Electrocatalysts in Proton Exchange Membrane Fuel Cells: A Mechanistic Investigation. *J. Electrochem. Soc.* 2005, 152, F2256.

45 Uchida, M.; Kakinuma, K.; Iiyama, A. Evaluation of Cell Performance and Durability for Cathode Catalysts (Platinum Supported on Carbon Blacks or Conducting Ceramic Nanoparticles) During Simulated Fuel Cell Vehicle Operation: Start-Up/Shutdown Cycles and Load Cycles. In *Nanostructured Materials for NextGeneration Energy Storage and Conversion Fuel Cells*; Li, F., Bashir, S., Liu, J., Eds.; Springer: Berlin, Heidelberg, 2018; pp 53−113.

46 Papadias, D. D.; Ahluwalia, R. K.; Kariuki, N.; Myers, D.; More, K. L.; Cullen, D. A.; Sneed, B. T.; Neyerlin, K. C.; Mukundan, R.; Borup, R. L. Durability of Pt-Co Alloy Polymer Electrolyte Fuel Cell Cathode Catalysts under Accelerated Stress Tests. *J. Electrochem. Soc.* 2018, 165, F3166−F3177.

47 Zhang, J.; Litteer, B. A.; Gu, W.; Liu, H.; Gasteiger, H. A. Effect of Hydrogen and Oxygen Partial Pressure on Pt Precipitation within the Membrane of PEMFCs. *J. Electrochem. Soc.* 2007, 154, F1006− F1011.

48 Kneer, A.; Jankovic, J.; Susac, D.; Putz, A.; Wagner, N.; Sabharwal, M.; Secanell, M. Correlation of Changes in Electrochemical and Structural Parameters due to Voltage Cycling Induced Degradation in PEM Fuel Cells. *J. Electrochem. Soc.* 2018, 165, F3241−F3250.

Chapter 3 Effect of Pt Distribution of PEFC Cathode Catalyst on Performance and Durability

3-1. Introduction

In order to obtain high performance, it is important to increase the Pt utilization rate by increasing the reaction field called the three-phase interface where protons, O_2 and electrons meet on the Pt surface in the cathode CL and cause an electrochemical reaction.[1] Carbon Blacks (CBs) such as Acetylene black, Vulcan carbon blacks, Ketjenblack, among others, are often used as carbon support materials, and it has been found that the structure and morphology of the carbon support have a great effect on the fuel cell performance and durability.[2–7] I considered that the efficient supply of protons and oxygen is crucial at high current density. Previous research has revealed that Pt particles supported on the carbon support, which are exposed to ionomer, the sulfonic acid groups of the ionomer adsorb on the Pt surface and inhibit the oxygen reduction reaction (ORR) under low humidity and low current density conditions.[8–11] Therefore, in recent years, by using a carbon support with a high specific surface area that has many pores that ionomer cannot penetrate,[12–16] a large amount of Pt is supported inside the pores, and a proton path is formed by the moisture of the humidifying gas and generated water.[17,18] Such catalysts that can prevent poisoning by the ionomer are called accessible carbons and have been reported to show high performance. Other research has reported that low electrode potential reduce the adsorption of sulfonic acid groups on the Pt surface.[19] Harzer et al. report that it is important that Pt particle is also supported on the surface of the support in order to obtain high performance when using porous carbon.[20] Previous research suggests that accessible carbons should have a certain amount of exterior Pt particles and that these

are covered with ionomer, and that Pt in the pores that cannot be covered with ionomer is made effective by the dissociated protons in the generated water. As typical examples of accessible carbons, Ketjenblack, which has a high specific surface area,[18,21–26] and mesoporous carbons are used.[27–32] The pore structure (pore volume, surface area) and pore size distribution of the high specific surface area supports and catalysts have been determined by the N_2-adsorption measurements, and much research has been focused on the effect of pore structure on performance.[4,23,33] Appropriate ionomer design is important, because, if the ionomer blocks the entrances of the pores of the carbon support, the cell performance will deteriorate. Ionomer on the surface of the support has been reported to be observable using low acceleration voltage transmission electron microscopy (TEM)[3,34,35] or scanning transmission electron microscopy (STEM).[36] On the other hand, the low acceleration voltage TEM or the STEM cannot determine the shape of the pores of the carbon support. Therefore, although the ionomer covering the surface of the carbon support can be observed, the state of the ionomer penetrating into the pores cannot be determined. It has been difficult to directly characterize the state of coverage of the ionomer on a porous support, and this deficiency has hampered progress in the field.

In previous research, I suggested that the amount of hysteresis volume in the isotherm of the N_2-adsorption measurements is a parameter that indicates the state of ionomer coverage in the pores of the catalysts.[37] In addition, the effect of Pt loading percentage (wt % Pt) on cell performance was also investigated.[17] Rahman et al. used two supports with different specific surface areas (about 1300 m^2 / g and 800 m^2 / g) to prepare a catalyst in which the wt % Pt was varied from 25 to 40 wt %. They inferred the morphology of catalysts from the Pt particle size and pore volume and discussed the correlation between cell performance and durability. They showed that it is important not

to increase the wt % Pt so much that the Pt particle begins to block the pores.[33] In these studies, different wt % Pt catalysts have not been compared to cell performance with information obtained from detailed analysis of morphology such as Pt interior and exterior frequency, Pt particle size distribution, pore size distribution, and ionomer coverage. As the wt % Pt changes, the interior and exterior distribution of Pt changes, which may affect the state of coverage of the ionomer. In order to design a high-performance catalyst, it is important to investigate not only the Pt particle size and pore volume, but also the more detailed catalyst morphology.

In addition, many studies have investigated Pt or PtCo deterioration and carbon deterioration with catalysts using various types of supports.[38–40] Three factors are considered as catalyst deterioration factors: (1) coarsening of Pt particles by electrochemical Ostwald ripening and aggregation;[41,42] (2) some dissolved Pt precipitates into the polymer electrolyte membrane, producing what is called a Pt band,[43] and a portion of the dissolved Pt is discharged into the wastewater of the cathode;[44] and (3) carbon corrosion occurs in the CL during startup and shutdown, which causes Pt particle detachment from the carbon support. When H_2 and O_2 are present in the anode CL during startup and shutdown and an H_2-front is generated, reversal current causes carbon corrosion.[45–47] The hydrogen passivation process (H_2-SU/SD) has been proposed to improve the durability of PEFCs during startup and shutdown. During shutdown, the cathode O_2 is consumed by the H_2 that permeates through the anode by closing the cathode gas valves at both the inlet and outlet and also stopping the supply of anode gas (H_2). During startup, the valve is reopened, and air and H_2 are resupplied to the cathode and anode, respectively. H_2-SU/SD prevents current reversal from the H_2-front of the anode and suppresses severe carbon corrosion. However, it was found that H_2-SU/SD also

caused carbon corrosion, even though it was less severe than that during the current reversal.[48] Speder et al. investigated the effect of wt % Pt on changes in electrochemical surface area (ECSA) in Ketjenblack and Vulcan through load cycling and startup and shutdown durability tests.[49] They showed that the wt % Pt could affect carbon corrosion and coarsening of Pt particles. Most studies have examined these types of degradation by potential cycling under H_2/N_2 (anode/cathode) gas conditions.[50] In this evaluation, the effect of the potential on the deterioration of Pt and Co and carbon corrosion are observed, so the conditions are such that the generated water and O_2 and H_2 gas flux in actual operation are not taken into consideration. Takei et al. investigated the catalyst deterioration during galvanostatic load cycling operating condition under H_2/Air conditions using a graphitized CB supported platinum catalyst.[51]

In a previous study, carried out under galvanostatic load cycling, I reported that increasing the distance between Pt particles using an ultrahigh specific surface area support can suppress the coarsening of the Pt particles and improve durability.[37] Lowering the wt % Pt on the carbon support is one approach to increase the interparticle distance. On the other hand, as the wt % Pt decreases, the thickness of the CL increases, which increases the gas diffusion resistance and may reduce performance. In addition, I investigated the durability of galvanostatic load cycling operation but did not include startup or shutdown.

Designing a catalyst that achieves both high performance and high durability is an important task in fuel cell technology. In the present study, I sought to propose a design guideline for a high-performance catalyst from the morphology of the catalyst and the cell performance by using ultrahigh specific surface area support catalysts with various wt % Pt values. I also examined the optimum CL structure for high durability by carrying

out durability testing including startup, shutdown and galvanostatic load cycling operation.

3-2. Experimental

3-2-1. Analysis of Pt particle distribution of catalysts

The morphology of the Pt particles was analyzed by scanning transmission electron microscopy (STEM, HD-2700, Hitachi High-Technologies Co.). The Pt particle size and interior or exterior distributions were analyzed based on the images acquired by STEM. Details of the method are described in section 2-2-3.

3-2-2. Catalyst materials and preparation of MEAs

All the anode CLs were prepared with a CB supported PtRu catalyst (Tanaka Kikinzoku Kogyo K.K.) with a total metal loading of 54% by weight. All of the cathode CLs were prepared from Pt particles dispersed on CB (Tanaka Kikinzoku Kogyo K.K.) with four different wt % Pts (20 wt %, 30 wt %, 40 wt % and 50 wt %). The wt % Pt indicates the percentage of the weight of Pt in the total weight of the support and Pt. I will simplify the description of each catalyst as Pt/K18-2, Pt/K18-3, Pt/K18-4, Pt/K18-5. The CB support of these catalysts was ECP600JD (Lion Specialty Chemicals Co., Ltd.) and noted as K18. Anode and cathode CL inks were prepared by dispersing the catalysts in water, ethanol, and Nafion™ PFSA polymer dispersion (D2020, Chemours Company, ion exchange capacity (IEC) = 1.03-1.12 meq g^{-1}). Ethanol, distilled water, and ionomer were added to the catalyst (ethanol/water = 50:50 wt %), mixed, the catalyst inks were directly sprayed onto the ion exchange polymer electrolyte membrane (NR-211, Dupont, 25 μm thickness) using a pulse-swirl-spray (PSS, Nordson Co. Ltd.) apparatus, and the hot plate was set at

65 °C to prepare the catalyst-coated membranes (CCMs). The cathode ink was applied on one side of the polymer electrolyte membrane, and the anode ink was applied on the opposite side. The electrode was 6 cm on each side, with an area of 36 cm^2. The Pt loadings were 0.20 ± 0.01 mg cm^{-2} for the cathode CLs and 0.12 ± 0.01mg cm^{-2} for the anode CLs. The CCMs were annealed by hot-pressing at 140 °C and 1.1 MPa for 5 min, and then they were assembled with two gas diffusion layers (GDLs, H1509, NOK Corp.), one on each electrode.

3-2-3. Physical characterization of CB supports, catalysts and CCMs

Analysis of the surface area and pore size distribution of the CB supports and CCM was carried out using a surface area and pore size analyzer (Autosorb-iQ_3, automated gas sorption analyzer, Anton Paar GmbH). To examine the cathode CL morphology, the CCM was coated with the cathode ink on both sides. Degassing was carried out at the degassing port. Conditions were 200 °C for 8 h on the CB support and catalysts. The CCM was pretreated at low temperature (80 °C) for 24 h to prevent morphological changes of polymer electrolyte membrane and ionomer. The range of P/P_0 values in the N_2-adsorption measurements was 0.025-0.995. Since the amount of N_2 gas dissolved or incorporated into the polymer electrolyte membrane and ionomer was very small, most of the amount of N_2 gas was considered to have been adsorbed on the surface of the carbon support, catalyst or catalyst + ionomer. The specific surface area and pore size distribution were calculated by the Brunauer-Emmett-Teller (BET) method and the quenched solid density functional theory (QSDFT) method, respectively. QSDFT is an analysis method that considers the non-uniform structure of carbon pores.[52] In addition, since the DFT analysis considers the molecular-pore interaction, it is suitable for investigating the

characteristics of pores with diameters down to 10 nm, significantly lower than is available with the Barret, Joyner and Halenda (BJH) method or the Derjaguin-Broekhoff-de Boer (DBdB) method. In this study, N_2 at 77 K on carbon (cylindrical porosity, QSDFT equilibrium model) was selected as the analysis model for the QSDFT method.[3]

3-2-4. MEA characterization by electrochemical measurements

Electrochemical characterization measurements of the cathode CLs were carried out in a single cell evaluation device controlled using a measurement system (Fuel cell single cell evaluation system, Panasonic Production Technology Co., Ltd.). Before starting the measurement, 65 °C H_2 and air were supplied to the anode and cathode, the cell was operated at 0.3 A cm^{-2} for 60 minutes at a cell temperature of 65 °C, then the cathode gas was switched to N_2, and operation was stopped for 60 minutes at a cell temperature of 45 °C. The above operation constituted one cycle, and ten cycles were carried out as a conditioning procedure. Cyclic voltammetry (CV) was carried out at 65 °C and 100% relative humidity (RH) using a potentiostat (HZ3000, Hokuto Denko Co.). The anode was purged with H_2 at a flow rate of 200 mL min^{-1}, the cathode was purged with N_2 at a flow rate of 200 mL min^{-1}, and the gas flow was stopped during measurement. During the CV measurements with the MEA, the hydrogen evolution reaction (HER) starts to occur at voltages lower than about 0.1 V. Since there is an apparent overlapping of the HER current with that of the hydrogen adsorption waves, there is likely to be some error in the $Q_{Pt\text{-}H}$ value. I stopped the N_2 gas flow, because increasing the hydrogen concentration near the cathode catalyst helps to reduce the overlapping of the HER current.[53] Before the potential sweep, the potential was maintained for 30 s at open circuit. Then, the potential was swept back and forth from 0.05 to 1.0 V at 20 mV s^{-1}. The potential sweep was carried out three

times, and the third sweep was used for the calculation of ECSA. The ECSA value was determined from the hydrogen adsorption charge based on $\Delta Q_{\text{Pt-H}}$ = 0.21 mC cm^{-2} with 0.4 V−0.05 V as the hydrogen adsorption region. $\Delta Q_{\text{Pt-H}}$ is the amount of electric charge generated when hydrogen is adsorbed at unity coverage on a polycrystalline Pt surface. C_{dl} is averaging between 0.38 and 0.42 V.

The current−potential polarization ($I-V$) characteristic of MEAs were carried out in a single-cell evaluation device by supplying hydrogen (anode) and air (cathode), at 65 °C and 100% RH under ambient pressure. The flow rates of all gases were controlled using mass flow controllers; the utilizations of the reactant gases were 40% O_2 (U_{o} = 40) and 80% H_2 (U_{f} = 80). The $I-V$ curve was measured at each point with a measurement time of 5 minutes under quasi-static operating conditions, and the average value observed during the final minute was obtained. The overall overvoltage was divided approximately into a reaction overvoltage and a diffusion overvoltage in the following fashion. An approximate Tafel line was obtained from the intercept and slope at a low current of 0.9 V or higher on the IR-free $I-V$ curve, and the reaction overvoltage was determined as the difference from the theoretical open circuit voltage (OCV). The diffusion overvoltage was the difference between the approximate Tafel line and the IR-free voltage. Limiting current measurements were carried out by linearly sweeping the voltage from 0.80 to 0.15 V at a scan rate of 10 mVs^{-1}, 100% RH, and ambient pressure. Diluted oxygen (0.5%) gas (balance 99.5% N_2 or He) was supplied to the cathode (500 mL min^{-1}) and H_2 was supplied to the anode (200 mL min^{-1}), both fully humidified. Limiting current was measured at cell temperatures of 50 °C and 65 °C. The size of the electrodes was 4.84 cm^2 with 2.2 cm on each side. Limiting current measurements were carried out to separate the transport resistance of oxygen. The oxygen transport resistance (R_{total}) has been

investigated in various models.[54,55] Kudo et al. reported that oxygen diffusion resistance at the ionomer/Pt interface has a great effect on performance.[56] In this study, the measurement and analysis of the limiting current were carried out based on the oxygen diffusion resistance model and measurement method presented by Nonoyama et al., in which the oxygen concentration linearly decreases from the GDL to the Pt interface.[57,58] A temperature distribution is assumed between the GDL and the Pt surface, but it has not been measured in this study. Therefore, the temperature distribution is not taken into consideration. This study is based on the assumption that R_{DM}, R_{pore}, and R_{film} occur under the same temperature conditions. Kudo et al. stated that the ionomer/Pt interfacial resistance is important, but in this study, the interfacial resistance and the internal resistance could not be separated, so R_{film} included both. Although I make assumptions in this study, I propose that the relative results obtained in comparing each catalyst do not change, and, to a first approximation, the same tendencies should be observed under a range of conditions.

R_{total} is the sum of the three resistances shown in equation (1):

$$R_{\mathrm{total}} = R_{\mathrm{DM}} + R_{\mathrm{pore}} + R_{\mathrm{film}} \quad (1)$$

R_{DM} is the resistance assigned to oxygen diffusion within the GDL and MPL, R_{pore} is the oxygen diffusion resistance assigned to transport through the CL, and R_{film} is the resistance assigned to the dissolution and diffusion of oxygen in ionomer or water on the surface of Pt.

R_{total} of the cathode can be calculated from the limiting current using the following equation (2).

$$R_{\mathrm{total}} = \mathrm{C_{O2}} \times \frac{4\mathrm{F}}{I_{\mathrm{lim.}}} \quad (2)$$

In the above equation, C_{O2} is the oxygen concentration in the gas channel, F is the Faraday constant, and $I_{lim.}$ is the limiting current. Each resistance can be calculated from the sensitivity of the gas or temperature. Sensitivity indicates the rate of increase in oxygen transport resistance when the conditions are changed. Since the pores of the GDL are large enough (> 0.8 μm),[57] molecular diffusion is dominant and the contribution of Knudsen diffusion can be ignored. In the CL, where most of the pores have a diameter of less than 100 nm,[59] Knudsen diffusion is considered to dominate. R_{DM} and R_{pore} may contain some Knudsen and molecular diffusion, respectively, but this analysis does not appear to have a significant impact on the results. Equation (3) shows the formula for calculating the sensitivity toward the balance gas.

$$Balance\ gas\ sensitivity\ = \frac{\left(v_A^{1/3} + v_B^{1/3}\right)^2}{\sqrt{(1/M_A) + (1/M_B)}} \tag{3}$$

In equation (3), ν_A and ν_B are the diffusion volumes of each mixed gas, and M_A and M_B are the molecular weights of each gas. In this case, the cases of O_2 and N_2 and the cases of O_2 and He were calculated to obtain the sensitivity. When the gas type is changed, only molecular diffusion changes. Since the sensitivity of molecular diffusion resistance between He and N_2 molecules is 3.46, R_{DM} can be obtained from the difference in transport resistance when He and N_2 are used as diluents. The sensitivity when the operating temperature was changed was calculated by applying each temperature to $T^{-1.75}$ for R_{DM}, $T^{-0.5}$ for R_{pore} and $T^{-1}e^{-17200/RT}$ for R_{film}. The sensitivity at 50 °C and 65 °C was 1.08 for R_{DM}, 1.02 for R_{pore} and 1.40 for R_{film}.

3-2-5. Durability evaluations in combined operation cycle of startup, shutdown and galvanostatic load cycling

The durability test was carried out in a combined cycle including startup, shutdown, and galvanostatic load cycling under H_2/air (anode/cathode) conditions, as a protocol that simplifies and simulates the operating mode of the residential fuel cell system. Figure 3-1 shows the protocol of the durability test. The durability test was carried out at a cell temperature of 65 °C and 100% RH and operated at $U_o = 40$ and $U_f = 80$ as in the MEA characterization. First, when gas was supplied to the anode and cathode (startup), the

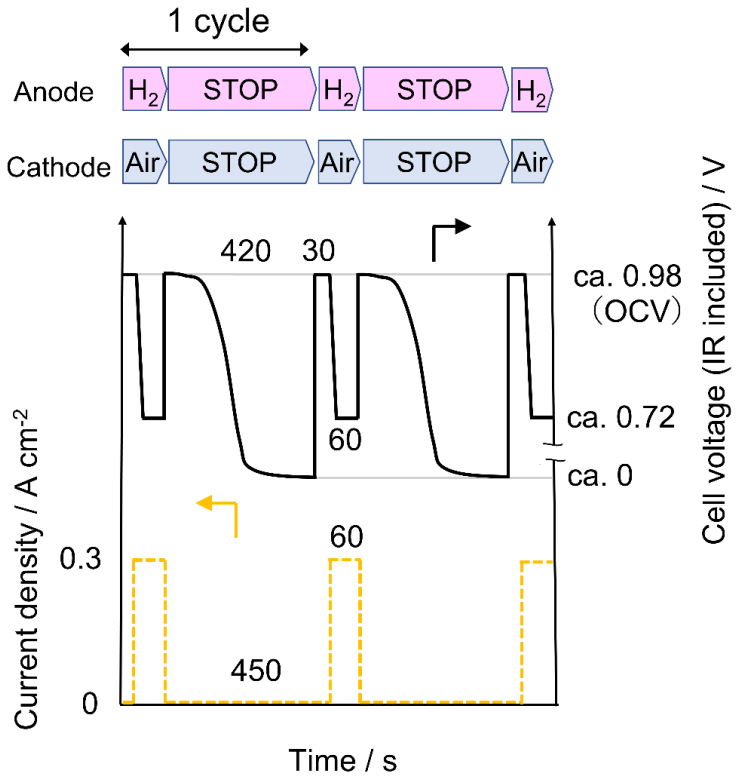

Figure 3-1. Changes in current density and cell voltage for combined cycle protocols, including startup, shutdown, and galvanostatic load cycling, to investigate catalyst degradation.

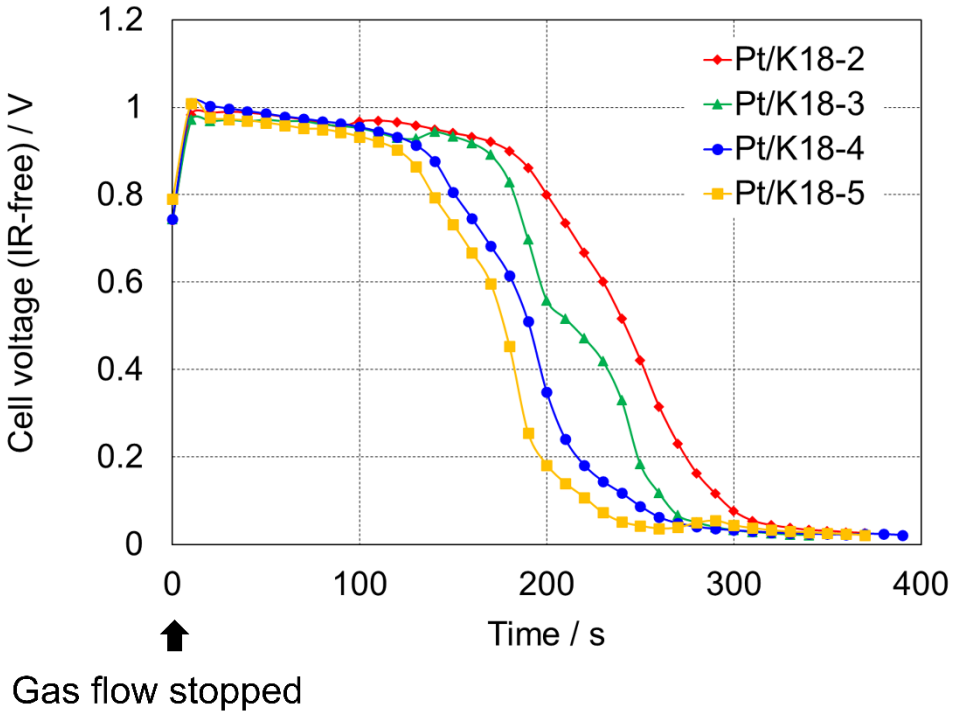

Figure 3-2. Time dependence of voltage of each catalyst after stopping the flow of gas to the anode and cathode during shutdown.

Table 3-1. Time to reach 0.2 V from when the voltage started to drop sharply (100 s).

Catalyst	Pt/K18-2	Pt/K18-3	Pt/K18-4	Pt/K18-5
Voltage drop time / s	98	117	149	175

potential represents the OCV. The cell was held for 30 s at OCV (no current flow) to allow sufficient gas to disperse within the cell, a load operation was held at 0.3 A cm^{-2} for 60 s (simulating an actual load). Then, the gas supply of the anode and the cathode was stopped (shutdown). At this time, H_2 existing at the anode permeates the cathode and reacts with O_2 at the cathode to be consumed, the cell voltage begins to drop and finally drops to near 0 V (Figure 3-2). The lower the wt %, the longer it took for the cell voltage to reach 0.2 V after it began to drop (Table 3-1). This is suggested to be because the lower the wt %

Pt, the thicker the CL, and the longer it takes for H_2 permeating from the anode to react with O_2 in the cathode CL. The operation of the startup, shutdown and galvanostatic load was set as one cycle, and the number of cycles was 2,000. Before and after the durability test, the CV were measured to investigate the degree of ECSA deterioration.

3-2-6. Analysis of catalyst morphology after the durability test

After the durability test, an MEA cross-section sample was prepared using a focused ion beam device (FIB, Hitachi High-Tech Co.). To analyze the distribution of Pt in the depth direction of the polymer electrolyte membrane, Z-contrast (ZC) images of the prepared samples were acquired using STEM. For catalyst observation after the durability test, the polymer electrolyte membrane side of the CL was sampled and transmitted electron (TE) images were acquired by STEM. Concentration changes of Pt in the cathode CL and polymer electrolyte membrane of the MEAs were analyzed using a field emission-electron probe microanalyzer (EPMA) with a Pt line scan.

3-3. Results and discussion

3-3-1. Analysis of CB support, catalyst, CL microstructure and Pt and ionomer distribution of the catalyst

I investigated four catalysts with different loading percentages on the same CB support (K18). In order to focus on the pores of the CB support and catalyst, I defined pores of 10 nm or less as nanopores. The properties of specific surface area and nanopore volume of the K18 and catalysts in this study are summarized in Table 3-2. As the wt % Pt increased, the specific surface area and nanopore volume tended to decrease. Figure 3-3a shows the isotherm of K18 and each catalyst. The hysteresis volume was defined as the

Table 3-2. Properties of the support and catalysts with different Pt loading

	Unit	K18	Pt / K18-2	Pt / K18-3	Pt / K18-4	Pt / K18-5
Actual Pt loading weight percentage	wt%	0	18.3	27.1	34.8	44.3
Specific surface area	$m^2 / g_{\text{-carbon}}^{-1}$	1823	1493	1279	1301	1269
Nanopore volume (~10 nm)	$cm^3 / g_{\text{-carbon}}^{-1}$	1.31	1.06	0.91	0.93	0.86
Hysteresis volume	$cm^3 / g_{\text{-carbon}}^{-1}$	138	136	134	129	121

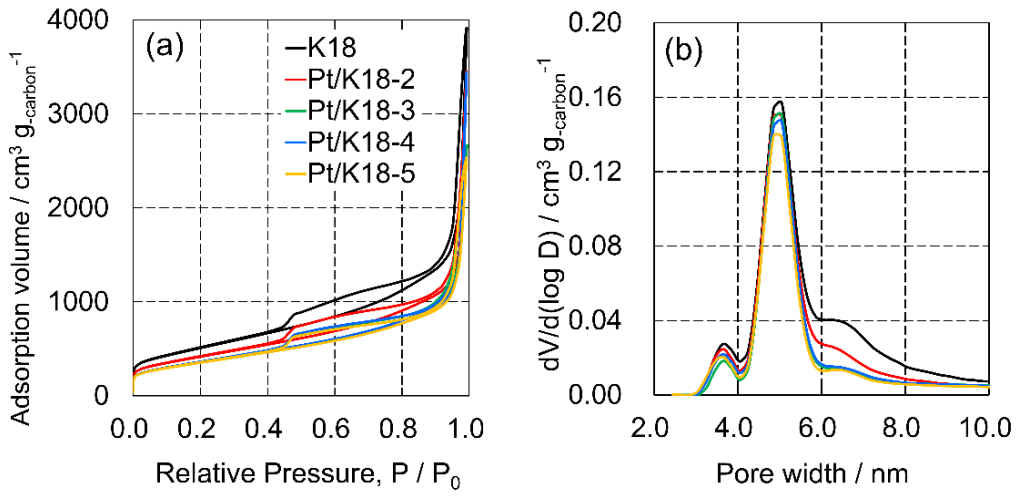

Figure 3-3. The CB support and catalysts (a) isotherm and (b) pore size distribution per unit mass of carbon.

difference between the volume of the isotherm on the desorption side and the adsorption side when $P/P_0 = 0.5$. All samples show IV(a) type characteristics in the isotherm classification,[60] indicating an abundance of nanopores with a diameter of approximately 4 nm.[61] The isotherms showed a combined hysteresis loop of H3 and H4 types,[21] which indicates that K18 and catalysts have bottleneck-shaped pores. From the above characteristics of the isotherms, I conclude that the support and catalysts have many bottleneck-shaped nanopores. The larger the wt % Pt, the smaller the hysteresis volume, indicating that the Pt particles are supported in the pores of the K18. Figure 3-3b shows

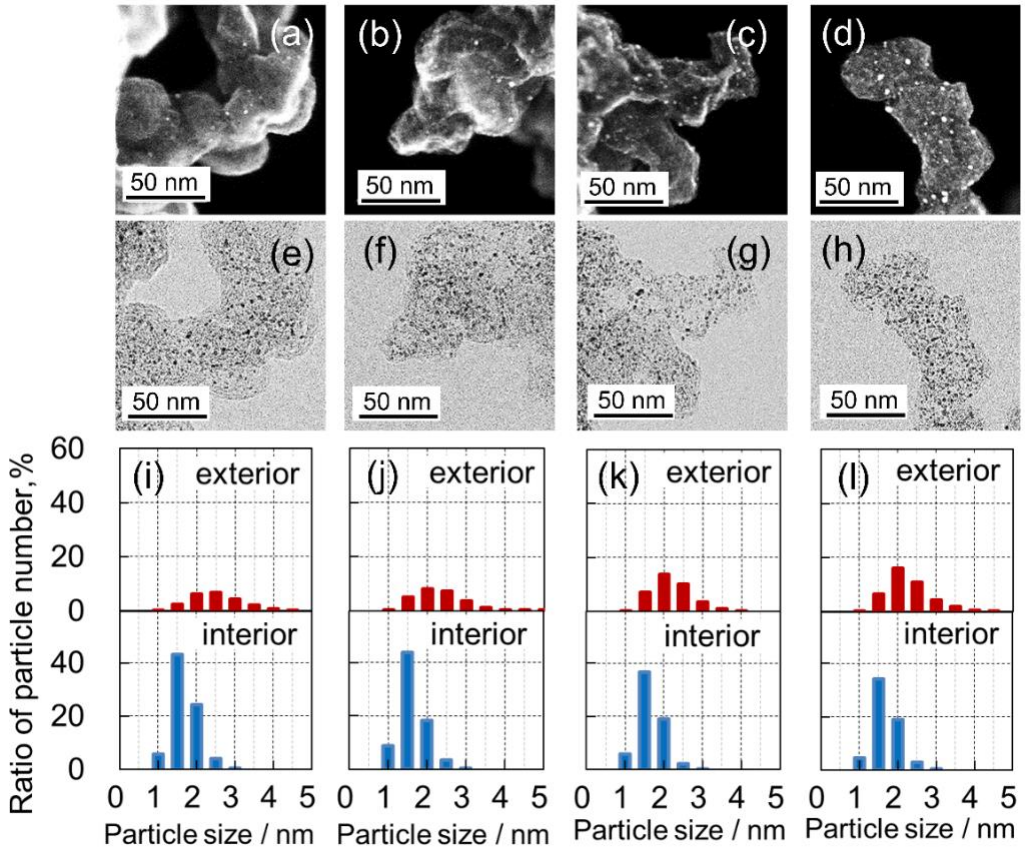

Figure 3-4. STEM images and Pt particle size distributions of the catalysts. SE and TE image of (a,e) Pt/K18-2, (b,f) Pt/K18-3, (c,g) Pt/K18-4, (d,h) Pt/K18-5. Interior and exterior Pt distribution of (i) Pt/K18-2, (j) Pt/K18-3, (k) Pt/K18-4, (l) Pt/K18-5.

the pore size distributions of K18 and catalysts. The decrease in nanopores was small in Pt/K18-2, and gradually decreased from Pt/K18-3 to Pt/K18-5. The secondary electron (SE) and TE images of each catalyst observed by STEM are shown in Figure 3-4a-h. By acquiring an image in which the catalyst is rotated 180°, the interior and exterior Pt can be separated, and very useful information can be obtained to understand the structure of the catalyst. Pt did not appear to be significantly aggregated, even when the wt % Pt was high, but was highly dispersed with small particles. Figure 3-4i–l shows the frequencies of Pt particles present on the interior and exterior surfaces. The exterior Pt particle was

Table 3-3. Interior and exterior Pt particle size and frequency of catalysts.

		Pt/K18-2	Pt/K18-3	Pt/K18-4	Pt/K18-5
Exterior	Frequency, %	22.8%	25.3%	36.4%	39.7%
	Particle size / nm	2.74 ± 0.61	2.54 ± 0.57	2.49 ± 0.51	2.50 ± 0.51
Interior	Frequency, %	77.2%	74.7%	63.6%	60.3%
	Particle size / nm	1.91 ± 0.33	1.86 ± 0.35	1.89 ± 0.32	1.93 ± 0.31

often 2.0 to 2.5 nm, and the interior Pt particle was mostly 1.5 to 2.0 nm. The respective particle sizes did not change significantly for all of the catalysts. The average particle size was about the same for all catalysts, and the higher the wt % Pt, the higher the frequency of exterior Pt (Table 3-3). From these results, it is considered that the Pt particles were not aggregated. Furthermore, since the particle size of Pt was smaller than the diameter of the pores of support analyzed in Figure 3-3b. Park et al. investigated the effect of Pt loading and ionomer addition on pore volume using various carbon supports.[3] Results using Ketjenblack (ECP, about 800 m^2 g^{-1}) as the support showed that the pores of the support were blocked when the exterior Pt particles were above 2.8 nm, resulting in a 45% reduction in support pore volume. The pore size of ECP600JD used as a support in this study has a larger diameter than ECP, and as shown in Table 3-3, the Pt particle size of the catalyst is smaller. Therefore, I considered that Pt rarely blocks the pore entrances. In addition, as shown in Table 3-3, the smaller the wt % Pt, the higher interior Pt frequency. In a study in which Pt was supported on carbon supports having various specific surface areas (pore volumes) using the colloid method, the specific surface area of Pt increased as the specific surface area of the carbon support increased.[62] From this, as the Pt loading percentage increases, the Pt particles are probably initially supported inside the pores and gradually outside the pores. Figure 3-5a shows the isotherms of CCM prepared using each

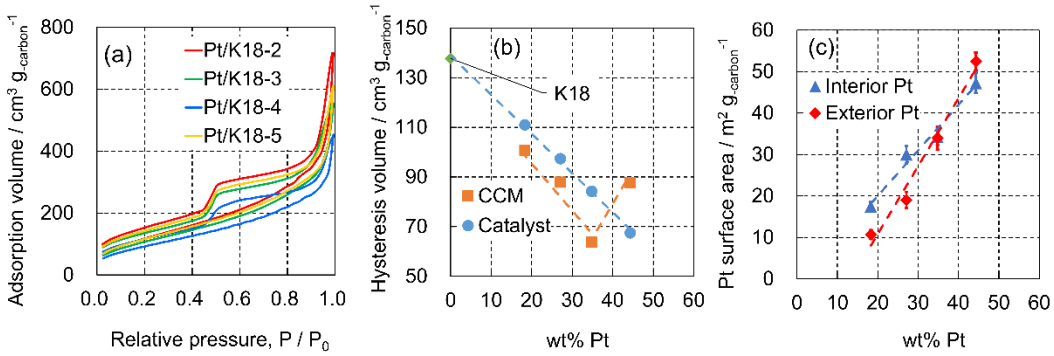

Figure 3-5. (a) CCM isotherm at I/C 1.2 of each catalyst. (b) Hysteresis volume of each catalyst and CCM. (c) Interior and exterior Pt surface area calculated from the particle size of each catalyst.

catalyst at I/C 1.2 and the hysteresis volume of each isotherm are shown in Figure 3-5b. I/C represents the ratio of ionomer weight to carbon weight, and, in the case of catalysts with the same wt % Pt, the larger the I/C value, the larger the amount of ionomer. Ketjenblack (ECP, about 800 m^2 g^{-1}), which has been used as a carbon support for standard catalysts, has many pores with a diameter of approximately 3.5 nm.[37] The ECP600JD used in this study as a carbon support has many pores with a diameter of 5 to 7 nm (Figure 3-3b), which are larger than those of the standard catalyst. Therefore, it is considered that the catalyst using K18 as a carbon support has a structure in which ionomer can easily penetrate near the pore entrance than the standard catalyst. Ngo et al. reported that the alcohol content of alcohol/water mixed solvents has a significant effect on the shape of the ionomer.[63] Although they used isopropanol, I consider that the ionomer behaves similarly in my ink because isopropanol and ethanol have the same number of hydrating water molecules, i.e., three.[64] At the composition ethanol/water = 50:50 wt % in this study, the ionomer is considered to exist as rigid rod-like particles in the solution and during coating on the catalyst, without forming large aggregates. As shown above, the ECP600JD has a larger pore diameter than the ECP, and the ionomer has a rod-like

structure. Therefore, in this study, ionomer may penetrate into the nanopores and cover the interior Pt. Studies have shown that the ionomer does not penetrate into the pores of the catalyst.[13,31,65,66] On the other hand, previous study showed that at least 10% of the interior Pt was covered with ionomer in the catalyst using ECP.[12] Therefore, in my catalyst layer, I believe that ionomer has penetrated into the nanopores to some extent. Inferring from the internal and external distribution of Pt obtained from the STEM observation images shown below and the ECSA shown in section 3-2, 10 to 40% of the interior Pt is covered by ionomer.

CCM hysteresis decreased linearly from Pt/K18-2 to Pt/K18-4 but increased for Pt/K18-5. The results show that ionomer penetrated the pores and covered the interior Pt up to the 40 wt % Pt, but it is considered that the ionomer penetrating the pores decreased when the wt % Pt was increased to 50 wt %. This suggests that the ionomer did not penetrate into the pores in proportion to the wt % Pt. At 50 wt % Pt, the hysteresis volume of CCM is larger than that of the catalyst, which means that the volume of nanopores has increased. The result is unclear, but it is possible that ionomer that could not penetrate the pores bound to the catalytic aggregates to form a new pore structure (bottleneck-like pores with narrow inlets). I am working to elucidate the relationship between the catalyst structure and cell performance by conducting structural analysis from the results of isotherm and pore size distribution using N_2 gas adsorption by various catalysts and CCMs.[3,37,62] I believe that research from this perspective is extremely important in establishing design guidelines for catalyst layer structures and that further research is needed in the future. I have not obtained multiple data points for the measurement in Figure 3-5b. However, in order to obtain reliable data, the recommended optimum pressure tolerance (10^{-3} to 10^{-2}) and recommended equilibrium time (2 to 3 minutes) were set at each measurement point

of the corresponding mesopore volume in N_2 adsorption. I have confirmed that the actual measurement was performed with a sufficient equilibrium time (6 to 10 minutes), longer than the set time, and thus I believe that highly reliable data was obtained. Figure 3-5c shows the Pt surface area of the interior and exterior at each wt % Pt. The surface area was calculated from the particle size measurement results shown in Table 3-3, assuming that the Pt particles are spherical. The interior Pt surface area was larger than the exterior Pt surface area up to the 40 wt % Pt, and the hysteresis volume of CCM was reduced. At 50 wt % Pt, the exterior Pt surface area became larger than the interior Pt surface area, and the hysteresis volume increased. The increase in hysteresis volume (increase in nanopore volume) was caused by the ionomer not penetrating into the catalytic pores. Alternatively, new pores may have been created by binding catalyst aggregates. In any case, this suggests that the penetration of ionomer into the pores and the structure of catalyst layer was affected by the Pt surface areas corresponding to interior and exterior surfaces, which is a very interesting result.

3-3-2. Cell performance and electrochemical measurement

Figure 3-6 shows the dependence of the performance for each catalyst on the I/C value. I/C was optimized based on ECSA (Figure 3-6a), mass activity (Figure 3-6d) and cell voltage at 0.2 A cm^{-2} (Figure 3-6e) for all catalysts. Since the residential fuel cell operates at a low current density in order to achieve high efficiency, I confirmed the optimization of I/C in the low current density region. The performance of I/C 1.2 was the highest for all catalysts, and there was no change in the optimum I/C due to the difference in the wt % Pt. The I/C 1.2 of Pt/K18-4 showed high values in all cases. The changes for Pt/K18-5 were small over the range of I/C was varied. As discussed in section 3-3-1, the values of

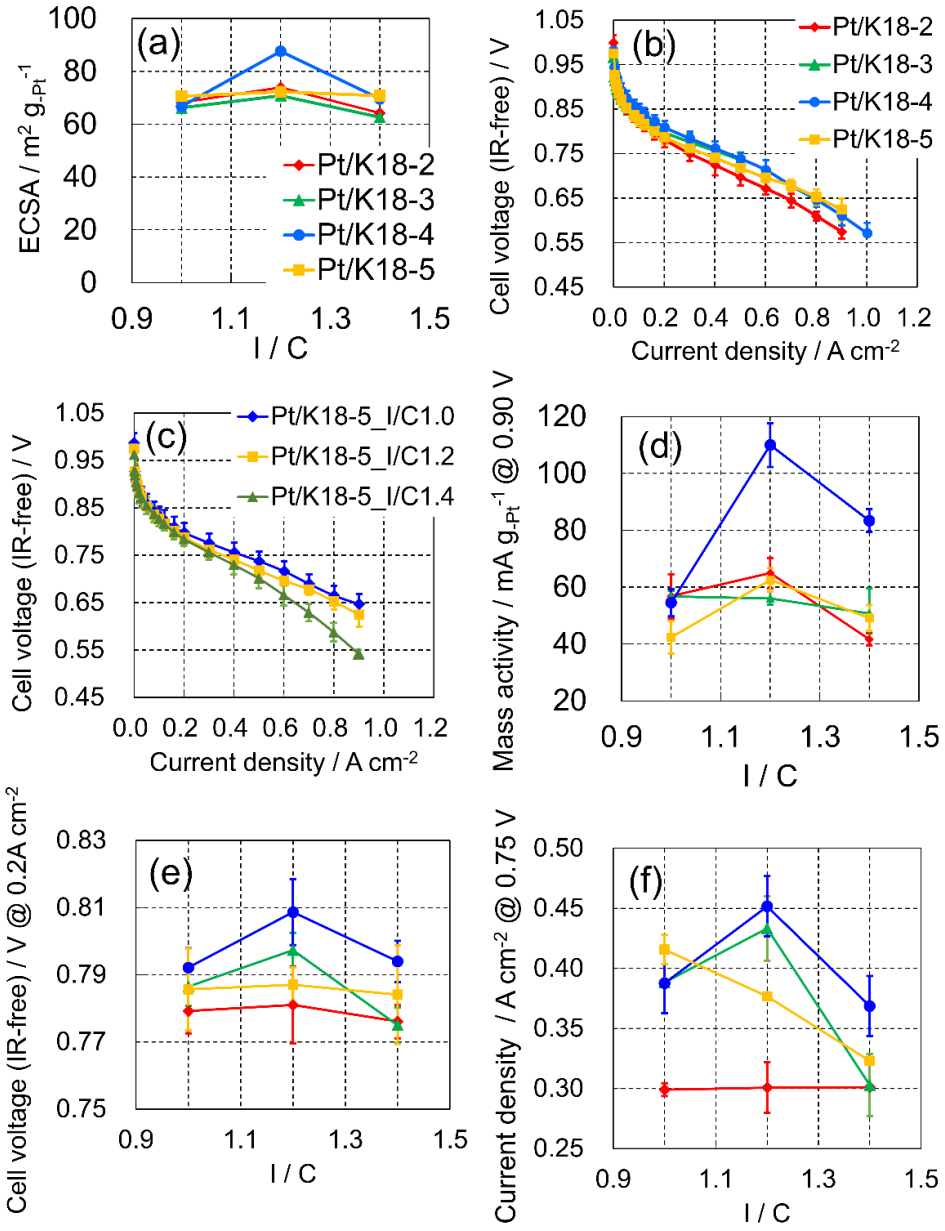

Figure 3-6. Dependence of each catalyst on ionomer content at 65 °C and 100% RH. (a) ECSA, (b) *I*−*V* curve at I/C 1.2, (c) *I*−*V* curve at different I/C of Pt/K18-5, (d) mass activity at 0.90 V, (e) IR-free cell voltage at 0.2 A cm^{-2}, and (f) current density at 0.75 V.

Pt/K18-4 were high in ECSA, mass activity, and cell voltage in the low current density region (0.2 A cm^{-2}), because the ionomer penetrates deep into the pores and covers the Pt particles. Since Pt/K18-5 has a small amount of ionomer penetrating inside the pores, the

Pt supported in the pores is less covered with the ionomer, and the ECSA is small. For Pt/K18-5, it is considered that there is no significant change in the area of Pt covered by ionomer between I/C 1.0 and 1.4. Figure 3-6b shows the $I-V$ curves of each catalyst of I/C 1.2. Pt/K18-2 showed low cell performance in the entire current density region. In addition, the cell performance of Pt/K18-4 was high up to 0.5 A cm^{-2}. Figure 3-6c compares the $I-V$ curves of Pt/K18-5 with different I/C values. As shown in Figure 3-5 e, the cell performance at 0.2 A cm^{-2} was highest at I/C 1.2, but there was no significant difference between I/C 1.0 and 1.4. However, the higher the current density, the higher the cell performance of I/C 1.0, which had the smallest amount of ionomer. In the high current density region, the cell performance of I/C 1.4 was significantly reduced. There was no significant difference in ECSA and mass activity between Pt/K18-2 and Pt/K18-3 or Pt/K18-5. Since Pt/K18-2 has a low Pt density and the thickest CL, the diffusion distance of O_2 is long and the diffusion resistance is large. Therefore, it is considered that the cell performance of Pt/K18-2 is low at a high current density, for which the diffusivity of the gas greatly affects the performance. Pt/K18-4 had high ECSA, MA and thin CL, so it is considered that the cell performance was high. On the other hand, Pt/K18-5 had a high Pt density and a thin CL, so that the diffusion resistance is considered to be low. However, the cell performance was lower than that of Pt/K18-4. The Pt/K18-5 catalyst may be affected by ionomer that could not penetrate the pores, resulting in reduced performance. The higher the current density of Pt/K18-5, the higher the performance of the CL with smaller I/C. Therefore, it is considered that the ionomer was swollen by the generated water and the oxygen diffusivity was hindered. Figure 5f compares the current densities at 0.75 V. The performance of Pt/K18-4 was remarkably high in ECSA and mass

Table 3-4. Comparison of reaction overvoltage and diffusion overvoltage with different current densities when each catalyst is I/C 1.2.

	Current density	Pt/K18-2	Pt/K18-3	Pt/K18-4	Pt/K18-5
Reaction overvoltage	0.01 / A cm^{-2}	300	304	285	301
	0.50 / A cm^{-2}	384	383	382	383
Diffusion overvoltage	0.01 / A cm^{-2}	-	-	-	-
	0.50 / A cm^{-2}	75.9	32.0	27.3	57.0

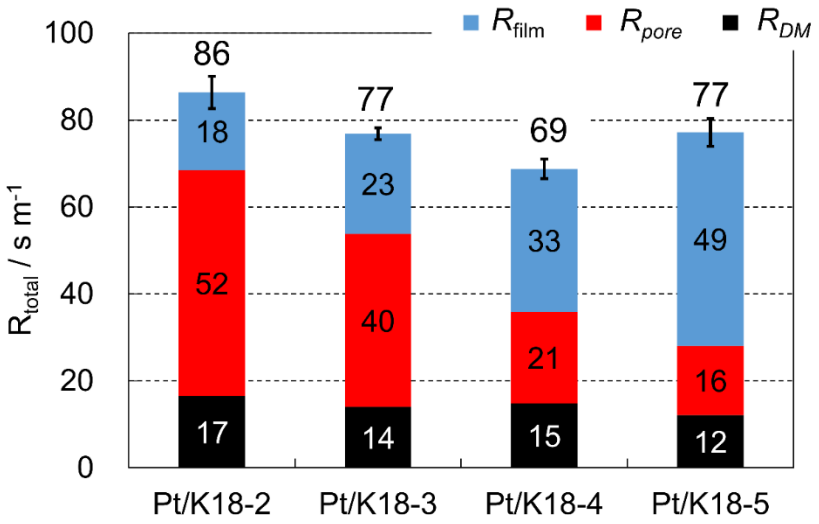

Figure 3-7. Changes in transport resistance measured by limiting current in each catalyst layer.

activity, which are less affected by the generated water, but the cell performance of Pt/K18-3 improved as the current density increased.

Table 3-4 shows the comparison of reaction overvoltage and diffusion overvoltage with different current densities in order to identify the cause of the cell performance degradation at I/C 1.2. The reaction overvoltage was smaller for Pt/K18-4 at 0.01 A cm^{-2}; this agrees with the result in Figure 3-6a, and, since Pt/K18-4 has a high ECSA, the reaction overvoltage was small at very low current densities with little generated water. The reaction overvoltage was equivalent for all catalysts at 0.5 A cm^{-2}. Proton paths of Pt

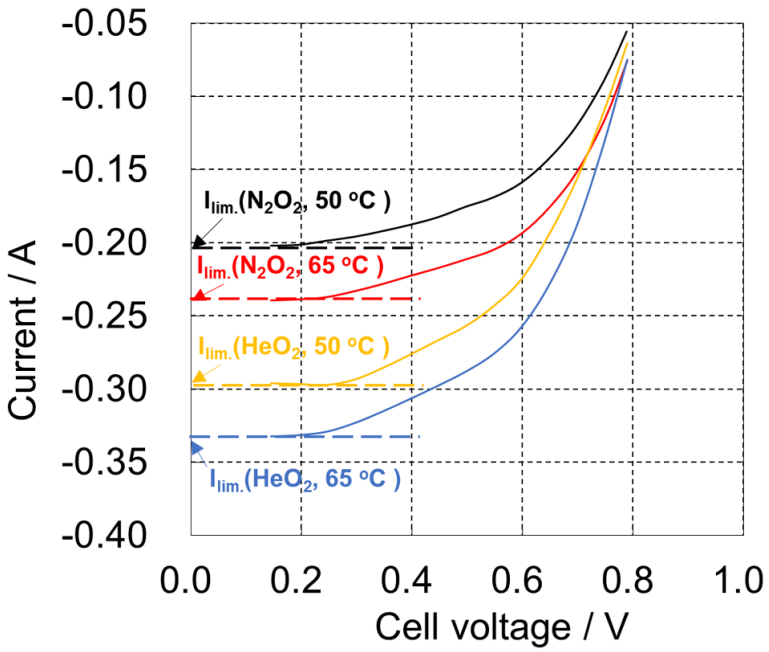

Figure 3-8. An example of linear sweep curve for Pt/K18-5 obtained by limiting current measurement at cell temperatures of 65 °C and 50 °C using oxygen gas diluted 0.5% with N_2 or He.

supported in the pores were formed by the generated water, and, as a result, it is considered that the reaction overvoltage became equivalent. Regarding diffusion overvoltage, it is generally considered that the larger the loading percentage of the catalyst, the thinner the CL and therefore the smaller the diffusion overvoltage. From Pt/K18-2 to Pt/K18-4, as expected, the diffusion overvoltage decreased as the loading percentage increased. However, Pt/K18-5 had a large diffusion overvoltage, which is a factor of low performance. The diffusion resistance is composed of three factors.[57,58] Oxygen diffuses in (1) the carbon paper GDL containing a mesoporous layer (MPL) (R_{DM}), (2) the CL which has small pores (R_{pore}), and (3) the ionomer covering the Pt surface (R_{film}). Figure 3-7 shows the oxygen diffusion resistance of each catalyst measured by the limiting current measurement. The linear sweep curves obtained under each condition are shown in Figure 3-8. Since GDL is the same for all MEAs, R_{DM} was nearly the constant. R_{pore}

tends to become smaller as the wt % Pt increases, which is considered to be due to the thinner CL. On the other hand, the higher the wt % Pt, the higher the R_{film}. As shown in Figure 3-5b, from Pt/K18-2 to Pt/K18-4, the larger the wt % Pt, the more ionomer penetrated into the pores, and the Pt particles supported inside the pores was also covered with ionomer. It is considered that the R_{film} increased, because the oxygen transport resistance for Pt supported in the interior of the pores was increased. Pt/K18-5 is considered to have less ionomer covering the Pt particle inside the pores. Therefore, it is considered that the reason why the R_{film} for Pt/K18-5 was greatly increased is that the Pt particle supported on the exterior surface is thickly covered with ionomer. As discussed in section 3-3-1, the degree of penetration of ionomer into the pores may depend on the Pt surface area, and Pt/K18-5 has a structure in which diffusion resistance is significantly increased by swelling of ionomer by generated water.

I considered that the exterior Pt particle of Pt/K18-5 was thickly covered with ionomer. Figure 3-9 shows schematic images of the catalyst that can be considered from the above. Figure 3-9a corresponds to Pt/K18-2 to Pt/K18-4, and Figure 3-9b to Pt/K18-5. For all

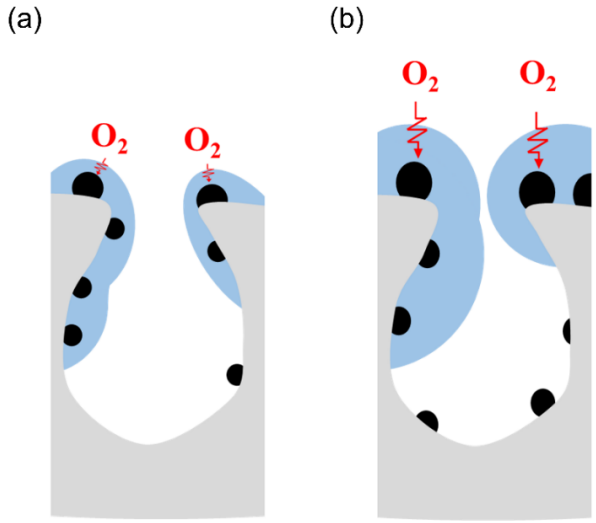

Figure 3-9. Schematic images of ionomer covering near catalyst pores. (a) Pt/K18-2, Pt/K18-3 and Pt/K18-4 (b) Pt/K18-5.

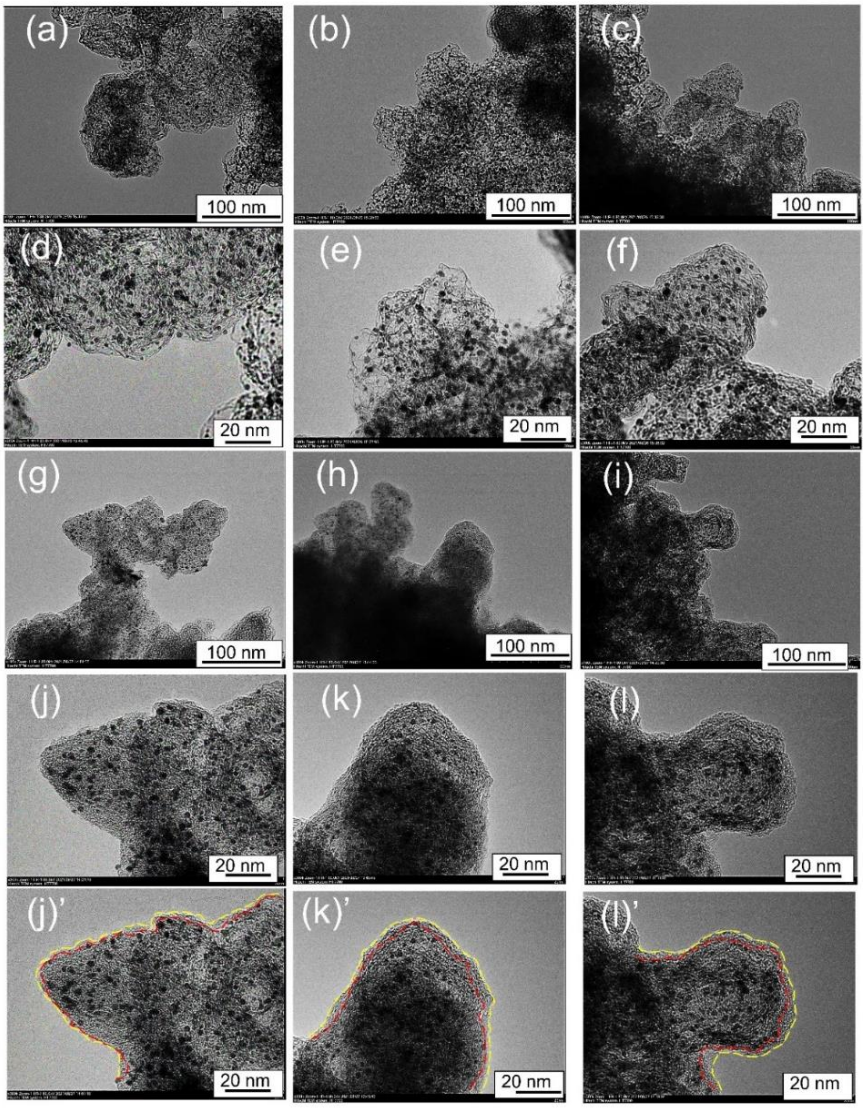

Figure 3-10. Observation image of Pt/K18-4 and Pt/K18-4 with ionomer using low acceleration TEM. (a), (b) and (c) low magnification Pt/K18-4, (d), (e) and (f) high magnification Pt/K18-4, (g), (h) and (i) low magnification Pt/K18-4 with ionomer, (j), (k) and (l) high magnification Pt/K18-4 with ionomer. The ionomer surface (yellow dotted line) and carbon support surface (red dotted line) of (j), (k) and (l) are shown in (j'), (k') and (l').

catalysts, the Pt particles were highly dispersed, without agglomeration. From Pt/K18-2 to Pt/K18-4, the surface area assigned to Pt particle in the interior was large, and the ionomer penetrated the pores. The longer the distance that O_2 must diffuse to reach the Pt

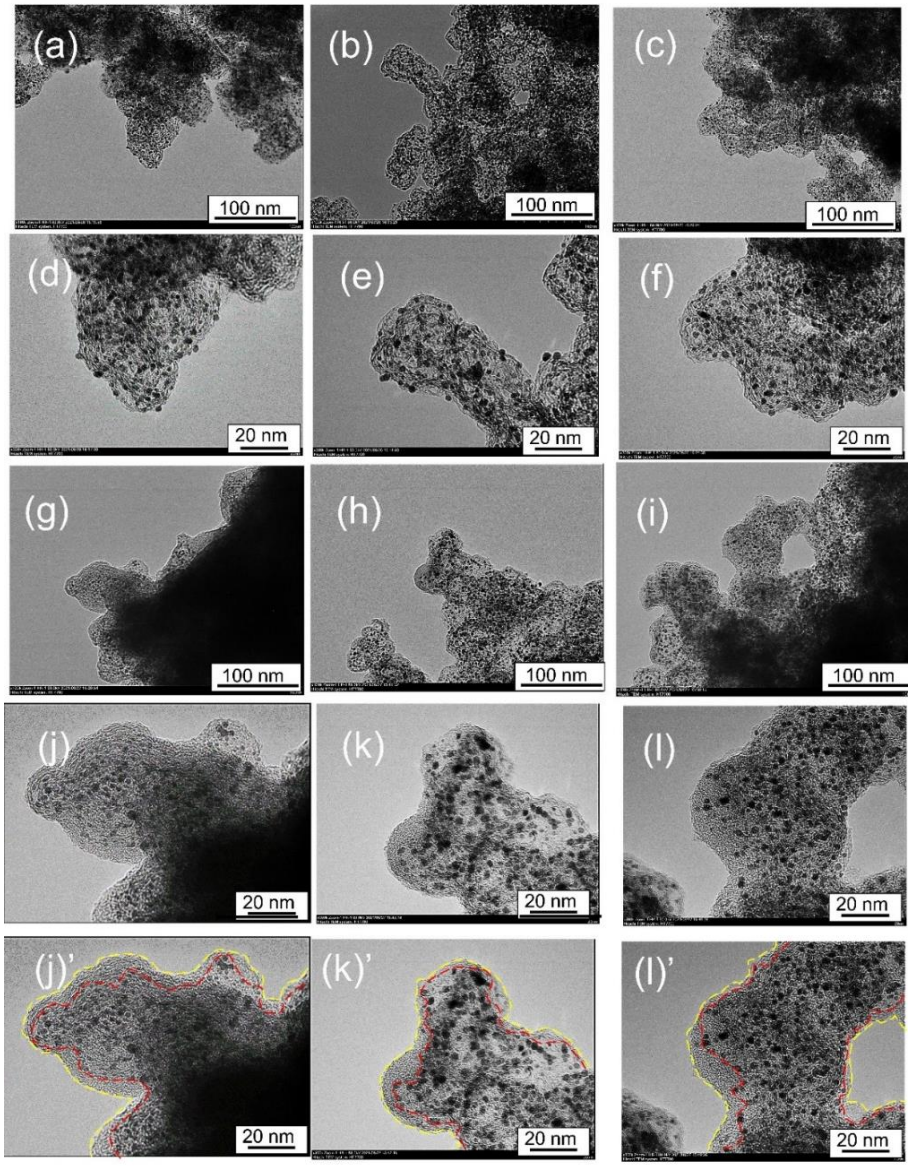

Figure 3-11. Observation image of Pt/K18-5 and Pt/K18-5 with ionomer using low acceleration TEM. (a), (b) and (c) low magnification Pt/K18-5, (d), (e) and (f) high magnification Pt/K18-5, (g), (h) and (i) low magnification Pt/K18-5 with ionomer, (j), (k) and (l) high magnification Pt/K18-5 with ionomer. The ionomer surface (yellow dotted line) and carbon support surface (red dotted line) of (j), (k) and (l) are shown in (j'), (k') and (l').

particle supported in the pores, the higher the oxygen permeation resistance in ionomer. For Pt/K18-5, the exterior Pt surface area was larger than the interior Pt surface area, and ionomer thickly covered the surface of the catalyst, and therefore, the oxygen permeation

resistance became high. Figure 3-10 and Figure 3-11 shows an image of the ionomer covering on the catalyst surface observed with a low acceleration TEM. Pt/K18-5 appears to have a thicker ionomer covering than Pt/K18-4. In recent years, there has been much discussion about the interactions between the ionomer and Pt particles. Kakinuma et al. shows that the ionomer is preferentially adsorbed on Pt on the support surface in Pt/GCB mainly composed of exterior Pt.[35] Park et al. also showed for Pt/GCB that a long side chain ionomer preferentially covers the Pt surface.[67] Ly et al. showed that the larger the Pt particle size, the more likely it is to interact electrostatically with the negatively charged groups (SO_3^-) of the ionomer.[26] My results also more strongly suggest that the presence of Pt strongly attracts the ionomer and has a significant effect on the structure of the catalyst and catalyst layer.

In many studies, inhibition of activity by specific adsorption of ionomer has been investigated under low humidification and high potential conditions (e.g. 0.9 V). However, in actual operation, electric power is generated at a lower voltage and water is generated. Previous studies have shown that the specific adsorption of ionomer on the Pt surface occurs mainly in a dry state or at high potentials,[9,68] and, moreover, other studies have shown that the specific adsorption is mitigated by the presence of water or low potential.[19,69] Therefore, the decrease in activity due to the specific adsorption of ionomer may be relatively small under most actual operating conditions. The accessible carbon I consider has a structure in which there are many Pt particles that are effective in mitigating poisoning depending on the generated water and operating voltage, and the Pt can form a three-phase interface by the generated water. Therefore, I believe that a structure in which the ionomer covers some Pt particles are necessary for improving performance. In the case of the catalyst using the ultrahigh specific surface area carbon

support used in this study, the structure in which approximately 35% of the total Pt particles were on the surface of the support and were covered with ionomer showed the highest performance. I conclude that, when the wt % Pt is changed, the Pt surface area changes as the Pt particle size and the frequency of Pt particles present in the interior and exterior changes, so that the state of ionomer coverage also changes. In previous studies, the relationship between the dispersed state of Pt particles and cell performance has been discussed by focusing on the Pt particle size and internal/external distribution of Pt particles. In this study, I, for the first time, find that the dispersion state of Pt particles affects the covering of ionomer. Since it has a great effect on cell performance, it is important to optimize the wt % Pt for the development of high-performance catalysts. I propose a new perspective that is important for designing high-performance catalysts. In the case of the catalyst using the ECP600JD support, it was confirmed that the 40 wt % Pt catalyst was superior in the low current density region, and the performance of the 30 wt % Pt catalyst becomes superior for increasing current density, as a second choice.

3-3-3. Comparison of cell performance and electrochemical measurements before and after durability test

The $I-V$ curves obtained before and after the durability test for each catalyst are shown in Figure 3-12a. The beginning of testing (BOT) indicates the initial evaluation after activation, and the end of testing (EOT) indicates the evaluation after 2,000 cycles. The I/C value for all cathodes was 1.2, which showed the highest performances in the initial evaluations (ECSA, MA, IR-free voltage at 0.2 A cm^{-2} before the durability test). Pt/K18-4, which had the highest cell performance at BOT, maintained high cell performance at EOT, and Pt/K18-2, which had the lowest performance at BOT, also had the lowest

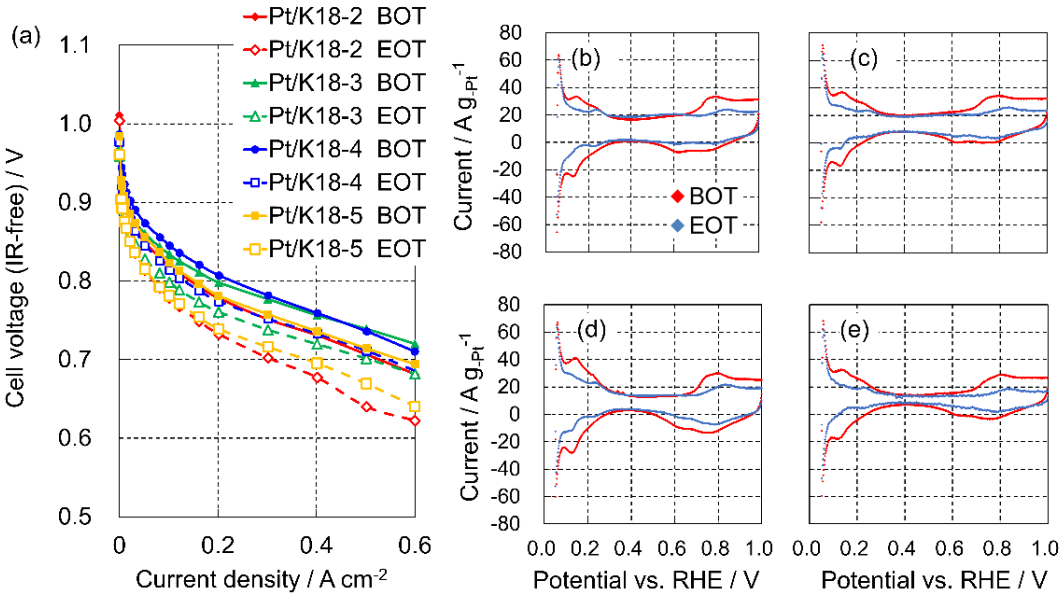

Figure 3-12. (a) $I-V$ curves before (BOT) and after (EOT) startup, shutdown and actual loading durability test. Comparison of changes in cyclic voltammetry of (b) Pt/K18-2, (c) Pt/K18-3, (d) Pt/K18-4, (e) Pt/K18-5 of BOT and EOT.

performance after the durability test. Figure 3-12b−e shows the cyclic voltammograms obtained before (BOT) and after (EOT) the durability test for each catalyst. Since the cyclic voltammograms were not shifted upwards, to the oxidation current side, for any of the catalysts, it is considered that no detectable increase in cross leakage had occurred. These results indicate that the deterioration of the polymer electrolyte membrane hardly occurred, thus, with no effect on the cell performance. Table 3-5 summarizes the ECSA, electric double layer capacity (C_{dl}), and current density at 0.75 V before and after the durability test. In the case of ECSA, these values decreased by about 50−60% for all catalysts. In the case of C_{dl}, various changes were observed. After the durability test, C_{dl} decreased by 7% for both Pt/K18-3 and Pt/K18-4, and decreased by 37% for Pt/K18-5. That for Pt/K18-2 increased about 8%. These results suggest that the catalysts deteriorated via different mechanisms. The overall C_{dl} of the catalyst contains contributions of stored

Table 3-5. Changes in BOT and EOT of ECSA, electric double layer capacity (C_{dl}), and current density at 0.75 V of each catalyst.

	Pt/K18-2	Pt/K18-3	Pt/K18-4	Pt/K18-5
	ECSA / $m^2\ g_{-Pt}^{-1}$			
BOT	73.9	70.8	87.6	73.8
EOT	30.2	36.2	43.2	31.4
Percentage of change	-59.2%	-48.9%	-50.7%	-57.5%
	C_{dl} / $F\ g_{-Pt}^{-1}$			
BOT	393 ± 0.7	297 ± 2.4	260 ± 1.8	178 ± 2.4
EOT	424 ± 2.4	275 ± 4.4	241 ± 0.5	113 ± 11.0
Percentage of change	+7.8%	-7.4%	-7.3%	-36.8%
	Current density / $A\ cm^{-2}$ @ 0.75 V			
BOT	0.31	0.44	0.44	0.34
EOT	0.16	0.25	0.31	0.17
Percentage of change	-48.3%	-43.3%	-29.4%	-48.9%

electrical charge on the surfaces of both Pt and CB. Therefore, the change in C_{dl} at the EOT is a combination of the change for Pt (change in ECSA) and that for carbon. Table 3-6 shows the carbon and Pt allocations in C_{dl} at both BOT and EOT. I calculated the allocations for each C_{dl} from the area percentages of Pt and carbon before the durability test. Furthermore, by calculating the coefficient between the amount of C_{dl} of Pt and ECSA and applying the relational ratio to ECSA after the durability test, the allocation amounts of Pt and carbon in C_{dl} after the durability test were separated. Comparing the changes in carbon allocation in C_{dl} between BOT and EOT, Pt/K18-2 increased while Pt/K18-5 decreased significantly, suggesting that carbon was degraded via different mechanisms. The disordered domains of high specific surface area supports (amorphous

carbon and defective graphite crystals) have been reported to cause carbon corrosion in the actual operating electrode potential range ($0.40 < E < 1.00$ V).[70] The ultrahigh specific surface area supports used in this study are thought to have many disordered domains, and carbon corrosion may occur during actual electrical loading ($1.00 < E < 0.70$ V). In order to avoid carbon corrosion due to reversal current at the time of startup and shutdown, H_2-SU/SD has been proposed, in which the cathode gas valves are closed during the

Table 3-6. Properties of each catalyst measured at (a) the beginning of testing (BOT) and (b) end of testing (EOT) and C_{dl} changes for carbon.

(a)

				(1)		(2)	(3)	(4)
Catalyst	BOT C_{dl}	Specific surface area of Pt ∗	BET specific surface area of catalyst	Pt surface area percentage in catalyst	BOT ECSA	Amount of Pt allocation in C_{dl} of BOT	Amount of carbon allocation in C_{dl} of BOT	Coefficient
Unit	F g_{Pt}^{-1}	m^2 $g_{\text{-carbon}}^{-1}$	m^2 $g_{\text{-carbon}}^{-1}$		m^2 g_{Pt}^{-1}	F g_{Pt}^{-1}	F g_{Pt}^{-1}	F $m^{2\,-1}$
Pt/K18-2	393	28.1	1493	1.88%	73.9	7.4	386	0.10
Pt/K18-3	297	49.0	1279	3.83%	70.8	11.4	286	0.16
Pt/K18-4	260	68.2	1301	5.24%	87.6	13.6	246	0.16
Pt/K18-5	178	99.7	1269	7.86%	73.8	14.0	164	0.19

(b)

			(5)	(6)	(7)	(8)
Catalyst	EOT C_{dl}	EOT ECSA	Amount of Pt allocation in C_{dl} of EOT	Amount of carbon allocation in C_{dl} of EOT	C_{dl} change amount of carbon	C_{dl} change percentage of carbon
Unit	F g_{Pt}^{-1}	m^2 g_{Pt}^{-1}	F g_{Pt}^{-1}	F g_{Pt}^{-1}	F g_{Pt}^{-1}	
Pt/K18-2	424	30.2	3.02	421	35.1	9.10%
Pt/K18-3	275	36.2	5.81	269	-16.5	-5.78%
Pt/K18-4	241	43.2	6.71	234	-12.1	-4.92%
Pt/K18-5	113	31.4	5.96	107	-57.6	-35.03%

∗ Calculated from actual Pt loading percentage shown in Table 3-2 and Pt particle size and interior or exterior frequency in Table 3-3.

The numbers in parentheses refer to the steps in the calculations, as listed below.

(1) Pt surface area percentage in catalyst calculated from the BET specific surface area of catalyst and specific surface of Pt.
(2) Calculate the allocation of Pt to C_{dl}, assuming that the area percentage of Pt and carbon in catalyst is also proportional to C_{dl}.
(3) Divide the C_{dl} allocated to Pt from the C_{dl} of the BOT.
(4) Calculate the coefficient of ECSA and C_{dl} allocated to Pt.
(5) Multiply EOT ECSA by a coefficient to calculate the amount of Pt allocated in C_{dl} after durability test (EOT).
(6) Divide the Pt allocation from EOT C_{dl} to calculate the amount of carbon allocation in C_{dl}.
(7) Calculate the amount of change from BOT C_{dl} and EOT C_{dl} allocated to carbon.
(8) Calculate the C_{dl} change percentage of carbon.

■ Calculation formula

(1) Pt surface area percentage in catalyst = Specific surface area of Pt / BET specific surface area of catalyst × 100
(2) Amount of Pt allocation in C_{dl} of BOT = BOT C_{dl} × Pt surface area percentage in catalyst
(3) Amount of carbon allocation in C_{dl} of BOT = BOT C_{dl} - Amount of Pt allocation in C_{dl} of BOT
(4) Coefficient = Amount of Pt allocation in C_{dl} of BOT / BOT ECSA
(5) Amount of Pt allocation in C_{dl} of EOT = EOT ECSA × Coefficient
(6) Amount of carbon allocation in C_{dl} of EOT = EOT C_{dl} - Amount of Pt allocation in C_{dl} of EOT
(7) C_{dl} change amount of carbon = Amount of carbon allocation in C_{dl} of BOT - Amount of carbon allocation in C_{dl} of EOT
(8) C_{dl} change percentage of carbon = Amount of carbon allocation in C_{dl} of BOT / C_{dl} change amount of carbon × 100

shutdown and the H_2 gas supply of the anode is stopped. In this study as well, the implementation of H_2-SU/SD avoids carbon corrosion due to the generation of high potential (E > 1.00 V). However, the occurrence of carbon corrosion has been confirmed even when H_2-SU/SD is carried out and the potential range is 1.00 or less. Yamashita et

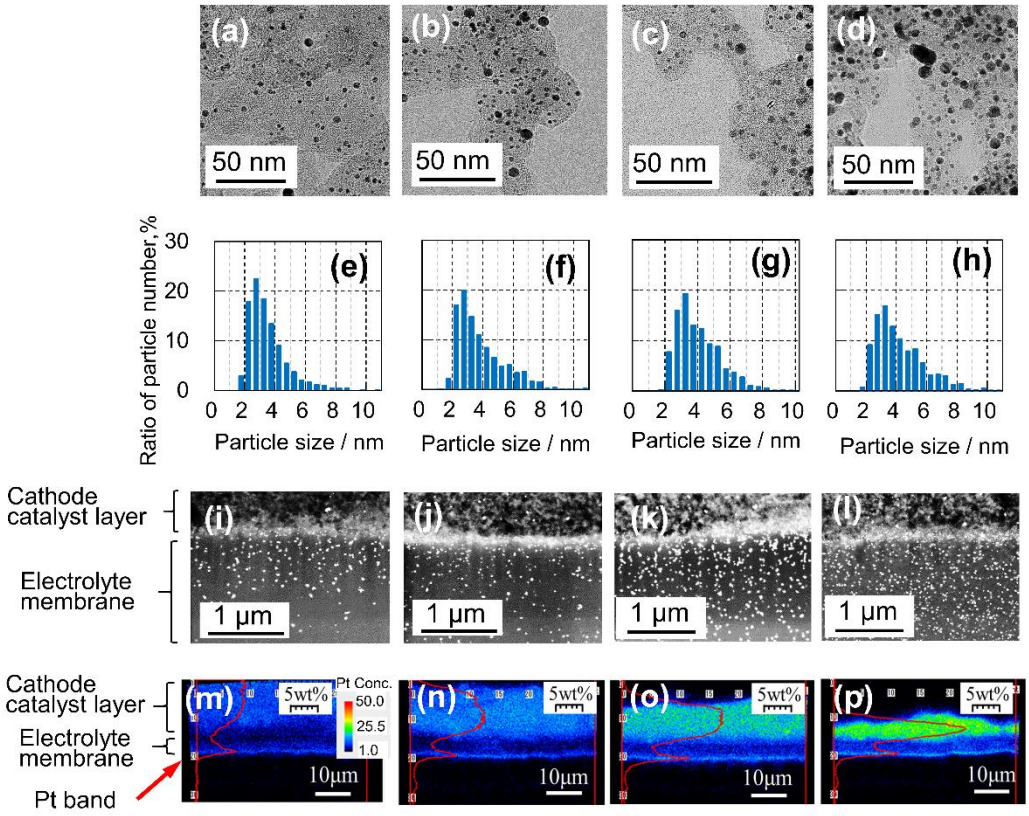

Figure 3-13. Catalyst and electrolyte membrane on the cathode catalyst layer side image and Pt particle size distribution and Pt content in MEA after durability test. TE image of (a) Pt/K18-2, (b) Pt/K18-3, (c) Pt/K18-4 and (d) Pt/K18-5 after durability test. Pt particle size distribution of the catalyst test of (e) Pt/K18-2, (f) Pt/K18-3, (g) Pt/K18-4 and (h) Pt/K18-5. The ZC image of the membrane on the cathode catalyst layer side after the durability test of (i)Pt/K18-2, (j)Pt/K18-3, (k) Pt/K18-4 and (l) Pt/K18-5. Changes in Pt concentration in the cathode catalyst layer and electrolyte membrane by EPMA and Pt concentration line scan (red line) of (m) Pt/K18-2, (n) Pt/K18-3, (o) Pt/K18-4 and (p) Pt/K18-5.

al. proposed carbon corrosion mechanisms for H_2-SU/SD. In the cathode CL during shutdown and startup, the interface between H_2 diffusing from the anode and air in the cathode (H_2-front) or air supplied at startup (air-front) is formed. Due to the heterogeneity of the distribution of ionomer at the areas in the moving interfaces, there are locations where the H^+ pathway disappears, and carbon corrosion occurs because the hydrogen ions

needed for ORR are obtained on the Pt surface by the oxidation reaction of carbon.[48] In their study, at the time of shutdown, only the air supplied to the cathode was stopped, and hydrogen at the anode continued to be supplied. In this study, both the anode and cathode gases were stopped during the stop in order to more simulate the shutdown method of the actual system. As shown in Figure 3-2, at the time of shutdown, the amount of change until the anode and cathode have the same potential and the voltage reaches around 0 V is close to 1 V for all catalysts. Therefore, it can be interpreted that hydrogen remains in the anode and cathode, and it is assumed that carbon corrosion will occur due to H_2-front and air-front proposed by Yamashita et al. Since there is no air at the anode, a high voltage higher than OCV due to the reverse current did not occur when hydrogen was supplied at startup. Comparing the changes in current density at 0.75 V, Pt/K18-4 was significantly less than that of other catalysts. Figures 3-13a−d show TE images of the cathode catalysts after the durability test. The black dots are Pt particles. I confirmed that the lower the wt % Pt, the smaller the average Pt particle size, and the coarsening of Pt particles was suppressed (Table 3-7). Before the durability test, each average Pt particle size was almost the same for all catalysts, but after the durability test, that of Pt/K18-2 with the lowest Pt loading percentage was 3.6 nm and of Pt/K18-5 with the highest Pt loading percentage was 4.3 nm. The carbon surface of the Pt/K18-5 could not be clearly observed compared to other catalysts. This result suggested that a different mode of degradation occurred. Figures 3-13e−h show the results of the particle size distribution of each catalyst. All catalysts have a large number of 3-4 nm Pt particles, and the lower the wt % Pt, the sharper the particle size distribution. This means that many Pt particles were distributed on the carbon support while maintaining a small particle size. Figures 3-13i−l are ZC images of the cross section of the polymer electrolyte membrane on the cathode CL side, and Pt

Table 3-7. Average size of Pt particle and catalyst layer thickness before and after the durability test.

	Catalyst	Pt/K18-2	Pt/K18-3	Pt/K18-4	Pt/K18-5
Particle size / nm	BOT	2.10 ± 0.40	2.03 ± 0.41	2.11 ± 0.39	2.16 ± 0.39
	EOT	3.59 ± 1.24	3.90 ± 1.41	4.07 ± 1.26	4.32 ± 1.54
Catalyst layer thickness / μm	BOT	25.0 ± 4.6	13.6 ± 3.2	11.4 ± 2.6	10.0 ± 2.0
	EOT	17.0 ± 4.2	12.3 ± 2.6	11.0 ± 3.8	6.6 ± 1.7
	Percentage of change	-32.0%	-9.6%	-3.5%	-34.0%

reprecipitated in the polymer electrolyte membrane is seen as white particles. Compared to other catalysts, Pt/K18-5 exhibited a greater number of Pt particles reprecipitated in the polymer electrolyte membrane. In other words, for Pt/K18-5, in addition to the coarsening of the Pt particles, the dissolution and reprecipitation of Pt in the polymer electrolyte membrane has a great influence on the deterioration of cell performance. A cross-sectional image of each catalyst after the durability test is shown in Figure 3-14. Figure 3-13m-p shows the results of EPMA analysis of the cathode CL and polymer electrolyte membrane. The red line shows the Pt content by line analysis. It can be confirmed that a Pt band was formed for all catalysts. It can be confirmed that the higher the wt % Pt of the catalyst, the higher the Pt concentration in the polymer electrolyte membrane between the Pt band and the cathode catalyst, which is consistent with the observation results of the polymer electrolyte membrane images in Figure 3-13i–l. Although ECSA decreased by the same amount in Pt/K18-2 and Pt/K18-5, it is considered that different deterioration mechanisms occur due to the difference in C_{dl} change and the amount of Pt deposited in the polymer electrolyte membrane. The Pt interparticle distance was calculated based on the specific surface area shown in Table 3-2 and the particle size

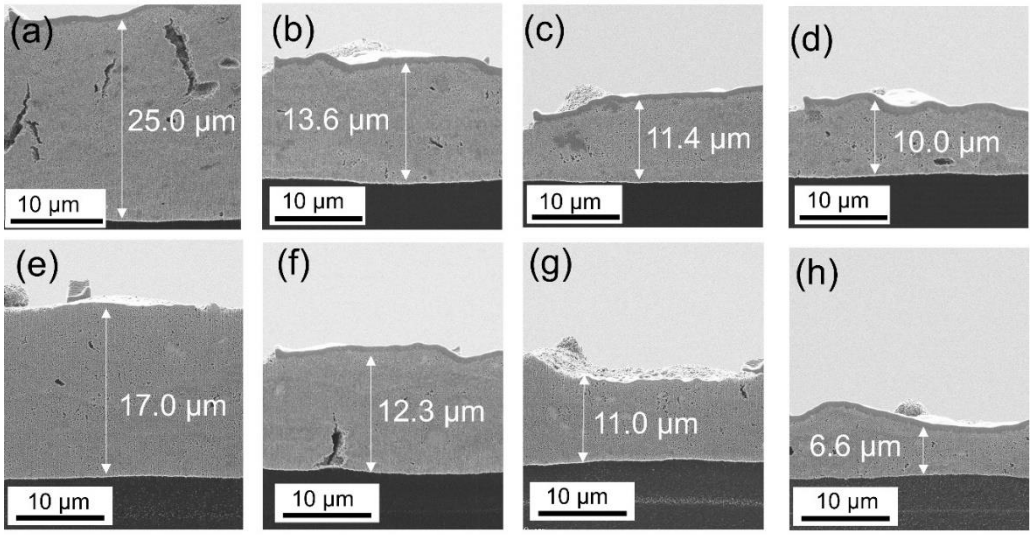

Figure 3-14. Cross-sectional scanning ion microscope (SIM) images and thickness of catalyst layer of each catalyst. Images of (a) Pt/K18-2, (b) Pt/K18-3, (c) Pt/K18-4, and (d) Pt/K18-5 before the durability test and after the durability test of (e) Pt/K18-2, (f) Pt/K18-3, (g) Pt/K18-4, and (h) Pt/K18-5.

shown in Table 3-3. The interparticle distance was 30 nm for Pt/K18-2, 22 nm for Pt/K18-3, 19 nm for Pt/K18-4, and 16 nm for Pt/K18-5. From the results in Table 3-7, it can be said that the coarsening of Pt particle is promoted as the interparticle distance is shorter. However, in the case of longer interparticle distances, it is more difficult for Pt ions to precipitate on adjacent Pt particles (electrochemical Ostwald ripening). I consider that that some Pt ions that could not be reprecipitated on the adjacent Pt particles, which could not be confirmed, may be dissolved in the cathode wastewater and released to the outside of the cell. The thickness of the cathode catalyst layer was measured from the MEA cross-sectional images before and after the FIB-processed durability test (Figure 3-14). In the cross-sectional observation image, the thickness of the catalyst layer is reduced, and it is presumed that the cause is that the surface of the catalyst is oxidized and the volume is reduced. It can be seen that the change in the thickness of the cathode catalyst layer

strongly reflects the effect of carbon corrosion. Pt/K18-2 and Pt/K18-5 have a very large reduction rate before and after the durability test (shown below in Table 3-7). The change in C_{dl} in Table 3-5 and the change in the thickness of the cathode catalyst layer in Table 3-7 show opposite tendencies, but it is judged that these results are caused by the result of large carbon corrosion. In the case of Pt/K18-2, since the wt % of Pt is small, the CL thickness is thick and gas replacement takes time. As the result of C_{dl} change shows, the thickness of the CL is greatly reduced, but it is considered that carbon corrosion in the amorphous state is promoted and it becomes more porous. In the case of Pt/K18-5, it is considered that the catalytic effect of aggregated Pt with a large particle size was large, carbon corrosion was promoted, and both C_{dl} and the thickness the CL were greatly reduced. On the other hand, Pt/K18-4 exhibited the smallest changes in C_{dl} and in the thickness of the catalyst layer. Figure 3-14 shows schematic images of the deterioration mechanism when the wt % Pt is low (Pt/K18-2) and high (Pt/K18-5). Since Pt/K18-2 has

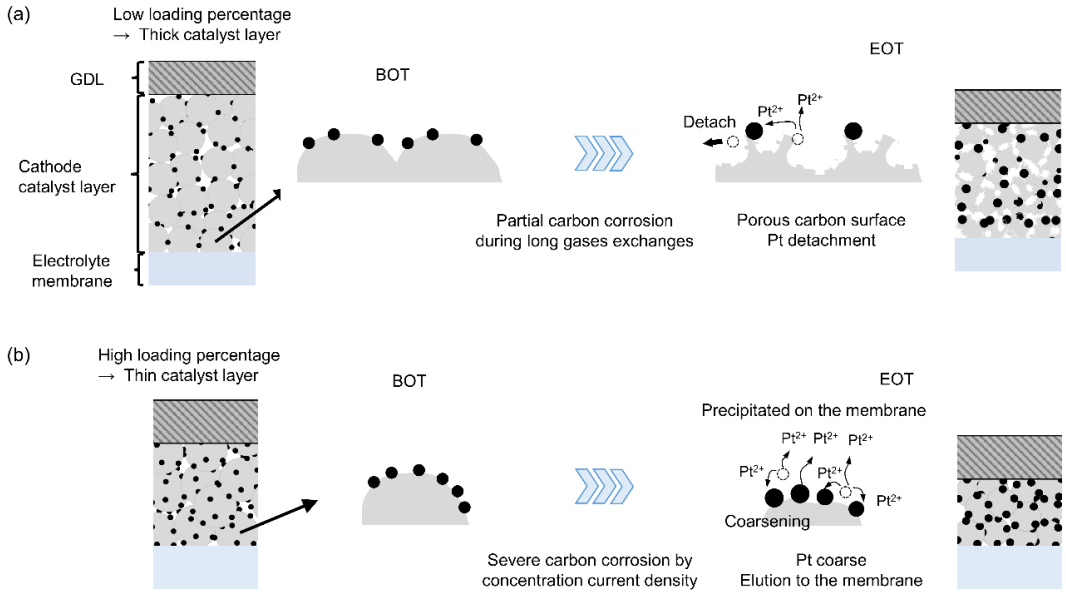

Figure 3-15. Schematic images of catalyst deterioration of (a) Pt/K18-2 and (b) Pt/K18-5.

a low wt % Pt and the CL is thick, and it requires a relatively long time for the air in the cathode CL to be replaced with hydrogen during shutdown or hydrogen to be replaced with air during startup. The H_2-front (Figure 3-2 and Table 3-1) and air-front move slowly during this time. The carbon oxidation reaction (COR) occurs during this long period, carbon corrosion progresses, as shown in Figure 3-15a, and Pt particles are detached from the catalyst. At the locations where Pt is detached, the surface of the carbon support becomes rough and more porous, but since Pt does not exist, no further COR occurs. As a result, in the case of Pt/K18-2, the coarsening of Pt was suppressed, but Pt detached from the catalyst and ECSA decreased. Since the carbon is more porous, C_{dl} increased, and Pt detachment decreased the electrochemically active Pt in the CL, decreasing the amount of Pt dissolved, resulting in less elution into the polymer electrolyte membrane. As shown in Figure 3-2 and Table 3-1, lower wt % Pt during shutdown led to a longer O_2 consumption period. For Pt/K18-2, the time required to consume the O_2 was 1.8 times longer than that for Pt/K18-5. Because the thick CL has large volume, the filling period of H_2 in the cathode CL increased. Similarly, for a thicker CL, the exchange period from H_2 to air is expected to a require a longer time during startup, so it is estimated that Pt/K18-2 will require 1.8 times more time than Pt/K18-5.

In the case of Pt/K18-5, as shown in Figure 3-15b, the distance between the particles is short, and the ionized Pt is likely to reprecipitate on the adjacent Pt particles, so that the Pt particle size becomes large. Since the wt % Pt is high, the CL is thin, and the H_2-front and air-front move quickly, the gas exchange periods are short, thus leading to a short COR generation time. Compared to Pt/K18-2, the increase of carbon surface area by partial carbon corrosion occurring during each shutdown/startup operation would be small. However, the C_{dl} of Pt/K18-5 decreased remarkably. The most likely explanation

is that a severe coarsening of Pt particles occurred, which led to a decrease of the C_{dl} of carbon, since there was less direct corrosion of carbon at the interface between Pt and carbon. From these results, I conclude that the Pt particle did not detach, the particle size increased, and a large amount of Pt also diffused into the polymer electrolyte membrane.

From these durability evaluation results, I conclude that the main deterioration factors change depending on the wt % Pt. In the case of lower wt % Pt, carbon roughening by partial corrosion during the longer gas exchange time led to a porous surface, and Pt particle detachment occurred. In the case of high wt % Pt, the concentration of current density in the thinner CL led to Pt particle coarsening, severe carbon corrosion, and Pt dissolution into the membrane. In particular, CB supports that have a large internal nanopore volume are vulnerable to coarsening of Pt particle on the exterior surface of the CB support and carbon deterioration due to the uneven distribution of ionomer thereon, which contributes to the types of deterioration above. In order to design a highly durable catalyst, it is important to consider the situation from the viewpoint of the thickness of the CL and the distance between Pt particles when the wt % Pt is changed. When the ECP600JD support was used with the 40 wt % Pt loading, the CL was sufficiently thin to suppress the carbon corrosion, and the long interparticle distance allowed Pt to be maintained as small particles, thus showing high durability.

3-4. Conclusions

In order to design a high-performance catalyst, I investigated the effect of the catalyst structure on the ionomer covering state and cell performance. The structure of the catalyst was varied by preparing catalysts with different wt % Pt values, using an ultrahigh

specific surface area carbon support (ECP600JD, ca. 1800 m^2 / g). In this study, the Pt loading percentage (wt % Pt) on the carbon was varied from 20 wt % to 50 wt %. The higher the wt % Pt, the higher the Pt particle frequency on the exterior surface of the carbon. Along with this, the exterior Pt surface area also increased. I suggest that, when the Pt surface area corresponding to the exterior surface of the CB support is larger than that corresponding to interior surface, the ionomer covers the surface of the exterior Pt thickly, increasing the oxygen permeation resistance in the ionomer. Therefore, the oxygen diffusion resistance increased and caused the deterioration of the cell performance. I have shown that catalyst design focusing on the Pt surface areas corresponding to interior and exterior surfaces is important for optimizing the state of ionomer coverage to maximize the performance of the catalyst.

In addition, the combined durability test protocol constructed with startup, shutdown and galvanostatic load cycling was evaluated to clarify the effect of the difference in wt % Pt on durability. From the results of the electrochemical measurements and the observation of the CL, it is concluded that different deterioration mechanisms occur depending on the difference in the wt % Pt. In the case of the catalyst having a low wt % Pt, since the distance between particles is long, coarsening of Pt particles is suppressed, but the CL becomes thick. It requires a long period for the air in the cathode CL to be replaced by H_2 during shutdown or the H_2 to be replaced by air during startup. In that case, the slow movement of the H_2-front or air-front leads to a severe carbon corrosion, causing Pt particles to detach from the support and degrading cell performance. In contrast, in the case of the catalyst having a high wt % Pt, these gas-fronts move quickly, and the number of Pt particles detaching from the support is small, but the distance between the catalysts is short, so that the Pt particles are likely to be coarsened. As the

coarsening of Pt particles continues, ECSA decreases, and more Pt elutes into the polymer electrolyte membrane, resulting in a decrease in cell performance.

From the viewpoints of both initial performance and durability, the catalysts with approximately 40 wt % Pt, which are in the mid-range of those commonly used, can be considered to combine high performance and high durability. In order to improve performance and durability, it is important to design the Pt interior and exterior distribution so that the ionomer does not thickly cover the pore entrance, and to make use of a wt % Pt that minimizes carbon corrosion and coarsening of Pt particles.

In the present study, the advanced characterization and optimization of the Pt/C catalysts with various values of wt % Pt on the ultrahigh surface area CB, combined with extensive performance and durability testing, have provided an unprecedented level of understanding of the reaction sites and mass transport characteristics that are essential for achieving high performance and stability, which are crucial for their practical application in PEFCs.

3-5. References

1 Tabe, Y.; Nishino, M.; Takamatsu, H.; Chikahisa, T. Effects of Cathode Catalyst Layer Structure and Properties Dominating Polymer Electrolyte Fuel Cell Performance. *J. Electrochem. Soc.* 2011, 158, B1246–B1254.

2 Padgett, E.; Yarlagadda, V.; Holtz, M, E.; Ko, M.; Levin, B, D, A.; Kukreja, R, S.; Ziegelbauer, J, M.; Andrews, R, N.; Ilavsky, J.; Kongkanand, A.; Muller, D, A. Mitigation of PEM Fuel Cell Catalyst Degradation with Porous Carbon Supports. *J. Electrochem. Soc.* 2019, 166, F198−207.

3 Park, Y.-C.; Tokiwa, H.; Kakinuma, K.; Watanabe, M.; Uchida, M. Effects of Carbon Supports on Pt Distribution, Ionomer Coverage and Cathode Performance for Polymer Electrolyte Fuel Cells. *J. Power Sources* 2016, 315, 179–191.

4 Jayawickrama, S, M.; Fujigaya, T. Effect of Polymer-Coating on Carbon Blacks for Pt Utilization Efficiency of Polymer Electrolyte Membrane Fuel Cells. *J. Power Sources* 2021, 482, 228932.

5 Soboleva, T.; Zhao, X.; Malek, K.; Xie, Z.; Navessin, T.; Holdcroft, S. On the Micro-, Meso-, and Macroporous Structures of Polymer Electrolyte Membrane Fuel Cell Catalyst Layers. *ACS Appl. Mater. Interfaces* 2010, 2, 375–384.

6 Soboleva, T.; Malek, K.; Xie, Z.; Navessin, T.; Holdcroft, S. PEMFC Catalyst Layers: The Role of Micropores and Mesopores on Water Sorption and Fuel Cell Activity. *ACS Appl. Mater. Interfaces* 2011, 3, 1827–1837.

7 Kim, M.; Park, J.-N.; Kim, H.; Song, S.; Lee, W.-H. The Preparation of Pt/C Catalysts Using Various Carbon Materials for the Cathode of PEMFC. *J. Power Sources* 2006, 163, 93–97.

8 Kodama, K.; Shinohara, A.; Hasegawa, N.; Shinozaki, K.; Jinnouchi, R.; Suzuki, T.; Hatanaka, T.; Morimoto, Y. Catalyst Poisoning Property of Sulfonimide Acid Ionomer on Pt (111) Surface. *J. Electrochem. Soc.* 2014, 161, F649–F652.

9 Shinozaki, K.; Morimoto, Y.; Pivovar, B, S.; Kocha, S, S. Suppression of Oxygen Reduction Reaction Activity on Pt-Based Electrocatalysts from Ionomer Incorporation. *J. Power Sources* 2016, 325, 745–751.

10 Tymoczko, J.; Vallejo, F, C.; Colic, V.; Koper, M, T, M.; Schuhmann, W.; Bandarenka, A, S. Oxygen Reduction at a Cu Modified Pt (111) Model Electrocatalyst in Contact with Nafion polymer. *ACS Catal.* 2014, 4, 3772–3778.

11 Kodama, K.; Motobayashi, K.; Shinohara, A.; Hasegawa, N.; Kudo, K.; Jinnouchi, R.; Osawa, M.; Morimoto, Y. Effect of the Side-Chain Structure of Perfluoro-Sulfonic Acid Ionomers on the Oxygen Reduction Reaction on the Surface of Pt. *ACS Catal.* 2018, 8, 694–700.

12 Uchida, M.; Park, Y.-C.; Kakinuma, K.; Yano, H.; Tryk, D. A.; Kamino, T.; Uchida, H.; Watanabe, M. Effect of the State of Distribution of Supported Pt Nanoparticles on Effective Pt Utilization in Polymer Electrolyte Fuel Cells. *Phys. Chem. Chem. Phys.* 2013, 15, 11236–11247.

13 Shinozaki, K.; Yamada, H.; Morimoto, Y. Relative Humidity Dependence of Pt Utilization in Polymer Electrolyte Fuel Cell Electrodes: Effects of Electrode Thickness, Ionomer-to-Carbon Ratio, Ionomer Equivalent Weight, and Carbon Support. *J. Electrochem. Soc.* 2011, 158, B467–475.

14 Fernandez, R, T.; Siddharthan, A, V.; Kurungot, S. In Situ Preparation of Ionomer as a Tool for Triple-Phase Boundary Enhancement in 3D Graphene Supported Pt Catalyst. *Adv. Sustainable Syst.* 2021, 5. 2000125.

15 Iden, H.; Mashio, T.; Ohma, A. Gas Transport Inside and Outside Carbon Supports of Catalyst Layers for PEM Fuel Cells. *J. Electrochem. Soc.* 2013, 708, 87–94.

16 Du, F.; Dao, T, A.; Peitl, P, V. J.; Bauer, A.; Preuss, K.; Bonastre, A, M.; Sharman, J.; Spikes, G.; Perchthaler, M.; Schmidt, T, J.; Orfanidi, A. Effects of PEMFC Operational History under Dry/Wet Conditions on Additional Voltage Losses due to Ionomer Migration. *J. Electrochem. Soc.* 2020, 167, 144513.

17 Padgett, E.; Andrejevic, N.; Liu, Z.; Kongkanand, A.; Gu, W.; Moriyama, K.; Jiang, Y.; Kumaraguru, S.; Moylan, T. E.; Kukreja, R.; Muller, D. A. Connecting Fuel Cell

Catalyst Nanostructure and Accessibility Using Quantitative Cryo-STEM Tomography. *J. Electrochem. Soc.* 2018, 165, F173–F180.

18 Peng, Y.; Choi, J.-Y.; Fürstenhaupt, T.; Bai, K.; Zhang, Y.; Banham, D. New Approach for Rapidly Determining Pt Accessibility of Pt/C Fuel Cell Catalysts. *J. Mater. Chem. A* 2021, 9, 13471–13476.

19 Hanawa, H.; Kunimatsu, K.; Watanabe, M.; Uchida, M. In Situ ATR-FTIR Analysis of the Structure of Nafion–Pt/C and Nafion–Pt_3Co/C Interfaces in Fuel Cell. *J. Phys. Chem. C* 2012, 116, 21401–21406.

20 Harzer, G. S.; Orfanidi, A.; El-Sayed, H.; Madkikar, P.; Gasteiger, H. A. Tailoring Catalyst Morphology towards High Performance for Low Pt Loaded PEMFC Cathodes. *J. Electrochem. Soc.* 2018, 165, F770−F779.

21 Kongkanand, A.; Yarlagadda, V.; Garrick, T, R.; Moylan, T, E.; Gu, W. Electrochemical Diagnostics and Modeling in Developing the PEMFC Cathode. *ECS Trans.* 2016, 75, 25.

22 Yarlagadda, V.; Carpenter, M. K.; Moylan, T. E.; Kukreja, R. S.; Koestner, R.; Gu, W.; Thompson, L.; Kongkanand, A. Boosting Fuel Cell Performance with Accessible Carbon Mesopore. *ACS Energy Lett.* 2018, 3, 618–621.

23 Ko, M.; Padgett, E.; Yarlagadda, V.; Kongkanand, A.; Muller, D, A. Revealing the Nanostructure of Mesoporous Fuel Cell Catalyst Supports for Durable, High-Power Performance. *J. Electrochem. Soc.* 2021, 168, 024512.

24 Ramaswamy, N.; Gu, W.; Ziegelbauer, J. M.; Kumaraguru, S. Carbon Support Microstructure Impact on High Current Density Transport Resistances in PEMFC Cathode. *J. Electrochem. Soc.* 2020, 167, 064515.

25 Alegre, C.; Gálvez, M, E.; Moliner, R.; Baglio, V.; Aricò, A, S.; Lázaro, M, J. Towards an Optimal Synthesis Route for the Preparation of Highly Mesoporous Carbon Xerogel-Supported Pt Catalysts for the Oxygen Reduction Reaction. *Appl. Catal., B* 2014, 147, 947–957.

26 Ly, A.; Asset, T.; Atanassov, P. Integrating Nanostructured Pt-Based Electrocatalysts in Proton Exchange Membrane Fuel Cells. *J. Power Sources* 2020, 478, 228516.

27 Shintani, H.; Miyata, N.; Sugawara, Y. A Model for Mesoporous Carbon-Supported Platinum Catalyst/Electrolyte Interfaces in Polymer Electrolyte Fuel Cells. *J. Power Sources* 2021, 487, 229414.

28 Matsumoto, K.; Hiyoshi, M.; Iijima, T. Application of Mesoporous Carbon Nano Dendrites (MCND) As Catalyst Supporting Materials for PEFCs. *Meet. Abstr*. 2013, MA2013−02, 1617.

29 Numao, S.; Judai, K.; Nishijo, J.; Mizuuchi, K.; Nishi, N. Synthesis and Characterization of Mesoporous Carbon Nano-Dendrites with Graphitic Ultra-Thin Walls and Their Application to Supercapacitor Electrodes. *Carbon* 2009, 47, 306–312.

30 Ahn, C.-Y.; Cheon, J.-Y.; Joo, S.-H.; Kim, J. Effects of Ionomer Content on Pt Catalyst/Ordered Mesoporous Carbon Support in Polymer Electrolyte Membrane Fuel Cells. *J. Power Sources* 2013, 222, 477–482.

31 Kamitaka, Y.; Takeshita, T.; Morimoto, Y. MgO-Templated Mesoporous Carbon as a Catalyst Support for Polymer Electrolyte Fuel Cells. *Catalysts* 2018, 8, 230.

32 Joo, S, H.; Park, C.; You, D, J.; Lee, S, A.; Lee, H, I.; Kim, J, M.; Chang, H.; Seung, D. Ordered Mesoporous Carbons (OMC) as Supports of Electrocatalysts for Direct

Methanol Fuel Cells (DMFC): Effect of Carbon Precursors of OMC on DMFC Performances. *Electrochim. Acta* 2006, 52, 1618–1626.

33 Rahman, Md, M.; Inaba, K.; Batnyagt, G.; Saikawa, M.; Kato, Y.; Awata, R.; Delgertsetsega, B.; Kaneta, Y.; Higashi, K.; Uruga, T.; Iwasawa, Y.; Ui, K.; Takeguchi, T. Synthesis of Catalysts with Fine Platinum Particles Supported by High-Surface-Area Activated Carbons and Optimization of their Catalytic Activities for Polymer Electrolyte Fuel Cells. *RSC Adv.* 2021, 11, 20601.

34 Kakinuma, K.; Kawamoto, M.; Tamoto, K.; Yamaguchi, M.; Honmura, S.; Iiyama, A.; Uchida, M. Evaluation of Ionomer Distribution on Electrocatalysts for Polymer Electrolyte Fuel Cells by Use of a Low Acceleration Voltage Scanning Electron Microscope. *J. Electrochem. Soc.* 2021, 168, 054510.

35 Kakinuma, K.; Kobayashi, R.; Iiyama, A.; Uchida, M. Influence of Ionomer Content on Both Cell Performance and Load Cycle Durability for Polymer Electrolyte Fuel Cells Using Pt/Nb-SnO_2 Cathode Catalyst Layers. *J. Electrochem. Soc.* 2018, 165, J3083–J3089.

36 Cullen, D, A.; Koestner, R.; Kukreja, R, S.; Liu, Z, Y.; Minko, S.; Trotsenko, O.; Tokarev, A.; Guetaz, L.; Meyer III, H, M.; Parish, C, M.; Moref, K, L. Imaging and Microanalysis of Thin Ionomer Layers by Scanning Transmission Electron Microscopy. *J. Electrochem. Soc.* 2014, 161, F1111–F1117.

37 Kobayashi, A.; Fujii, T.; Harada, C.; Yasumoto, E.; Takeda, K.; Kakinuma, K.; Uchida, M. Effect of Pt and Ionomer Distribution on Polymer Electrolyte Fuel Cell Performance and Durability. *ACS Appl. Energy Mater.* 2021, 4, 2307–2317.

38 Sandbeck, D, J, S.; Secher, N, M.; Inaba, M.; Quinson, J.; Sørensen, J, E.; Kibsgaard, J.; Zana, A.; Bizzotto, F.; Speck, F, D.; Paul, M, T, Y.; Dworzak, A.; Dosche, C.;

Oezaslan, M.; Chorkendorff, I.; Arenz, M.; Cherevko, S. The Dissolution Dilemma for Low Pt Loading Polymer Electrolyte Membrane Fuel Cell Catalysts. *J. Electrochem. Soc.* 2020, 167, 164501.

39 Babu, S, K.; Mukundan, R.; Wang, C.; Langlois, D.; Cullen, D, A.; Papadias, D.; More, K, L.; Ahluwalia, R.; Waldecker, J.; Borup, R. Effect of Catalyst and Catalyst Layer Composition on Catalyst Support Durability. *J. Electrochem. Soc.* 2021, 168, 044502

40 Castanheira, L.; Silva, W, O.; Lima, F, H, B.; Crisci, A.; Dubau, L.; Maillard, F. Carbon Corrosion in Proton-Exchange Membrane Fuel Cells: Effect of the Carbon Structure, the Degradation Protocol, and the Gas Atmosphere. *ACS Catal.* 2015, 5, 2184–2194.

41 Horn, Y, S.; Sheng, W, C.; Chen, S.; Ferreira, P, J.; Holby, E, F.; Morgan, D. Instability of Supported Platinum Nanoparticles in Low-Temperature Fuel Cells. *Top. Catal.* 2007, 46, 285–305.

42 Mayrhofer, K, J, J.; Meier, J, C.; Ashton, S, J.; Wiberg, G, K, H.; Kraus, F.; Hanzlik, M.; Arenz, M. Fuel Cell Catalyst Degradation on the Nanoscale. *Electrochem. Commun.* 2008, 10, 1144–1147.

43 Guilminot, E.; Corcella, A.; Charlot, F.; Maillard, F.; Chateneta, M. Detection of Pt^{z+} Ions and Pt Nanoparticles Inside the Membrane of a Used PEMFC. *J. Electrochem. Soc.* 2007, 154, B96–B105.

44 Xie, J.; Wood III, D, L.; Wayne, D, M.; Zawodzinski, T, A.; Atanassov, P.; Borupa, R, L. Durability of PEFCs at High Humidity Conditions. *J. Electrochem. Soc.* 2005, 152, A104–A113.

45 Dilleta, J.; Lamibraca, A.; Maranzanaa, G.; Durstc, J.; Spernjakd, D.; Fairweatherd, J.; Mukundand, R.; Borupd, R, L.; Didierjeana, S.; Lottina, O. Internal Currents, CO_2 Emissions and Decrease of the Pt Electrochemical Surface Area during Fuel Cell Start-Up and Shut-Down. *ECS Trans.* 2012, 50, 701–710.

46 Wang, C.; Ricketts, M.; Soleymani, A, P.; Jankovic, J.; Waldecker, J.; Chen, J. Effect of Carbon Support Characteristics on Fuel Cell Durability in Accelerated Stress Testing. *J. Electrochem. Soc.* 2021, 168, 044507.

47 Mittermeier, T.; Weiß, A.; Hasché, F.; Hübner, G.; Gasteiger, H, A. PEM Fuel Cell Start-up Shut-down Losses vs Temperature for Non-Graphitized and Graphitized Cathode Carbon Supports. *J. Electrochem. Soc.* 2017, 164, F127–F137.

48 Yamashita, Y.; Itami, S.; Takano, J.; Kakinuma, K.; Uchida, H.; Watanabe, M.; Iiyama, A.; Uchida, M. Degradation Mechanisms of Carbon Supports under Hydrogen Passivation Startup and Shutdown Process for PEFCs. *J. Power Sources* 2017, 164, F181–F187.

49 Speder, J.; Zana, A.; Spanos, I.; Kirkensgaard, J, J, K.; Mortensen, K.; Hanzlik, M.; Arenz, M. Comparative Degradation Study of Carbon Supported Proton Exchange Membrane Fuel Cell Electrocatalysts - The Influence of the Platinum to Carbon Ratio on the Degradation Rate. *J. Power Sources* 2014, 261, 14–22.

50 Ohma, A.; Shinohara, K.; Iiyama, A.; Yoshida, T.; Daimaru, A. Membrane and Catalyst Performance Targets for Automotive Fuel Cells by FCCJ Membrane, Catalyst, MEA WG. *ECS Trans.* 2011, 41, 775–784.

51 Takei, C.; Kakinuma, K.; Kawashima, K.; Tashiro, K.; Watanabe, M.; Uchida, M. Load Cycle Durability of a Graphitized Carbon Black-Supported Platinum Catalyst in Polymer Electrolyte Fuel Cell Cathodes. *J. Power Sources* 2016, 324, 729–737.

52 Neimark, A. V.; Lin, Y.; Ravikovitch, P. I.; Thommes, M. Quenched Solid Density Functional Theory and Pore Size Analysis of Micro-Mesoporous Carbons. *Carbon* 2009, 47, 1617-1628.

53 Carter, R, N.; Kocha, S, S.; Wagner, F, T.; Fay, M.; Gasteiger, H, A. Artifacts in Measuring Electrode Catalyst Area of Fuel Cells through Cyclic Voltammetry. *ECS Trans.* 2007, 11, 403–410.

54 Katayama, S.; Sugawara, S. Electrochemical Method to Quantitate Gas Transport Resistance at Immediate Vicinity of Catalyst Surface in Polymer Electrolyte Fuel Cells. *J. Power Sources* 2021, 483, 229178.

55 Fukuyama, Y.; Shiomi, T.; Kotaka, T.; Tabuchi, Y. The Impact of Platinum Reduction on Oxygen Transport in Proton Exchange Membrane Fuel Cells. *Electrochim. Acta* 2014, 117, 367–378.

56 Kudo, K.; Jinnouchi, R.; Morimoto, Y. Humidity and Temperature Dependences of Oxygen Transport Resistance of Nafion Thin Film on Platinum Electrode. *Electrochim. Acta* 2016, 209, 682–690.

57 Nonoyama, N.; Okazaki, S.; Weber, A, Z.; Ikogi, Y.; Yoshida, T. Analysis of Oxygen-Transport Diffusion Resistance in Proton-Exchange-Membrane Fuel Cells. *J. Electrochem. Soc.* 2011, 158, B416–B423.

58 Cho, S.; Tamoto, K.; Uchida, M. Effect of an Electrospray-Generated Ionomer Morphology on Polymer Electrolyte Fuel Cell Performance. *Energy Fuels* 2020, 34, 14853–14863.

59 Xie, J.; More, K, L.; Zawodzinski, T, A.; Smith, W, H. Porosimetry of MEAs Made by "Thin Film Decal" Method and Its Effect on Performance of PEFCs. *J. Electrochem. Soc.* 2004, 151, A1841–A1846.

60 Thommes, M.; Kaneko, K.; Neimark, A, V.; Olivier, J, P.; Reinoso, F, R.; Rouquerol, J.; Sing, K, S, W. Physisorption of Gases, with Special Reference to the Evaluation of Surface Area and Pore Size Distribution (IUPAC Technical Report). *Pure Appl. Chem.* 2015, 87, 1051–1069.

61 Jung, W, S.; Popov, B, N. Hybrid Cathode Catalyst with Synergistic Effect between Carbon Composite Catalyst and Pt for Ultra-Low Pt Loading in PEMFCs. *Catal. Today* 2017, 295, 65–74.

62 Uchida, M.; Fukuoka, Y.; Sugawara, Y.; Eda, N.; Ohta, A. Effects of Microstructure of Carbon Support in the Catalyst Layer on the Performance of Polymer-Electrolyte Fuel Cells. *J. Electrochem. Soc.* 1996, 143, 2245–2252.

63 Ngo, T, T.; Yu, T, L.; Lin, H, L. Influence of the Composition of Isopropyl Alcohol/Water Mixture Solvents in Catalyst Ink Solutions on Proton Exchange Membrane Fuel Cell Performance. *J. Power Sources* 2013, 225, 293–303.

64 Noskov, S, Y.; Lamoureux, G.; Roux, B. Molecular Dynamics Study of Hydration in Ethanol-Water Mixtures Using a Polarizable Force Field. *J. Phys. Chem. B* 2005, 109, 6705–6713.

65 Male, K.; Mashio, T.; Eikerling, M. Microstructure of Catalyst Layers in PEM Fuel Cells Redefined: A Computational Approach. *Electrocatalysis* 2011, 2, 141–157.

66 Takeshita, T.; Kamitaka, Y.; Shinozaki, K.; Kodama, K.; Morimoto, Y. Evaluation of Ionomer Coverage on Pt Catalysts in Polymer Electrolyte Membrane Fuel Cells by CO Stripping Voltammetry and its Effect on Oxygen Reduction Reaction Activity. *J. Electroanal. Chem.* 2020 871, 114250.

67 Park, Y.-C.; Kakinuma, K.; Uchida, H.; Watanabe, M. Effects of Short-Side-Chain Perfluorosulfonic Acid Ionomers as Binders on the Performance of Low Pt Loading Fuel Cell Cathodes. *J. Power Sources* 2015, 275, 384–391.

68 Kodama, K.; Jinnouchi, R.; Suzuki, T.; Murata, H.; Hatanaka, T.; Morimoto, Y. Increase in Adsorptivity of Sulfonate Anions on Pt (111) Surface with Drying of Ionomer. *Electrochem. Commun.* 2013, 36, 26–28.

69 Jomori, S.; Komatsubara, K.; Nonoyama, N.; Kato, M.; Yoshida, T. An Experimental Study of the Effects of Operational History on Activity Changes in a PEMFC. *J. Electrochem. Soc.* 2013, 160, F1067–F1073.

70 Castanheira, L.; Dubau, L.; Mermoux, M.; Berthomé, G.; Caqué, N.; Rossinot, E.; Chatenet, M.; Maillard, F. Carbon Corrosion in Proton-Exchange Membrane Fuel Cells: From Model Experiments to Real-Life Operation in Membrane Electrode Assemblies. *ACS Catal.* 2014, 4, 2258–2267.

Chapter 4 General Conclusion and Future Prospect

4-1. General conclusions

A fuel cell is an environment-friendly power generation device that does not emit CO2 during power generation and is capable of electrochemically reacting hydrogen and oxygen to directly convert chemical energy into electrical energy. Among fuel cells, polymer electrolyte fuel cells (PEFCs) are expected to be widely used for households and automobiles because of their low operating temperature and short startup time. However, in order to promote the electrochemical reaction in PEFC, it is necessary to use a catalyst containing a large amount of expensive Pt, especially as a cathode catalyst, which increases the cost and is one of the factors hindering its widespread use. In recent years, it has been reported that the sulfonic acid group of ionomer is adsorbed on the surface of Pt particles, which inhibits ORR activity under high voltage and low humidification conditions and causes deterioration of cell performance. Therefore, the idea of forming a three-phase interface with the generated water with ionomer without covering the surface of Pt as much as possible has accelerated the development of catalysts using carbon supports with high specific surface areas with many pores that ionomers cannot penetrate. On the other hand, some studies have shown that ionomer adsorption is mitigated in atmospheres with water or low voltage. Therefore, in actual fuel cell operation, the decrease in activity due to ionomer poisoning is not considered to be as great as the concern in previous studies. I think it is important that there are both Pt that is covered with ionomer to form a three-phase interface and Pt that is covered with water generated during operation to form a three-phase interface. In other words, I think that it is indispensable for a high-performance catalyst to have a structure in which Pt supported

on the surface of the carbon support and Pt supported inside the catalyst pores where ionomer cannot penetrate are present. In this study as well, the structure in which Pt is present both on the surface of the carbon support and in the catalyst pores (40 wt % Pt) shows the highest performance, so it is considered that the results supporting my claim above were obtained. In addition, it is known from previous studies that various operation patterns deteriorate the cathode catalyst and deteriorate the cell performance, so that a large amount of Pt is required. Cost reduction and improvement of durability are the most important issues for the spread of PEFC, and for that purpose, it is important to improve the cell performance and maintain the cell performance for a long time. Against this background, in this study, I focused on the effect of the catalyst structure on cell performance and durability under actual operation conditions in PEFC cathode catalysts and aimed to clarify the catalyst structure that leads to cost reduction and durability improvement.

In Chapter 2, I analyzed the structure of the CB support of catalyst and the covering state of ionomer, which is responsible for proton conduction, using four types of CB supports, and examined the relationship with cell performance. I suggested that if the amount of ionomer is appropriate in a catalyst using HSC support with many large diameter pores, the ionomer penetrates into the pores of the catalyst to some extent and also covers interior Pt, and it also improves Pt utilization, resulting in high cell performance. On the other hand, when the amount of ionomer becomes excessive, the pores of the catalyst are blocked by ionomer and O_2 transport is hindered, resulting in deterioration of cell performance. Many studies have shown that the Pt present in the catalyst pores is not covered with ionomer. The results of N_2-adsorption measurements, STEM observation, and electrochemical measurement in this study suggest that an appropriate amount of

ionomer penetrates into the pores and also covers the interior Pt. Furthermore, it was suggested that the dispersion of Pt, the state of ionomer covering on interior Pt, and the Pt utilization change depending on the specific surface area, pore diameter, and pore volume, and I suggested the importance of CB support design. Durability was examined using a protocol that simulated actual load operation cycling. The catalyst using ultrahigh surface area support (ECP600JD) suppresses the coarsening of Pt particles, and the decrease in Pt on the polymer electrolyte membrane side in the cathode catalyst layer is small, maintaining high ECSA and high cell performance even after the durability test. It is considered that this is because the coarsening is suppressed by the long distance between the Pt particles, and the elution into the polymer electrolyte membrane is suppressed because the Pt particles have a structure that easily stays in the pores. Since the higher the specific surface area CB support is, the more activation is performed and the more disordered domains are present, it is considered that the catalyst using ECP600JD may cause carbon corrosion in the operating electrode potential range. Since CB support with a larger specific surface area is activated more and has many disordered domains, it is considered that the catalyst using ECP600JD may cause carbon corrosion in the operating electrode potential range. However, in this study, no significant carbon corrosion was observed, and it was confirmed that it showed high durability. In this study, I showed the relationship and mechanism between the pore structure of the HSC catalyst, cell performance and durability, which was unclear in the previous studies, and showed the design guideline for the CB support.

In Chapter 3, I focused on the dispersion of Pt particles in the catalyst. Using the difference in the Pt loading percentage of the catalyst, which had the highest performance in Chapter 2, the effect of the difference in the presence state of Pt particles on the cell

performance was investigated. It was suggested that a catalyst with too much exterior Pt would make it difficult for ionomer to penetrate into the pores, resulting in a structure that thickly covers the surface of exterior Pt. It has been found that such a structure leads to a decrease in oxygen diffusivity in ionomer covering the surface of the Pt particles, resulting in a decrease in cell performance. I suggest that by properly designing the distribution of Pt in the catalyst, high cell performance can be achieved because it can reduce ionomer poisoning by the generated water during operation and the diffusion resistance of oxygen in the ionomer. Durability was examined using a protocol that combines startup, shutdown and galvanostatic load cycling. Since the catalyst layer of the low Pt loading percentage catalyst becomes thick, it takes time for the cathode catalyst layer to be replaced with Air or H_2 at the time of startup and shutdown, so that Pt particles are detached from CB support due to severe carbon corrosion and the cell performance deteriorates. On the other hand, when the Pt loading percentage is high, these gas fronts move rapidly and the number of Pt particles detached from the CB support is small, but the distance between the Pt particles is short, so that the Pt particles become coarse. It was shown that as the coarsening of Pt continued, ECSA decreased and Pt eluted in the polymer electrolyte membrane increased, resulting in a decrease in cell performance.

To improve performance and durability, it is important to design the interior and exterior distribution of Pt particles so that ionomer does not thickly cover the Pt surface and design the Pt loading percentage to minimize carbon corrosion and coarsening of Pt particles.

In this study, detailed catalyst structure was analyzed from N_2-adsorption measurements, STEM observation, and cross-sectional observation, and cell performance and electrochemical measurement results were examined in detail. Most of the previous studies analyzed the structures of supports and catalysts and linked them to cell

performance and durability. In this study, I newly proposed that the hysteresis volume is a method for estimating the ionomer covering state, and this is the first report to propose a catalyst design guideline in consideration of the ionomer covering state. I also investigated the effects of specific adsorption of ionomer, which many fuel cell researchers have been interested in in recent years and provided the optimal design guidelines that I think. There are many previous studies that Pt should have a structure that is not directly covered by ionomer. Meanwhile, I showed the design guideline that the structure in which both Pt supported on the surface of the carbon support and directly covered by the ionomer and Pt supported in the catalyst pores in which the ionomer cannot penetrate is important. The new evaluation method and the design guideline proposed in this study are considered to be a result that contributes to future research. In addition, most of the studies on durability evaluation so far have investigated the effect of voltage on the catalyst by changing the voltage in a uniform reaction field in which H_2 is supplied to the anode and N_2 is supplied to the cathode. On the other hand, in this study, I considered that it is important to reflect the research results in the actual system and evaluated the durability under actual operating conditions. Durability evaluation was performed assuming actual operating conditions in which H_2 is supplied to the anode and air is supplied to the cathode to change the current, and startup / shutdown operation of the actual system is assumed. As a result, I was able to investigate the durability and elucidate the catalyst deterioration mechanism under conditions closer to the actual system, including the effects of generated water and gas flow when startup and shutdown. Few studies have evaluated durability under production conditions, and I was able to present very significant results.

As a result, I was able to propose a new view and deterioration mechanism regarding the covering state of ionomer near the catalyst pores, which had been unclear until now, and show important parameters for catalyst design that lead to improved cell performance and durability.

Although only a small part of what I was able to investigate in this study, I believe that it is essential to improve the catalyst for the further spread of fuel cells, and research on high specific surface area support catalysts will become important in the future. I hope that the results of this study will help reduce the cost and improve the durability of PEFCs and contribute to practical application.

4-2. Future prospects

In recent years, research using HSC supports, which I focused on in this study, has attracted attention in the development of fuel cell catalysts. I will propose future strategies to improve performance and durability.

In this study, I investigated the catalyst design when Pt particles were used as the cathode catalyst, but I could not study the catalyst using Pt alloy. In fuel cell catalysts, many studies have investigated catalysts using Pt alloys in order to enhance ORR activity and MA more than Pt.[1–3] Although the initial performance is improved, it is difficult to maintain the initial performance due to the dissolution of alloys such as Co, and there remains a challenge in durability.[4] When the catalyst particles are changed from Pt particles to Pt alloy particles, it is important for future fuel cell catalyst development to find a new catalyst design guideline based on the insights in this study.

In addition, high oxygen permeation ionomer (HOPI), which has a structure with a five-membered ring in the side chain, is attracting attention as one of the methods for

improving ORR activity and oxygen diffusibility in the highly current density region.[5–7] It has been reported that HOPI is also used in the second generation of MIRAI,[8] and it is a material that is expected to be further improved in the future. In order to further improve performance, it is necessary to study the performance and durability of HSC catalysts with HOPI applied.

In this study, I used CB, which has been used as a support for many years. In recent years, mesoporous carbon (MPC), which is a porous carbon material containing a large amount of mesopores (diameter 2 to 50 nm) and having a characteristic pore structure called communication pores, is attracting attention as a new type of support material.[9–13] Research on Pt/MPC is still scarce, and research on the detailed structure of the ionomer/Pt interface and deterioration mechanism has just begun[14], and I think that research will become more active in the future. The design concepts of ultrahigh specific surface area carbon support/Pt and MPC/Pt are similar, and I think that the findings of this study can be reflected, and the development of new support materials is one of the important efforts.

4-3. References

1 Kabir, S.; Myers, D, J.; Kariuki, N, N.; Park, J.; Wang, G.; Baker, A.; Macauley, N.; Mukundan, R.; More, K, L.; Neyerlin, K, C. Elucidating the Dynamic Nature of Fuel Cell Electrodes as a Function of Conditioning: An ex Situ Material Characterization and in Situ Electrochemical Diagnostic Study. *ACS Appl. Mater. Interfaces* 2019, 11, 48, 45016–45030.

2 Stariha, S.; Macauley, N.; Sneed, B, T.; Langlois, D.; More, K, L.; Mukundan, R.; Borup, R, L. Recent Advances in Catalyst Accelerated Stress Tests for Polymer Electrolyte Membrane Fuel Cells. *J. Electrochem. Soc.* 2018, 165, F492–F501.

3 Sneed, B, T.; Cullen, D, A.; Mukundan, R.; Borup, R, L.; More, K, L. PtCo Cathode Catalyst Morphological and Compositional Changes after PEM Fuel Cell Accelerated Stress Testing. *J. Electrochem. Soc.* 2018, 165, F3078–F3084.

4 Ahluwalia, R, K.; Papadias, D, D.; Kariuki, N, N.; Peng, J-K.; Wang, X.; Tsai, Y.; Graczyk, D, G.; Myers, D, J. Potential Dependence of Pt and Co Dissolution from Platinum-Cobalt Alloy PEFC Catalysts Using Time-Resolved Measurements. *J. Electrochem. Soc.* 2018, 165, F3024.

5 Braaten, J.; Liu, J.; White, Z.; Tiwari, N.; Brown, G.; Park, A, M.; Paul, D.; Ulissi, Z.; Litster, S. Development of Polymer Electrolyte Fuel Cell (PEFC) Cathodes with High Oxygen Permeability Ionomer (HOPI) for High Performance and Durability. *Meet. Abstr.* 2021, MA2021−02, 1188.

6 Department of Energy, “Durable High-Power Density Fuel Cell Cathodes for Heavy-Duty Vehicles”, https://www.hydrogen.energy.gov/pdfs/review20/fc327_litster_2020_p.pdf

7 Jinnouchi, R.; Kudo, K.; Kodama, K.; Kitano, N.; Suzuki, T.; Minami, S.; Shinozaki, K.; Hasegawa, N.; Shinohara, A. The role of oxygen-permeable ionomer for polymer electrolyte fuel cells. *Nat. Commun.* 2021, 12, 4956.

8 Toyota Technical Review “Development of the Fuel Cell System for the Second-Generation MIRAI”. 2021/2, 236.

9 Joo, S, H.; Pak, C.; You. D. J.; Lee, S-A.; Lee, H, I.; Kimb, J, M.; Chang. H.; Seung, D. Ordered mesoporous carbons (OMC) as supports of electrocatalysts for direct

methanol fuel cells (DMFC): Effect of carbon precursors of OMC on DMFC performances. *Electrochim. Acta* 2006, 52, 1618–1626.

10 Ahn, C-Y.; Cheon, J-Y.; Joo, S-H.; Kim, J. Effects of ionomer content on Pt catalyst/ordered mesoporous carbon support in polymer electrolyte membrane fuel cells. *J. Power Sources* 2013, 222, 477–482.

11 Ding, J.; Chan, K-Y.; Ren, J.; Xiao, F-s. Platinum and platinum–ruthenium nanoparticles supported on ordered mesoporous carbon and their electrocatalytic performance for fuel cell reactions. *Electrochim. Acta* 2005, 50, 3131–3141.

12 Salgado, J. R. C.; Quintana, J. J.; Calvillo, L.; Lázaro, M. J.; Cabot, P. L.; Esparbé, I.; Pastor, E. Carbon monoxide and methanol oxidation at platinum catalysts supported on ordered mesoporous carbon: the influence of functionalization of the support. *Phys. Chem. Chem. Phys.* 2008, 10, 6796–6806.

13 Hori, M.; Kato, H.; Matsumoto, S.; Nishi, N. FC Catalyst with Mesoporous Carbon. *Meet. Abstr.* 2013, MA2013–02, 1500. https://ecs.confex.com/ecs/224/webprogram/Paper22769.html

14 FC-Cubic, “6th FC-Cubic Open Symposium Remote Poster Session”, https://fc-cubic-event.jp/?page_id=1278

List of publications

1. Effect of Pt and Ionomer Distribution on Polymer Electrolyte Fuel Cell Performance and Durability

   Aki Kobayashi, Takahiro Fujii, Chie Harada, Eiichi Yasumoto, Kenyu Takeda, Katsuyoshi Kakinuma, and Makoto Uchida, *ACS Appl. Energy Mater.* 2021, 4, 2307−2317.

2. Effect of Pt Loading Percentage on Carbon Blacks with Large Interior Nanopore Volume on the Performance and Durability of Polymer Electrolyte Fuel Cells

   Aki Kobayashi, Takahiro Fujii, Kenyu Takeda, Kayoko Tamoto, Katsuyoshi Kakinuma, and Makoto Uchida, *ACS Appl. Energy Mater.* 2022, 5, 316−329.

Meeting Abstracts

1. 88th Meeting of the Electrochemical Society of Japan, March, 2021, Digital Meeting,
   Aki Kobayashi, Katsuyoshi Kakinuma, Takahiro Fujii and Makoto Uchida

2. 240th ECS Meeting, October, 2021, Digital Meeting,
   Aki Kobayashi, Katsuyoshi Kakinuma, Takahiro Fujii and Makoto Uchida

Awards

1. Student Presentation Award

88th Meeting of the Electrochemical Society of Japan, March, 2021, Digital Meeting,

“Pt とアイオノマの分布状態が電池性能および耐久性に与える影響”

Aki Kobayashi, Katsuyoshi Kakinuma, Takahiro Fujii and Makoto Uchida

Acknowledgments

The present thesis is the summary of work carried out at Fuel Cell Nanomaterials Center, and Interdisciplinary Graduate School of Medicine and Engineering in University of Yamanashi from 2019 to 2022.

This research was supported by funds for the "Superlative, Stable, and Scalable Performance Fuel Cell" (SPer-FC) and the "Electrolytes, Catalysts and Catalyst Layers with Extraordinary Efficiency, Power and Durability for PEFCs to 2030" (ECCEED'30-FC) projects from the New Energy and Industrial Technology Development Organization (NEDO).

I would like to express my greatest gratitude to **Professor Makoto Uchida** of University of Yamanashi for providing me this precious study opportunity as a Ph.D. I am grateful for his continued guidance, discussions, valuable suggestions, and warm encouragement through my study.

I would also like to express my sincere gratitude to **Professor Katsuyoshi Kakinuma** for his valuable suggestions, discussions, and guidance through my research. I also would like to express my gratitude to **Professor Donald Alexander Tryk** for his invaluable suggestions and comments.

Sincere gratitude is expressed to **Mr. Takahiro Asakawa**, **Ms. Kayoko Tamoto**, **Ms. Ayana Ooga** for the TEM, STEM and FIB measurements.

I would like to express my sincere gratitude to all of my colleagues at the Fuel Cell Nanomaterials Center for their kind support and help. Thank you everyone for helpful advice and valuable suggestion. And thank you for always worrying about my physical condition and eating habits.

I would like to express my greatest gratitude to **Manager Eiichi Yasumoto** of Panasonic Corporation for giving me the opportunity to study as a Ph.D. while working. I feel that the experience of studying in the doctoral course was a turning point for me. I am deeply grateful.

I am also very grateful to **Manager Kenyu Takeda**, **Mr. Takahiro Fujii**, and **Dr. Chie Harada** of Lifestyle Updates Business Division Electric Works Company of Panasonic Corporation for their warm encouragement and kind support of my research. Thanks to everyone's support, I was able to continue my doctoral course while working. Also, thank you for your concern and support for my physical condition and eating habits. I was able to continue studying in the doctoral course without getting sick.

I would like to express my sincere gratitude to my colleagues at Panasonic Corporation for their warm encouragement and valuable suggestions. Since I had many long-term business trips, everyone took care of my physical condition and helped me with various things at the company.

Finally, there were times when it was very difficult to carry out study and work at the same time. I haven't been able to meet in person and spent a lot of time together, but I would like to express my sincere gratitude for the support of my family.